2015-04-29

Magnetic Resonance Imaging for Tracking of Cells and Agents Targeted to Bone Fracture

Taha, May

UNIVERSITY OF CALGARY

Magnetic Resonance Imaging for Tracking of Cells and Agents Targeted to Bone Fracture

by

May Abdel Hamid Taha

A THESIS

SUBMITTED TO THE FACULTY OF GRADUATE STUDIES

IN PARTIAL FULFILMENT OF THE REQUIREMENTS FOR THE

DEGREE OF DOCTORATE OF PHILOSOPHY

GRADUATE PROGRAM IN MEDICAL SCIENCE

CALGARY, ALBERTA

APRIL, 2015

Abstract

Regenerative medicine is likely to play a major role in the treatment of musculoskeletal diseases. Stem cell therapies could be used to restore damaged or diseased tissues by contributing to the healing process. Additionally, bone targeted nanoparticles could be of great use in this field, as they can be used to deliver therapies or to image an injury site. In order to evaluate and monitor new regenerative therapies in preclinical models over time, a non-invasive *in vivo* imaging tool is needed. Use of such an imaging method will enable testing new cell therapies in bone. Magnetic resonance imaging (MRI) holds considerable promise for this purpose. Considering that it is a non-invasive and non ionizing method makes it well-suited for repeated measurements studies.

Initially, we optimized an MRI protocol for visualization of bone injuries, and then we compared the optimized MRI protocol with μCT as the gold standard for bone imaging. We found that MRI offers several advantages over μCT, including that it visualized soft tissue, edema, therapeutic biomaterials, and is especially useful when ionizing radiation is to be avoided. Subsequently, we used MRI to assess materials used in this study such as bone targeted nanoparticles, contrast agents and stem cell scaffolds.

After establishing the MRI protocol, we labelled-differentiated ESCs, and then transplanted them *in vivo* for MR tracking. The results showed that MRI detected the labelled cells *in vivo* that under some conditions the MRI could detect migration of the differentiated ESC's to remote site of injury. The findings were validated by histology and immunohistochemistry.

To our knowledge, this is the first study to track cells in bone fracture using MRI. Based on the results of this research, future studies can use the developed cell tracking model for testing the effectiveness of novel cell therapies that promote bone repair.

Acknowledgements

I would like to thank my supervisors, Dr. Jeff Dunn and Dr. John Matyas, for their contribution and guidance in the past five years. I would also like to express my special appreciation to my supervisory committee members Dr. Derrick Rancourt and Dr. Roman Krawetz for their continuous support and encouragement.

I would also like to express my gratitude for Dragana Ponjevick, Jaymi Taiani, Ying Wu, and Alison King for their added technical expertise and support. Also, thank you Tad Foniok, Dave Kirk and David Rushfold for their technical assistance with MR imaging.

Last but not least, I would also like to extend my gratitude to my family, especially my dad Abdel Hamid, my mom Samia, my sisters Marwa, Maha and Merna, for believing in me. Without their support, this achievement would not have been possible.

To my husband Ahmed and my kids Yousef and Malika---thanks for supporting me through the tough times.

Table of Contents

List of Tables

List of Figures and Illustrations

List of Symbols, Abbreviations and Nomenclature

Symbol	Definition
MRI	Magnetic resonance imaging
µCT	Micro-computed tomography
SPECT	Single photon emission computed tomography
PET	Positron emission tomography
T	Tesla
SE	Spin echo
GE	Gradient echo
GE-FLASH	Gradient Echo-Fast Low Angle Shot
True-FISP	True Fast Imaging with Steady State Precision
RARE	Rapid Acquisition with Relaxation Enhancement
CPMG	Carr Purcell Meiboom Gill Sequence
SWI	Susceptibility Weighted Imaging
TR	Repetition time
TE	Echo time
T_1	Longitudinal relaxation time
T_2	Transverse relaxation time
M_0	Net magnetization
M_z	Net magnetization in the z-direction
R_1	$1/T_1$
R_2	$1/T_2$
R_2*	$1/T_2$*
Gd	Gadolinium
SPIO	Super paramagnetic iron oxide
S/N	Signal to noise ratio
RF	Radiofrequency
SI	Signal intensity
ROI	Region of interest
H & E	Hematoxylin and Eosin
IHC	Immunohistochemistry
GFP	Green Fluorescent protein
PB	Prussian blue
SDS	Sodium Dodecyl Sulphate
SSC	Saline sodium citrate
ESC	Embryonic stem cells
dESCs	Differentiated embryonic stem cells
MSC	Mesenchymal stem cells
BGP	Beta-glycerol phosphate
DMEM	Dulbecco’s modified eagle medium
FBS	Fetal bovine serum
LIF	Leukemia inhibitory factor
PBS	Phosphate buffered saline

3-D	3 dimensional
µg	Microgram
µl	Micro-litre
µm	Micro-meter
Nm	Nanometer
Cm	Centimeter
Mm	Millimeter
M	Meter
S	Second
Min	Minutes
D	Days
H	Hours
MSK	Musculoskeletal system
ms	Muscle
NP	Nanoparticles
BP	Bisphosphonated

Chapter One: **Introduction**

1.1 Problem statement

Musculoskeletal (MSK) diseases affect 11 million Canadians annually[1]. In 2000, MSK disease cost the Canadian health care system $22.3 billion[2], a higher cost than for any other disease. MSK disease includes injuries or diseases in joints, ligaments, muscles, nerves, tendons, and bones. These diseases have many aspects which adversely affect the patient's quality of life, including long or short term disability, medical, economic, psychological, and social problems[3].

Regenerative medicine, with its novel tools, may provide excellent solutions for treating chronic MSK conditions. Its focus is to replace, engineer or regenerate tissues or organs in order to restore their normal function. Within regenerative medicine, our focus is on imaging tissue engineered therapies for healing bone fractures. The tissue engineered therapies involve cellular therapies, such as stem cell therapy, and biomaterial-based products. Stem cell therapy has been used to speed up and improve the healing of large bony defects[4]. For example, embryonic stem cells (ESCs) promoted bone healing in a murine fracture model[5]. Biomaterials which are used as stem cell scaffolds, have themselves been shown to promote healing of skeletal injuries in the absence of stem cells[6-8]. Lastly, bone-targeted nanoparticles have been used to deliver bioactive factors which enhance bone healing[9].

In order to monitor new cell therapies and learn about their *in vivo* behaviour and outcomes, a non-invasive imaging method is required. This method has to be safe, non-invasive, able to monitor the cell therapy on serial basis, and doesn't negatively affect the treatment outcome, but such a tool does not currently exist. The information provided by non-invasive imaging will help in testing new cell therapies.

The overall aim of this thesis is to develop an efficient protocol for the MR imaging of treatment options in a murine bone fracture model. Specific sub-aims relate to optimizing an MR imaging protocol that allows the *in vivo* imaging of the bone fracture model with minimal artefacts in a reasonable acquisition time. An optimal MR protocol is one that detects the bone fracture, the surrounding anatomical structures, the stem cells, and the biomaterials used as stem cells scaffold. The cells used in the bone-cell therapy should be effectively labelled with an MR contrast agent that does not adversely affect its proliferation and differentiation capacity, yet have enough contrast agent to be detected in the MR images. Finally, the optimized MRI protocol would be used to track the labelled cells *in vivo* in the bone fracture model, on serial basis. Different histological and immunohistochemical protocols were used to verify the MRI results. The result will be a protocol for non-invasive imaging, including a model system of bone fracture and an imaging time course of the fracture's healing.

The focus of this project was to lay the foundation for stem cell tracking in bone fracture models. The model was approached from a broader prespective aiming to optimize all the associated tools like MRI, cell culture and differentiation, cell labelling, cell imaging and tracking. Thus this study is considered to be a descriptive study. In future studies, the scope of the work could be narrowed to focus more on the successful outcomes from this project to build upon them. The advantage of narrowing the scope of work is to increase the rigour of the results.

Using magnetic resonance imaging (MRI) to track cells shows promise for the field of stem cell therapy[10,11]. This protocol could then be applied to many fields of regenerative medicine, drug delivery and cell therapies[2,4,12] such as, studying the fate of tissue engineered bone graft material in a bone fracture model[13,14].

1.2 Regenerative medicine, bone fracture and novel treatments

1.2.1 The biology of bone fracture

Bone plays a critical role in the mechanical support of living organisms and it acts as a mineral reservoir for calcium and phosphorus[15]. It also plays an important role in hematopoiesis[15]. Bone tissue is composed of a cellular and a non-cellular component. The cellular component contains osteoblasts, osteocytes, and osteoclasts[15]. The non-cellular components is divided into organic and inorganic components. The organic components are type I collagen and growth factors such as glycosaminoglycans, osteocalcin, osteonectin, and bone sialoproteins[16]. The inorganic component is formed of hydroxyapatite crystals, which act as the matrix for all other components[16]. The matrix is initialy laid as osteoid which mineralizes by the deposition of calcium and phosphate[16].

In brief, the cellular component of bone consists of osteoblasts, which help in bone formation through the deposition of collagen and the mineralization of hydroxyapatite[15]; osteocytes, which are the mature form of osteoblasts trapped in the matrix and which carry out the normal metabolic processes of bone[15]; and osteoclasts, which are multinucleated cells responsible for bone resorption[15]. The surface of the bone is covered by a membrane called the periosteum, which consists of fibroblasts and which contributes to bone regeneration[16].

Bone develops through one of two mechanisms. Intramembranous ossification, mesenchymal progenitor cells form bone directly[15]. In endochondral ossification, mesenchymal progenitor cells form a cartilaginous template that is subsequently replaced by bone during development[17].

The skeleton is composed of two types of bone: cortical (compact) bone and cancellous (spongy) bone. Cortical bone is denser than cancellous bone[18]. Long bones, such as tibia, are composed of cortical bone filled with bone marrow and covered with a layer of periosteum.

Unlike other body tissues, which heal by scar formation, bone heals by regeneration, i.e. by forming new bone tissue. Two perspectives are important when considering bone healing: the tissues involved and the stages that take place. The fracture healing response takes place in four distinct bone-related tissues: the marrow, the cortex, the periosteum, and the external soft tissue[19]. After bone fracture, the bone marrow loses its normal architecture and its cells start to reorganize themselves into regions of high- and low-cell density. The high-cell density regions contribute to bone formation. The cortex responds by re-establishing itself and bridging the fracture. Interestingly, the periosteum has the most important response in effecting fracture healing. It contains osteoprogenitor cells and mesenchymal cells which contribute directly to bone formation through intramembranous ossification. The response of the external soft tissue includes the development of a bridging callus which stabilizes the fracture[20].

In mice, the bone fracture healing process is composed of five stages that usually involve a combination of endochondral and intramembranous ossification. The process in humans is very similar to the process in mice[21]: (i) hematoma formation and inflammation, (ii) angiogenesis, woven bone and cartilage formation through intramembranous and endochondral ossification respectively, (iii) cartilage calcification, (iv) cartilage removal, and (v) bone formation associated with a chronic stage of bone remodeling[20,22]. In the early stage of inflammation, a hematoma is formed which transforms into granulation tissue that contains undifferentiated mesenchymal stem cells. It is suggested that the hematoma releases signaling molecules that could be important in regulating mesenchymal cell proliferation and differentiation[20]. In the second stage

of healing, which occurs during the first 7 to 10 days, the periosteum starts to form bone intra-membranously, leading to the deposition of woven bone. At the same time, the external soft tissues contribute to the healing process by forming a fracture callus. The fracture callus contains hard and soft callus. The hard callus is formed by intramembranous ossification while the soft callus is formed by endochodral osssification[20]. In the third stage, calcification of the cartilage occurs[20]. In the fourth stage, the hypertrophic chondrocytes of the cartilage are replaced with osteoblasts and osteoclasts, which in turn replace cartilage with woven bone[20]. In the fifth and last stage of bone healing, the woven bone is remodeled through activities of osteoblasts and osteoclasts into denser lamellar bone[20]. By the 6th week, the bone fracture is completely bridged with new cortical bone [22].

Normally, bone has the capacity to heal itself[19]. However, in some diseases such as osteoporosis and osteomalacia, the bone's capacity to heal itself is impaired[15]. Impaired healing leads to a loss of bone structure and function, and to disability[4,15]. Thus, it is critical to restore injured bone. As mentioned in the introduction, regenerative medicine, with its novel tools, offers different types of therapies to treat impaired bone healing, these tools include stem cells, biomaterials and nanoparticles. While these tools show promise, more animal testing is required before they can be translated into humans.

Different animal fracture models offer different fracture healing cascades. For example, changing the fracture level in rat tibial fractures was shown to affect the biomechanical properties of the healing bone[23]. The selection of an animal fracture model is critical for the success of the study. The choice of the animal model should consider the question being examined, the reproducibility of the bone fracture, the standardization and the biomechanical properties of the model[24,25].

Numerous studies have aimed to develop and standardize animal fracture models[22,23,26]. For example, Greiff described the ideal experimental fracture model as one that has a standardized site, type, and degree of bone and soft tissue damage[25]. In this study, a bur-hole fracture model was selected, in which a hole is drilled into the medial aspect of the tibia of a mouse while keeping the opposing side intact. The bur-hole fracture model is considered a closed bone fracture model where all the characteristics of fracture healing in a fixed long bone applies[22, 24,27,28]. One of the advantages of this model is that the fractured parts remain fixed together and do not need external fixation to immobilize the bone. Other advantages include standardized bone healing conditions and a fracture of reproducible size and Depth [29].

The reproducibility of the model was previously evaluated in a study done by Taiani[29] using μCT, where they found that the created fracture has a consistent depth, diameter and distance from the epiphysis. In this thesis project a similar method was used to create the bone fractures. The reproducibility of the fracture and consistency of healing was evidenced in previous studies where they were able to reproduce fractures of the same size and at the same location in successive surgeries[22,30]. Plus, the fracture healing pattern was similar across their subjects[22,29,30]. The reproducibility of the model in this thesis, defined as the location of the drill-holes, is noted in Chapter 8 section 3. Additionally, the fact that the tibia is not fully covered with muscles allows the bone fracture to be drilled with minimal soft tissue damage. This is important because the degree of soft tissue damage can affect the healing process.

Uusitalo *et al.*[22] first developed this bone fracture model. Then, a modified version of the model was developed and used by our collaborators in the Dr. Matyas lab to study the efficacy of new stem cell therapies on promoting bone healing[30]. We further modified the model to allow the imaging and the tracking of stem cell therapies in the bone fracture[27]. In our experiments,

multiple fractures were created in the tibia of the mouse. This was done to study the migratory behaviour of the cells from one fracture to the other across time. Moreover, the multiple fractures allowed implanting and comparing several biomaterials within the same mouse, which saved animal lives, MRI time, and cost. The distance between the tuberosity and the upper fracture was ~3 mm and the distance between the two fractures was ~3 mm (Figure 1-1). Cell therapy or biomaterials were transplanted into the holes according to the type of the experiment performed.

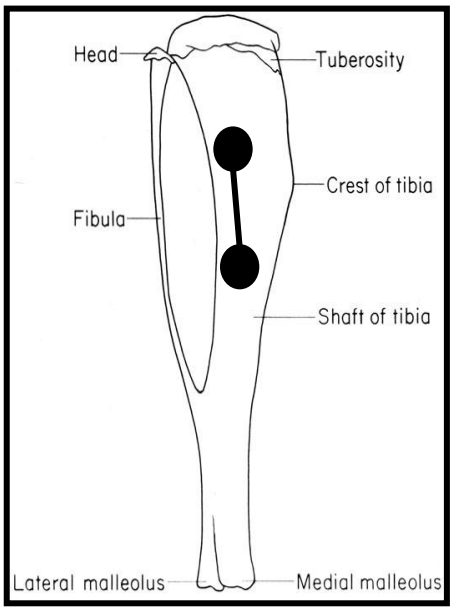

Figure 1-1 Illustrative diagram of the bone fracture model used in our study (Based on Cook)[31].

This model has some strengths and limitations. Most importantly, the small size of the mice made the surgical procedure challenging, but allowed us to place the whole mouse inside the small bore of the 9.4 T Bruker Avance MRI magnet. This enabled us to image live mice *in vivo* without sacrificing them. This model offered the needed reproducibility, insuring consistent results in terms of the healing process.

In summary, the model used is a reproducible bur-hole fracture model that generates a closed bone fracture to track stem cells *in vivo* using MRI. This model meets the criteria of reproducibility which makes it the most favourable model for imaging and monitoring novel tissue engineered therapies.

1.2.2 Biomaterials used in tissue engineered treatments

Many bone tissue engineered constructs uses scaffolds to deliver stem cells (discussed below in Section 1.2.3), growth factors, and therapeutic materials to the bone fracture[32]. All of these can be used individually or combined to form a treatment paradigm.

Scaffolds can play a major role in the success of the treatment, both through being used to support stem cells mechanically and through themselves promoting bone healing. The importance of mechanical support was evidenced by our preliminary experiments in which stem cells were suspended in culture media only. After transplantation, the cells flowed to other sites. However this did not happen when a 3D collagen gel scaffold was used to support the cells mechanically (detailed description is present in chapter 8). In addition to the 3D collagen gel, we imaged matrigel, purecol gel and hydroxyapatite (HA). Matrigel and purecol have been used previously as scaffolds for stem cells[33]. HA has been shown to contribute to the healing of bony defects in rabbit tibiae[8]. Transplanting collagen gel that contained cultivated bone marrow stromal cells caused a 30% increase in bone regeneration when compared to controls (nothing injected) after 120 days[34]. Scaffolds play an integral part in tissue engineered therapies. Therefore, we aimed not only to study the effects of scaffolds on bone healing in our model, but also how these scaffolds appeared on MR images to facilitate future studies on bone fracture therapies.

Nanoparticles are composed of liposomes. The liposomes can be bound to a bisphosphonate ligand which has strong affinity to bone[9]. Bone-targeted nanoparticles have been used to deliver therapeutic agents efficiently to the bone and reduce the nonspecific distribution of drugs to other organs[35]. Additionally, they have been be used to retain bone-morphogenic protein (bone-inducing factor) in a bioactive form which has been used to treat bone defects[9]. Nanoparticles could be used to carry MRI contrast agents, such as gadolinium or iron oxide particles. This approach could be used to decrease the toxicity of contrast agents and to increase the specificity of the delivery to the site of fracture. In this project, we used MRI to test how efficiently nanoparticles encapsulate the contrast agent gadolinium.

1.2.3 Stem cells

Stem cells have been used to repair bone injuries by mimicking the natural healing process of bone[4,14,36,37]. Stem cells can be obtained from different sources , including adult or embryonic tissues[32]. They retain the ability to be expanded and differentiated into more specialized cell types, which can be done *in vitro* using different culture systems and medium supplements [37].

Stem cells obtained from adult tissues are multipotent, meaning they have restricted differentiation potential[38]. They are found in limited numbers and are difficult to isolate[14]. However, they do not provoke an immune reaction when used for autogenous transplantation and they do not form tumours[36]. Despite the difficulty of isolating them, mesenchymal stem cells (MSC) obtained from adult tissue are the most commonly used cells in bone repair, in animals and humans[39]. They are present in bone marrow, skin and blood[36]. They have the capability to differentiate into more specialized cells such as bone, cartilage, fat, ligament, muscle, and tendon cells[14,38].

Stem cells can also be obtained from tissues during the early development, such as embryos. ESCs, which fall into this category, are derived from the inner cell mass of a blastocyst at the fifth day, an early stage pre-implantation embryo[40]. ESCs were isolated from mice by Evans and Kaufman in 1981[41]. These cells have two favourable characteristics: self renewal and pluripotency. Self renewal means that the cells have the capacity to divide and give rise to more identical stem cells[40]. Pluripotency means that the cells have the capacity to differentiate into any cell type from the three germ layers[40,41]. From isolation, to implantation, cell based therapies are very sensitive to a variety of factors such as type and source of cells, number of cells, differentiation protocol, and mode of delivery. We focused on ESCs as the cells of choice for bone repair because they are more feasible for large scale production than MSCs.

ESCs can heal a bony defect because they have the ability to give rise to all types of adult cells including those of osteogenic lineage, i.e. osteoblasts, osteoclasts and osteocytes[37,42]. However, there is a risk of tumour formation if the cells are transplanted in an undifferntiated form[5,43]. Therefore, it is very important to differentiate the ESCs into osteoblasts before transplanting them. The differentiation protocol followed in this study is a collagen I matrix polymerized with beta-glycerol phosphate (BGP)[44]. This protocol was previously used to differentiat the ESCs into osteogenic lineage, and prevented the ESCs from forming tumours *in vivo* and provided mechanical support the cells needed to help them stay and integrate at the site of fracture[38].

The ESCs used in this project were allogenic cells derived from male mice. They were transplanted into bone injuries of female mice of the same strain. This model offered two benefits. First, it minimized the risk of rejection. Second, it enabled tracking of the transplanted cells using the Y-chromosome *in situ* hybridization protocol discussed in chapter 8.

1.3 Imaging of bone fracture

Non-invasive imaging can offer a quantitative and qualitative assessment of a healing bone[27,45], and is therefore an essential tool for the diagnosis and monitoring of various diseases, and for the advancement of research[46,47]. The gold standard methods for bone imaging are plain radiography (x-ray) and computed tomography (CT)[27]. However, recent developments in the field offer MRI as a new approach for high resolution bone visualization applications[27]. This is explained in detail in chapter 2.

1.3.1 MRI of bone fracture

The development of MR imaging was greatly advanced by the discoveries in physics, math, and computers. Examples of the scientific achievements that contributed to the development of MRI are the development of Fourier transformation method by Fourier, the evidence of the existence of magnetic resonance presented by Rabi, and the discoveries about the quantum behavior of particles by Pauli[48,49]. All these discoveries and much more were the main reason that allowed researchers to develop MRI. Later in 1971, Damadian discovered that healthy tissue and cancerous tissues display different relaxation times which encouraged scientists to further investigate the use of MRI to study diseases[50]. In 1973, Paul Lauterbur published the first nuclear magnetic resonance image[51,52]. In 1977, Damadian et al. performed the first MRI body scan on human[53]. At present, researchers are working on developing better MRI hardware and software to obtain higher-resolution, better-quality images in a shorter scan time.

Nuclei with spin that has a net magnetization value can be imaged with MRI[54]. However, the hydrogen nucleus is the most frequently imaged nucleus due to its great abundance in biological tissues[55]. All the MRI done in this thesis used the hydrogen nucleus. MRI machines use strong magnetic fields and electromagnetic waves (radiofrequency waves) to form images of tissue[55]. A

radiofrequency (RF) pulse, produced by a transmitter, tips the net magnetization of the hydrogen atoms out of their alignment with the strong magnetic field[54]. Then, the hydrogen atoms relax back into alignment with the magnetic field, releasing energy which is caught by the receiver as signal[54]. Each tissue produces different signal based on its physical properties, such as water concentration, producing contrast among the different tissues[54]. MRI is a sensitive diagnostic technique; in which minimal signal intensity changes can indicate hidden pathologies[45].

Even though x-ray and CT are the imaging methods most commonly used to diagnose bone pathologies, in some cases MRI could be the method of choice for diagnosing a bony defect and following up its treatment[56]. MRI is sensitive to small changes in signal intensity, such as occur in stress fractures. Previous studies have shown that fracture lines that were missed on radiographs could be detected in MRI[45,57]. Accurate diagnosis is crucial in decision making for the patient's treatment plan[45]. Radiography mainly detects the late phases of bone stress injuries[58]. Another advantage of using MRI to image bone pathologies is that it provides information about all the soft tissue structures surrounding the bone, such as the periosteum, bone marrow, soft tissue, ligaments, and muscles. Some of these soft tissues play a major role in the bone healing process and need to be assessed to select the specific therapeutic approach[59]. However, many of these tissues do not appear clearly on x-ray based imaging[27]. Furthermore, MRI is used to examine the role of various therapeutic biomaterials in fracture healing, unlike CT which does not generate enough contrast to study these biomaterials. This was demonstrated in a study in which bone graft material appeared similar to the adjacent cortical bone in CT, but had a distinctive appearance in MR images[47]. Finally, MRI does not involve ionizing radiation, so it could be used for serial imaging to avoid unnecessary radiation exposure (Figure 1-2).

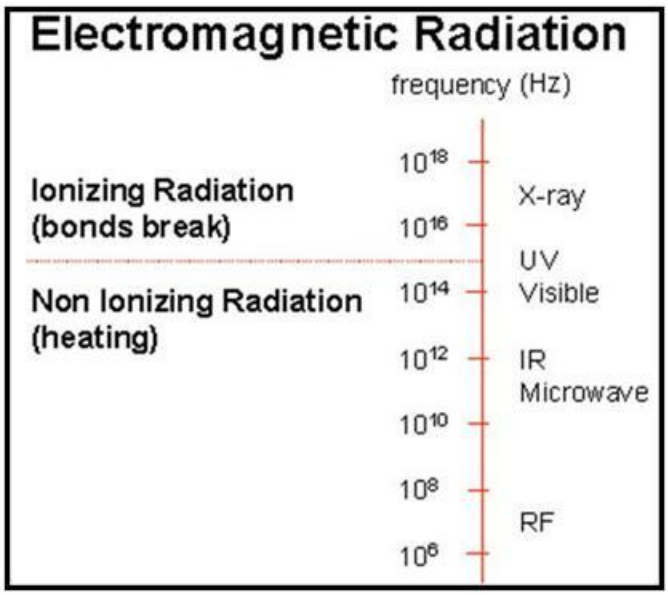

Figure 1-2 A scale showing the different frequencies of electromagnetic waves used in imaging. X-rays lie in the ionizing radiation zone while the radiofrequency waves used in MRI lie in the non-ionizing zone (Reproduced from Hornak)[54].

MRI of bone must be done carefully since the majority of signal obtained from bone is produced from its water content as opposed to its organic matrix. Bone tissue contains only 15% water, thus producing low amounts of signal and appearing hypointense, or dark, in MR images[46,60]. Recently developed MRI protocols were able to obtain signal from the bone hydrogen nuclei[61].

MRI has some limitations that we tried to overcome in order to use it in our project. First, MR images display motion artefacts if subjects move. Long scan times in particular increase the possibility of motion artefacts, because of subjects' discomfort and their inevitable movements[55]. In our experiments, the mice had to be anaesthetized and restrained to overcome this problem. Additionally, because we are using a very high field magnet (9.4 T) we can obtain a higher signal to noise ratio (S/N) or substitute S/N for a better resolution or a faster scan[62]. Second,

studying injuries in very small animal models such as the mouse requires high resolution and the images can be spoilt by susceptibility artefacts generated by the bone-soft tissue interfaces[27]. However, the increased availability of a range of MRI sequences makes it possible to overcome this issue. Lastly, MRI is contraindicated in subjects with metal implants or pacemakers due to safety concerns[55]. However, our mice do not have either, and future human test subjects could be selected that do not have these.

In summary, we are developing a reproducible MRI cell tracking system in a bone fracture model, for studying tissue engineered therapies. It offers several advantages over μCT, including that it can visualize soft tissue and edema clearly, can visualize therapeutic biomaterials[27] and is especially good at imaging bone fracture. Additionally, it can be used safely during serial imaging because it does not use ionizing radiation. MRI is a powerful tool that provides the contrast needed for this study. Animal anesthesia and advances in MR imaging sequences and hardware make it possible to overcome the limitations of MRI such as long imaging times and susceptibility artefacts.

1.3.2 MR imaging of bone-targeted nanoparticles and biomaterials

The development of nanoparticles that deliver biomaterials specifically to bone tissue is important in developing new therapeutic agents that can heal bony defects. Our collaborators in Dr. Uludag's lab at the University of Alberta, bound bisphosphonated ligands, which have a high affinity to bone, to the nanoparticles[9]. These particles have the capacity to encapsulate drugs and deliver them to bone successfully[9]. Members of the Uludag lab were developing a protocol to incorporate Gd into the nanoparticles, making the nanoparticles visible and traceable on MR images. Our contribution was to determine if the nanoparticles were able to retain the Gd efficiently. We did this by measuring the relaxivity of the nanoparticles using MRI *in vitro*.

Determining whether nanoparticles can be efficiently labelled with Gd is an important step in developing nanoparticles that can carry therapeutic agents to bone, while being visualized and followed up non-invasively with MRI.

During the experiments of chapter 3, we discovered that the use of biomaterials can alter the signal intensity (SI) at the site of fracture. Many of our analyses are based on the SI of the MR image; therefore, the alteration caused by the biomaterials alone might change the overall MR imaging results. We imaged the biomaterials individually to study how they altered the MR SI before combining them with stem cells. We studied three different biomaterials that are commonly used in stem cell bone therapies; hydroxyapatite (HA), matrigel and purecol.

1.4 *In vivo* detection of stem cells

Stem cells have great therapeutic potential for healing bony defects. However, more must be known about the *in vivo* behaviour of cells, including the cells' effect on healing, and their cellular viability and migration ability before these therapies can be used safely. For instance, transplanting undifferentiated ESCs into mice forms tumours[43]. Conversely, bone marrow stromal cells, which are more differentiated than ESCs, used to heal a bony defect stay at the site of a defect and contribute to bone healing[13]. In order to thoroughly study the different outcomes of different cell types and different treatments, *in vivo* cell detection methods are needed.

An ideal cell detection system is one that is biocompatible, non-toxic, non-invasive, stable over time and sensitive to a small number of cells[11]. It would not affect the studied cells' capacity to proliferate and differentiate. It would not involve genetic modification or ionizing radiation. Lastly, it would not be diluted upon cell division and any contrast agent would not transfer to non-stem cells[10]. A variety of cell detection methods exist; each of them has its own

strengths and limitations. At present, no cell detection method fulfills all the previous criteria[63]. However, multimodality approaches can combine strengths of different modalities[64].

In the GFP modification method, the GFP gene is introduced into the stem cell DNA. This causes the cell to express GFP which can be detected *in vivo* or *ex vivo*[65]. *In vivo* detection of GFP is performed using fluorescent imaging (Xenogen system)[66]. *Ex vivo* detection is done directly by examining the specimen under a fluorescent microscope using the appropriate filters[66], or indirectly by staining for the protein using immunohistochemistry[44]. The advantage of using genetic modification is that genes do not get diluted upon cell division. However, this method has the potential of inducing genetic abnormalities, which makes it hard to translate into humans.

In situ hybridization is done by transplanting male cells into female mice and staining for the Y-chromosome[30]. The advantage of this method is it doesn't involve genetic modification, however it is terminal therefore it does not allow time course studies to be performed.

The most commonly used *in vivo*, imaging-based cell detection methods are µCT, bioluminescence, near infrared, single photon emission computed tomography, positron emission tomography, ultrasound, and MRI. Most of these imaging methods require a labelling material to label the cells or tissues of interest to increase its contrast for proper visualization. The advantage of these methods is their capability to image cells *in vivo* in live animals over a time course. This is important in monitoring regenerative therapies and investigating their outcomes. Each of the previous methods generates images in a different way and therefore has its own strengths and weaknesses. To select the ideal imaging method for a study, it is important to consider the type of tissue being examined and the time course of the study. A brief description of each method follows.

In μCT, an x-rays emitter rotates around an object, projecting radiographs onto a detector on the opposite side. This produces tomographic images of that object that are subsequently reconstructed into a 3D image. It provides high spatial resolution. However, it requires very high concentrations of contrast agent to render a stem cell visible. Such high concentrations of contrast agent adversely affect the health of the host tissue. Host tissue is also negatively affected by the high dose of ionizing radiation used in μCT[64,63].

Bioluminescence is a type of photon emission-based imaging. The light is emitted as a by-product of a chemical reaction such as the luciferin reaction. The utility of bioluminescence imaging in cell tracking is limited due to its shallow tissue penetration and its low spatial resolution[67]. Additionally, it requires the stable expression of introduced genes. It is unlikely to be used clinically because it involves genetic modification of cells[63].

Near infrared imaging involves using fluorescent labelling materials to label the tissue being imaged[68]. Its detection penetration range is only 4 to 10 cm of tissue, limiting its use to near-surface applications[63]. Other disadvantages of this method are that the labelling material dilutes as the cells divide, making it harder to detect the cells *in vivo*[63,68].

Single photon emission computed tomography (SPECT) and positron emission tomography (PET) involve using a radionuclide radiotracer which decays and emits positrons[64]. When positrons encounter an electron while travelling through the tissue, they emit gamma ray which is detected by the gamma camera[64]. Because of the high sensitivity of SPECT and PET, they can detect cells at a very low concentration. The downside of using SPECT and PET is the potential of non-specific uptake of the radiotracer by normal tissue[67].

Ultrasound is a tissue contrast-based imaging technique. It has been used to track stem cells *in vivo*[64]. Ultrasound's benefits are that the machine is inexpensive and portable, the imaging

technique does not involve ionizing radiation and that the image is real-time and dynamic[64]. However, it is less commonly used in for cell tracking due to the unavailability of a long-term ultrasound contrast agent[64].

The last *in vivo* cell detection method and the focus of this thesis is MRI. MRI provides greater soft tissue contrast than μCT and ultrasound and is one of the most commonly used methods for stem cell tracking *in vivo*[10]. Briefly, the animal is positioned in the MRI scanner where a strong magnetic field is applied. A radiofrequency pulse is applied to excite the atoms with spin such as hydrogen atom. Then the excited atoms relax emitting a signal that is received by the receiver coil and then processed to form an MR image. Imaging parameters can be manipulated to highlight different properties of the atomic nuclei, and thereby also of the tissues, being imaged.

MRI cell tracking was introduced in 1993 to look at cell survival and migration after grafting[69]. In 2001, the first *in vivo* time course of cell migration was reported[70]. Later, several *in vivo* studies were done tracking labelled neural cells[69], stem cells[70], and dendritic cells[10]. Current research in proton MR imaging aims at increasing the resolution, improving S/N, and increasing the contrast between the tissue of interest and the surrounding tissue.

Contrast agents are used to increase the contrast between tissue of interest and the surrounding tissues[10]. For example, in an MR reporter gene imaging method, cells were genetically modified to over express ferritin, which is a protein responsible for storing iron within the cells[64]. Thus, iron level increased within the cells and this altered the signal in the MR image[64]. The strengths of this method are that only live cells are visualized and that the label does not get diluted during cell division. A limitation of this method is that genetic modifications involve the risk of genetic abnormalities and tumour formation[64].

Alternately, contrast agents can be used to label the cells to increase their visibility in *in vivo* MRI. The most commonly used contrast agents are based on iron oxide (super paramagnetic iron oxide, SPIO). They cause a negative contrast on MR images, i.e. they cause a localized darkening in T_2 weighted images. The advantage of using SPIOs over positive contrast agents is their higher sensitivity at detection because they generate a very strong localized magnetic field disturbance[10]. The second family of contrast agents is Gd which causes positive contrast in MR images, i.e. members of this family cause a localized lightening in T_1 weighted image. The advantage of using them is that, unlike negative contrast agents, the signal of the underlying tissue is enhanced which improves the visualization of the underlying structures. In this project, we used the most commonly used contrast agents, SPIOs and Gd for cell labelling.

During the cell labelling process, SPIOs are endocytosed by the cell. Both the cell membrane and the SPIOs are negatively charged; therefore the transfection lipofectamine is used to assist the process. Lipofectamine contains positively charged macromolecules which bind to the negatively charged SPIO particles by electrostatic interaction and facilitates their uptake into the cells[71]. Similar to SPIOs, Gd particles have a negatively charged membrane, which dictates the use of a transfection agent at the labeling process.

We previously listed the attributes of an ideal cell detection system. To review, it is one that is biocompatible, non-toxic, non-invasive, stable over time and sensitive to a small number of cells. It would not affect the studied cells' capacity to proliferate and differentiate. It would not involve genetic modification or ionizing radiation. Lastly, it would not be diluted upon cell division and any contrast agent would not transfer to non-stem cells. These criteria hold for both the non-invasive imaging modality and for the cell label. The SPIOs and Gd are dextran coated which makes them biocompatible and safe[10]. The SPIO are more visible than Gd, thus lower

dose of SPIO label can enable cell visualization[55]. Reducing the dose of the label will help reduce its toxic effects. The effect of labeling on the viability and the proliferation capacity of the cells is discussed in chapter 6. The advantage of this detection system is that it doesn't involve any genetic modifications. Though, the label gets diluted upon cell division[10].

By combining the advantages of non-invasive MR imaging with the SPIO and Gd labels, we were able to track labelled ESCs *in vivo*. This opens the door for the development of future therapies for healing of bone injuries[30,72], by allowing an evaluation of their fate after implantation and their possible therapeutic applications. To our knowledge, this is the first study to track labelled stem cells in a fracture model using MRI.

1.5 Aims of the project

Our main goal is to develop an MRI protocol that would allow new tissue engineered therapies to be tested and followed up non-invasively across a time course. This project is composed of five aims. The outline of the project is presented in Figure 1-3.

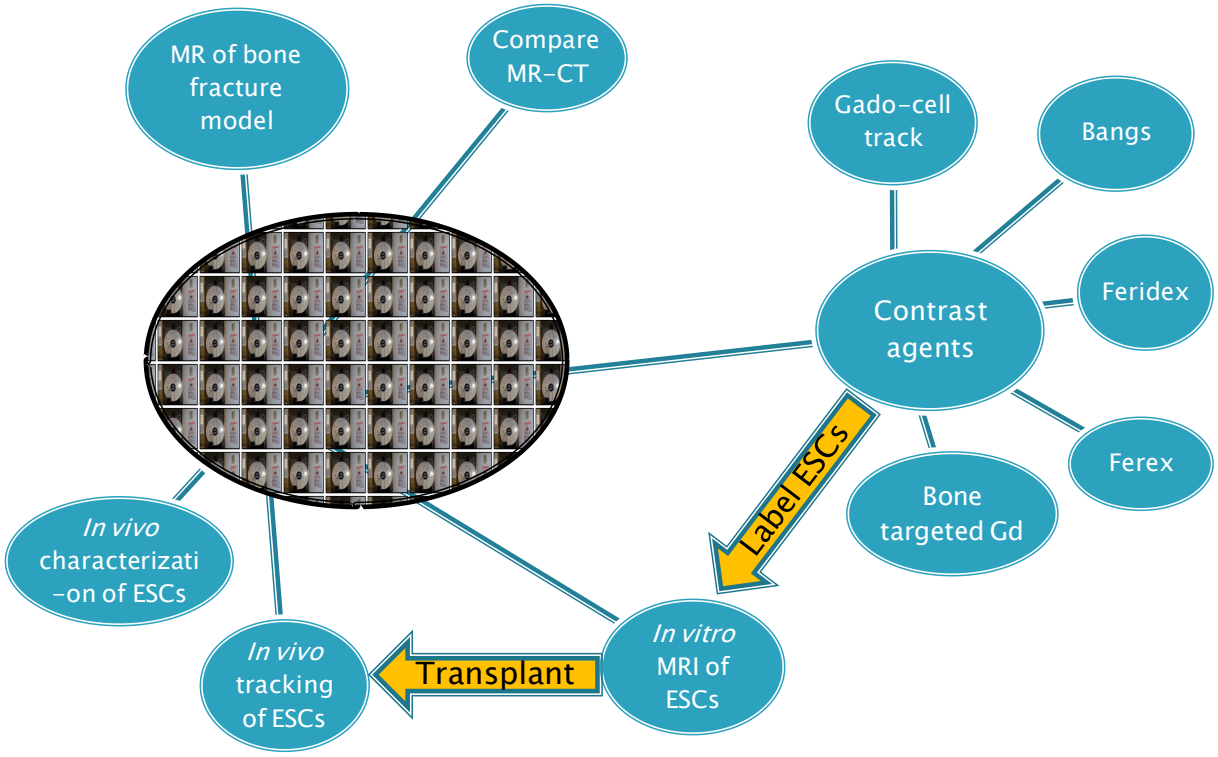

Figure 1-3 A diagram representing the outline of the project.

Aim1: Optimization of MRI for visualizing a mouse bone fracture model, validated using µCT and histology.

MRI of bone fracture in very small animal models such as the mouse can be challenging due to the high resolution required to see the small bones and smaller injuries, and the susceptibility artefacts generated by the bone-soft tissue interfaces. However, the increased availability of a range of MRI sequences makes it possible to overcome these issues. The first aim was to compare MRI sequences in order to select a sequence that had the best combination of resolution, a signal-to-noise ratio, contrast between bone and soft tissue, artefact reduction, and acquisition time. In addition, we compared the ability of MRI and µCT to image bone fracture,

bone marrow, transplanted biomaterial, and the progress of healing. Then, histology was used to validate the imaging results. The data of this aim are presented and discussed in chapters 2 and 3.

Aim 2: MRI of tissue engineered biomaterials used in the treatment of the bone fracture model.

Sub-aim 2.A: Biomaterials used in tissue engineered therapies could change the MRI results by altering the signal intensity at the site of bone fracture. Therefore, our first sub-aim was to study the effects of some common biomaterials on signal intensity in MR images. These data are presented and discussed in chapter 3.

Sub-aim 2.B: We used MRI to test new bone-targeted nanoparticles that were developed by our collaborators in Dr. Uludag's lab as part of a collaborative research project. Our contribution was testing the nanoparticles' efficiency in encapsulating and retaining the contrast agent gadolinium (Gd). If the nanoparticles successfully retained Gd, they could be used as a bone-targeted Gd-based contrast agent. Thus, using them would increase the specificity of contrast agent delivery to bone. It would also decrease the adverse effects of non-specific contrast agent administration such as allergies, hypotension and kidney disease[73]. These data are presented and discussed in chapter 4.

Sub-aim 2.C: We used MRI to compare the efficiency of two relatively new contrast agents (Ferex and Bangs) with the previously used and no longer available contrast agent Feridex. We also verified whether they had enough relaxivity for our project. The data are presented and discussed in the first part of chapter 5.

Aim 3: Labelling of ESCs with different contrast agents and imaging them *ex vivo* to establish an MRI imaging protocol for labelled cells.

ESCs were differentiated into (3D collagen construct) osteogenic lineage and labelled with different contrast agents at different concentrations to develop an ideal labelling protocol for the cells. An ideal labelling protocol was considered to be one that did not adversely affect the cells' proliferation or differentiation capacity and has enough sensitivity and stability to be detected with MRI even after cell division. Then, the labelled cells were imaged *ex vivo* using MRI to determine the number of labelled cells needed to be visualized in MRI. These data are presented in chapter 6.

Aim 4: Implanting and MRI tracking of ESCs *in vivo* in muscle and at the site of bone fracture.

In the first stage of the *in vivo* work, labelled ESCs, suspended in culture media, were injected into the thigh and the gastrocnemius muscle of uninjured mice. This was done to track the labelled cells against a clear background before moving to cell tracking in the fracture model. In the second stage of the *in vivo* work, dESCs (differentiated ESCs) in 3D collagen constructs were implanted in the bone fracture model to provide the cells with the needed mechanical support at the site of bone fracture[44]. Our aim was to track the labelled cells *in vivo* with serial MR imaging. The data of this aim are presented and discussed in chapter 7 and 8.

Aim 5: Histological characterization of the transplanted, labelled cells *in vivo* by staining for macrophages, GFP (Green fluorescent protein)-labelled cells, Y-chromosome-labelled cells and iron.

A key step towards developing cell therapies that are effective and safe is to study whether transplanted cells migrate, proliferate, die or integrate into the host tissue. In this aim histological and immunohistochemical protocols were used to verify the data obtained from the MR images.

One of the possible fates of transplanted cells is migration. We used Y-chromosome *in situ* hybridization and GFP immunohistochemistry staining protocols to identify the location and distribution of the transplanted cells among the tibial shaft, bone marrow and control fracture. Prussian blue staining of consecutive sections was performed to co-register the location of iron with the location of the implanted cells. This was done to determine whether iron was still inside the implanted cells.

Upon death, the transplanted, labelled cells expel the iron label, which gets phagocytosed by host tissue macrophages[74,75]. Accumulation of labelling iron in host macrophages could lead to false positive results in the MR image, i.e. giving inaccurate information about the location of implanted cells. We stained for macrophages and iron to determine if iron label had accumulated in macrophages. The data of this aim are presented and discussed in chapter 8.

Chapter Two: **MRI background, selection of coil, sequence and parameters to best-visualize a mouse bone fracture model at 9.4T**

In the first section of this chapter some basic MRI principals will be introduced to provide the needed background for using MRI. The second and third sections of this chapter have experimental work that aims to optimize a combination of coil, sequence, and parameters that will allow us to image the mouse fracture model using MRI. The MRI protocol developed in this chapter will be used will be used in the remainder of the thesis.

2.1 Basic principles of MRI

2.1.1 Introduction to important considerations for MR imaging

In this section, I will discuss the important criteria that should be considered for MR visualization of the bone fracture model. I will start with a brief explanation of the basic concepts behind MR imaging. Then, I will give more details about the most noteworthy parameters in MRI which will be used in our study. A good understanding of this knowledge is the key to optimize MRI sequence for best-visualization of bone fracture model. Essentially, in order to see the bone fracture, we need good contrast between bone, soft tissue, and implanted therapy. We also need good signal to noise (S/N) and little artefacts, since artefacts can obscure important information in the image. Also, it is equally important to optimize the acquisition time to a reasonable time frame since mice are under anesthesia. Moreover, the reproducibility of imaging was important for following up the same region of interest (ROI) longitudinally.

The goals of the experiments in this chapter are to select the imaging conditions that provide the best visualization of the fracture possible, specifically MR coil and MR imaging sequence and parameter selection. First, I will discuss coil selection (Section 2.2). Then, the selected coil will be used for the second experiment which is sequence and parameter selection (Section 2.3).

2.1.2 A brief background on how atomic nuclei behave during MR imaging and how MR images are formed

MRI uses the absorption and emission of electromagnetic waves in the radiofrequency range to form tomographic images[54]. Depending on what is being imaged, different pulse sequences (i.e. ways of administering and collecting the radio waves) can be selected that collects specific kinds of information collected and the signal intensity of that information can be optimized[54]. We will first describe in more detail how the image is created in MRI in order to provide the information required to understand the pulse sequence selection process. Then, in Section 2.3, we will describe how we chose the pulse sequence, and the parameters within it, to best image our animal model of bone fracture.

The components of an MRI scanner are the main magnet (B_0), the radiofrequency coil (B_1), the three gradient coils and the working console[55] (Figure 2-1).

Figure 2-1 A photograph of a 9.4 T MRI magnet. The gradient coils surround the hole in the centre of the main magnet and are obscured by the beige exterior of the main part of the machine. The console and the radiofrequency coil are not visible in this image.

The main magnet creates a static magnetic field which influences any atomic nuclei that have a net spin (Figure 2-2). The hydrogen atom is most abundant atom in the body[48], is the most

used nucleus in MRI[48], and is the nucleus used to generate images in this thesis. Some of the nuclei will have their magnetic moment aligned in the z-direction while others will align against it[54]. However, the net magnetization is always in the z-direction[54].

The static magnetic field influences the magnetic moment of the nuclei and will make them precess around the field[54]. The frequency of precession is described by Larmor equation[54]

$$\omega_0 = B_0 \times \lambda$$

Where B_0 is the main magnetic field strength and λ represents the gyro-magnetic ratio (the ratio of the magnetic moment of each nucleus to the angular momentum of the net spin of nuclei.

An RF pulse with a frequency exactly equal to Larmor frequency of the hydrogen nuclei, can excite them and consequently tilt the net magnetization vector away from the z-direction[54] (Figure 2-2). After the magnetization is tilted is done, the nuclei will start to dissipate their energy and relax to their equilibrium state, i.e. aligned with B_0, by producing a free induction decay (FID) radiofrequency signal[54]. This relaxation process involves three mechanisms; spin-lattice relaxation, spin-spin relaxation, and a third relaxation mechanism associated with dephasing, which will be explained in more detail in the next section[48].

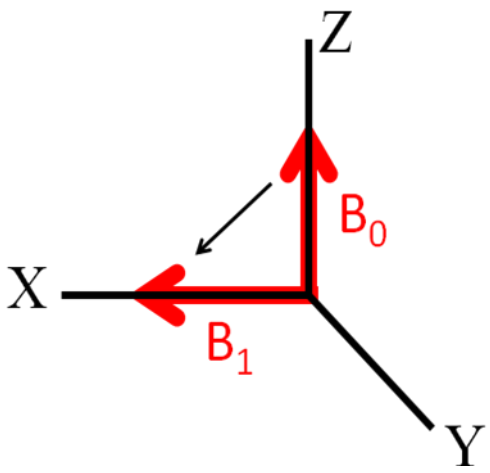

Figure 2-2 The tipping of the spin from the B_0 direction to the B_1 direction following the excitation pulse emitted by the radiofrequency coil.

The FID is detected by a receiver RF coil[54], which may or may not be the same as the excitation RF coil. While the spins are returning to equilibrium, the gradient coils are used to apply gradients in three different, orthogonal directions: G_x, G_y and G_z. These gradients are used to determine the 3D location of the signals emitted from different tissues[54]. Finally, after the spatially-encoded signal is detected by the receiver RF coil, it is transferred to the work station to be Fourier transformed and processed to form an image[54]. The entire FID is not used in image formation. Instead, only the signal at a specific time after the initial RF pulse is collected. This time between the RF pulse and signal collection is known as the echo time (TE)[54]. The image is also not obtained from a single repetition of this process; in fact many dozen repetitions are often needed to form images. The time taken to repeat this process is called repetition time (TR)[54]. Lastly, the net spin of the nuclei are not always tipped all the way into the transverse (i.e. x-y) plane (Figure 2-2). The flip angle refers to the angle between the z- (longitudinal) plane and the resultant angle of the spins[54].

*2.1.3 T_1, T_2 and T_2**

As mentioned above, the relaxation process is divided into three parts: the spin-lattice (T_1 or longitudinal) relaxation, the spin-spin (T_2 or transverse) relaxation, and the relaxation mechanism associated with dephasing which has a T_2 component in it (T_2*). Longitudinal relaxation (T_1) is the time taken for the net magnetization in the z-direction (M_z) to recover to 63% of the equilibrium value (M_0) (Figure 2-3). T_1 is governed by the following equation[54,76]:

$$M_z = M_0\ (1 - exp^{-\frac{t}{T_1}})$$

where M_z is the net magnetization in the z-direction and M_0 is the magnetization in equilibrium state. T_1 occurs when the spins give up the energy they obtained from the RF pulse to the surrounding lattice, subsequently, returning back to their equilibrium state.

Transverse relaxation (T_2) is the time taken to reduce the transverse magnetization by 37% of its original value (Figure 2-3). Molecular interactions are responsible for the decay in the transverse plan. For any given tissue T_2 is always shorter than T_1. T_2 is governed by the following equation[54,76]:

$$M_{xy} = M_{xy0}\ (1 - exp^{-\frac{t}{T_2}})$$

where M_{xy} is the net magnetization in the xy plan and M_{xy0} is the equilibrium magnetization in the xy plan.

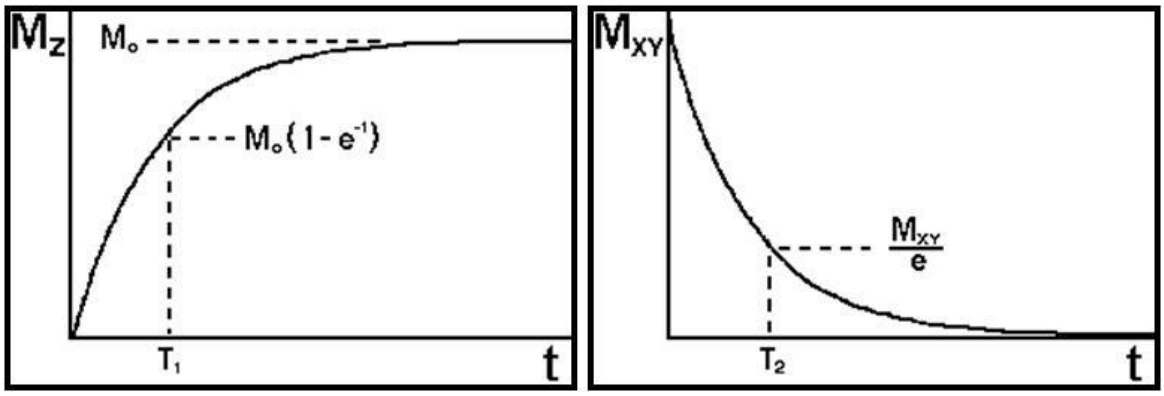

Figure 2-3 A diagram representing the T_1 and T_2 relaxation processes (reproduced from Hornak)[54].

As mentioned above, decay of magnetization in the transverse plan is affected by two factors: molecular interactions and the inhomogeneity of the main magnetic field. The combination of these two factors is the T_2 star time constant (T_2*). The relationship between T_2 and T_2* is represented in the following equation[54]:

$$\frac{1}{T_2^*} = \frac{1}{T_2} + \frac{1}{T_2'}$$

T'_2 is the effect of the inhomogeneities of magnetic field.

2.1.4 Generating MR weighted images and maps

Commonly, MR images have contrast based on the tissue parameters T_1, T_2 and proton density (along with other properties such as field inhomogeneity). Imaging parameters such as TR, TE and flip angle are manipulated so as to enable one of the tissue parameters to dominate the other[48]. This type of image is called a weighted image. A T_1 weighted image is generated by using a short TR and a short TE, the short TR is used so that it is shorter than the T_1 relaxation times of tissues, and the short TE is used to collect the signal before the spins start to dephase. On the other hand, a T_2 weighted image is generated by using a long TR and a long TE, the long

TR is selected to allow complete T_1 relaxation and thus eliminating all the T_1 effects, the long TE is selected to collect the signal while the spins are dephasing which highlights the difference in T_2 relaxation times of the tissues. T_1 weighted images require less acquisition times than T_2 weighted images. Lastly, to create a proton density weighted image, a long TR and a short TE is used to reduce the T_1 and T_2 effects on image.

Fluids have longer T_2 relaxation times than bone. Therefore, in a T_2 weighted image, fluids produce more signal than bone, and thus they appear bright which makes a T_2 weighted good for showing oedema. Similar to T_2 weighted image, in a proton density weighted image, the fluids appear bright and bone appear dark.

2.1.5 A brief background on MRI sequences

The term "MRI sequence" refers to a specific combination of RF pulses and gradients[48]. The most commonly used MRI sequences are based on spin echo (SE) and gradient echo (GE) sequences[48]. They can be used to generate T1, T2 and proton density weighted images. The SE sequence is made up of a 90-degree excitation pulse followed by a 180-degree rephasing pulse[48]. The 180-degree rephasing pulse reduces the effect of field inhomogeneity[48]. Therefore, SE sequence can be used when field inhomogeneity is causing artefacts that obstruct the visualization of structures in the image. The GE sequence differs in two ways from SE sequence. First, the excitation pulse in GE is usually less than 90^{o}[77]. This means that it takes less time for spins to relax, and TR can be shortened without losing too much signal. Second, the GE sequence uses a magnetic field gradient to rephase the spins, instead of the 180-degree rephasing pulse used in SE sequences[48]. This means that the resulting image is more prone to artefacts generated by field inhomogeneity. Therefore, GE sequences trade off greater speed with more artefacts due to field inhomogeneity[78].

Manipulating the parameters TR and TE can offer different types of contrast between tissues, or shorten the imaging times[48]. Often, these parameters could be traded off against each other to optimize the imaging sequence[48].

Another important MRI concept is the MR mapping. It is used to measure T_1 or T_2 values of a specific tissue. Simply, it is repeating the same pulse sequence with variable TR or TE values to generate a range of images. After that, the images are processed to obtain an MR map where each voxel contains a quantified value of this voxel across all the images instead of relative signal intensity. For example, a T_1 map can be created by using a RARE (Rapid acquisition with relaxation enhancement), inversion recovery or True FISP[79,80] (Fast imaging with steady state precession) sequences with variable TR and a fixed TE. The variable TR will allow variable amounts of T_1 relaxation in each image. Also, a T_2 map could be generated using a Carr Purcell Meiboom Gill (CPMG) a spin echo based sequence with variable TE to obtain images with variable T_2 weighting. To measure T_1 or T_2 values, the signal intensity of the tissue of interest is plotted as a function of TR or TE values, respectively. The obtained T_1 or T_2 relaxation curve is used to fit a mathematical function that will calculate the T_1 or T_2 relaxation times[81].

2.2 Coil selection

2.2.1 Introduction

Radiofrequency (RF) coils are needed to transmit pulses into the sample and receive signal back[54]. Their designs are varied, and the design influences factors such as S/N and RF homogeneity[54]. As a generalization, surface coils tend to be closer to the sample and have high signal/noise. However they have very poor RF homogeneity and so both the transmitted power as well as the received signal falls off with distance from the coil. This is not ideal for sequences with complex pulse shapes. Volume coils are shaped more like a cylinder and the RF power and

sensitivity is more evenly distributed over space. Quadrature coils (volume or surface) (Figure 2-4 A) have two coils within the geometry, operating at 90º out of phase from each other[82]. They increase the S/N by $\sqrt{2}$. This is a common clinical coil. Based on theoretical principles a solenoid approximates the most homogeneous in terms of RF sensitivity and has the highest S/N for a volume type configuration[83]. The solenoid is shaped like a tube, of a single sheet of metal (Figure 2-4 B). The disadvantage of the solenoid is that it is oriented across the magnetic field and not along it[84]. The sample has to be oriented across the bore of the MRI[84]. For our small limb imaging, this was a very appropriate configuration as the mouse leg could be moved into a cross-bore position without causing additional discomfort to the animal. An optimal coil for our study would be one that provides the highest signal to noise ratio among the other coils compared in this study. Additionally, it would provide a homogenous magnetic field within the coil. The two previously mentioned characteristics will aid in obtaining good quality MRI images where signal is homogenous and noise is minimal.

2.2.2 Methods

Experiments were approved by the Animal Care Committee of the institution. Bur-hole injuries were created in one mouse as follows; the mouse was anaesthetized with isoflurane, and then was given buprenorphine [0.03 mL] and penicillin [0.01 mL] *i.p.* prophylactically as analgesic and antibiotics, respectively. Surgery was performed unilaterally[85]. Briefly, an incision was made along the medial aspect of the tibia. The bone surface was exposed by dissecting the periosteum. Using a sterile dental drill with a 0.5 mm cutting bur, multiple holes were drilled into the tibia approximately 3 mm apart and to a 1mm depth across the cortical bone until the opposite cortex was reached[86]. The surgical incision was sutured.

MR imaging was approved by the Experimental Imaging Centre's Scientific Review Committee, Faculty of Medicine, University of Calgary. A 35 mm quadrature coil and a solenoid coil (manufactured in Institute of Biodiagnostics, in Winnipeg) were used. A mouse was put in each coil and imaged. We used a RARE, FISP and FLASH sequence (the sequences will be discussed in Section 2.3) with TR/TE 1250/7.5, 4/2 and 100/4 ms, respectively.

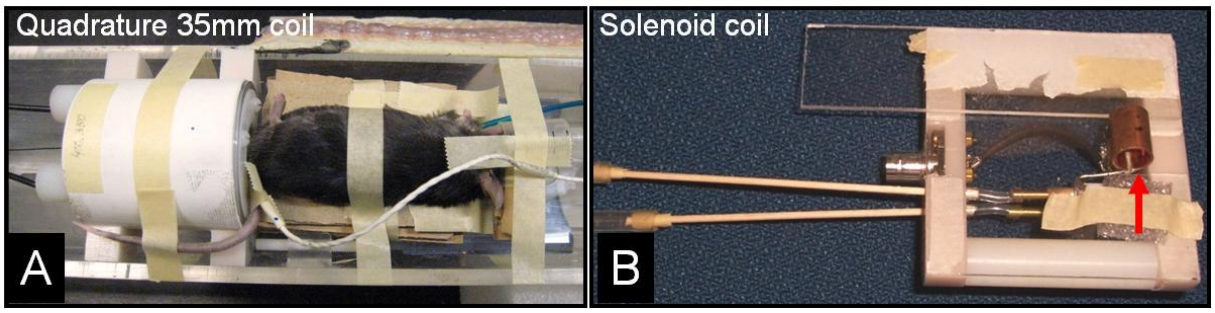

Figure 2-4 MRI coils used to image the mouse bone fracture. (A) Quadrature coil (35 mm). (B) Solenoid coil (1.5 cm length, 0.7 cm internal diameter). Bothe coils were tested for leg imaging.

2.2.3 Results

The leg of the mouse fitted in the solenoid coil. Subsequently, the region of interest was centralized in the middle of the coil. Conversely, it was hard to fit the leg of the mouse in the quadrature coil because the body of the mouse was interfering with further insertion of the leg into the coil, which made the leg off centered during imaging.

When we visually inspected the generated images from both coils, the images from the quadrature coil were off centered while those from the solenoid coil were centered and the field of view (FOV) contained the region of interest.

2.2.4 Conclusion

The solenoid coil fitted our mouse model better than the quadrature coil, which enabled the centralization of the region of interest at the centre of the coil. When the FOV is filled with tissue, this increased the emitted signal from the FOV, and consequently, gave high S/N ratio[83]. Also, for the reason that the solenoid coil is a highly efficient transmitter receiver coil, this decreases the RF load on the tissues while still providing good anatomical resolution [83]. The solenoid coil is characterized by a higher RF homogeneity within the resonator than quadrature coils[83] which minimizes the artefacts caused by field inhomogeneity. On the other hand, increasing the FOV as in case of the quadrature coil, increases the S/N. However, this is compensated in the solenoid coil by the good S/N ratio provided by the field homogeneity maintained within this coil. In conclusion, the solenoid coil fitted our model nicely and provided good S/N ratio associated with field homogeneity. Consequently, we used it for imaging the bone fracture model in our study.

2.3 The selection of MRI sequences and parameters for imaging of the bone fracture model

2.3.1 Introduction

The second step in the development of a non-invasive tracking system for cell therapies was the selection of an MRI sequence and parameters that allowed us to visualize the fracture in an amount of time that was tolerated by the mice being imaged. The MRI sequence that is most commonly used in MSK imaging is the spin echo sequence[87]. The Rapid Acquisition with Relaxation enhancement-spin echo sequence (RARE) sequence is a spin echo-based sequence in which a 90-degree pulse is applied followed by a train of rephasing 180-degree pulses. The advantage of this sequence is that the acquisition time is reduced by a factor of the echo train length or the RARE factor. For example, when using a RARE factor of 9, the acquisition time is

one ninth of the time it would have otherwise been. Because it is based on an SE sequence, it is not as prone to susceptibility artefacts (i.e. artefacts caused by field inhomogeneity) as the gradient echo methods. RARE also has increased S/N ratio compared to a standard spin echo for a given acquisition time.

Gradient echo sequences also show promise for MSK imaging. The Gradient Echo-Fast Low Angle Shot sequence (GE-FLASH) sequence combines a small flip angle with a TR that is shorter than the typical T_1 time for the tissue. The short TR results in speeding the entire image acquisition[88]. The True Fast-Imaging with Steady State Precision-gradient echo sequence (True-FISP) is similar to GE-FLASH except that TR is shorter than T_1 and T_2.

Susceptibility-weighted imaging (SWI) is a relatively new method to increase contrast in MR imaging. It enhances the contrast between tissues by using differences in tissue susceptibility to produce a new contrast[89,90]. It is commonly done based on GE sequences because they are more sensitive to susceptibility effects[91], however in some studies it was done based on a SE sequence as well[92]. It is done by combining the phase and the magnitude images to obtain a susceptibility-weighted image[89,90]. It is based on eliminating the unwanted phase artefacts and keeping only those of interest. SWI can be used to increase the sensitivity of the imaging to lesions[91].

We compared the RARE, GE-FLASH and True-FISP sequences for imaging our mouse fracture model. In a separate series of experiments, we also investigated whether SWI would give us additional information. Our goal was to find a sequence and parameters that would give the best combination of high signal-to-noise ratio, contrast between tissues, short imaging times, and minimal artefacts.

2.3.2 Methods

Four female mice, 4-6 weeks old, Sv129 mice (Jackson Laboratory, U.S.) were prepared as per our standard surgical protocol in Section 2.2.2. Animals were imaged 24 hours after the surgery to determine the strengths and limitations of three different MRI sequences: GE-FLASH, True-FISP, and RARE. SWI imaging was also tested, but separately. The protocol follows below. The MRI machine used in this study was a high magnetic field (9.4 T), 20cm horizontal bore Magnex magnet controlled by a Bruker Avance console system. To test the imaging sequences (GE-FLASH, True-FISP, and RARE), two mice were used and the sequences were repeated twice on each of them. A third mouse was used to try the different weighting of the RARE sequence. Then, a fourth mouse was used for the SWI processing experiment. The parameters of the three sequences are presented in Table 2-1.

Table 2-1 MRI parameter of GE-FLASH, True-FISP and RARE T_1 images presented in Figure 2-5.

Parameter	GE-FLASH	True FISP	RARE SE
Field of view (FOV)	1.28x1.28 cm	2.56 x 2.56 cm	1.28 x 1.28
TR/TE	200/4 ms	4/2 ms	1250/7.6 ms
Number of averages (NA)	12	20	10
Matrix	256 x 256	128 x 128	256 x 256
Slice thickness	0.5 mm	0.5mm	0.5 mm
Resolution	50x50x500 µm	200x200x500 µm	50x50x500 µm
Echo train length (ETL)	NA	NA	4
Pulse angle	30º	20 º	NA
Acquisition time	10 min. 14 sec	10 min	10 min

After investigation of the images generated by the three sequences, the RARE sequence was selected for imaging of the bone fracture model. Subsequently, an estimate of optimum RARE parameters were iteratively determined by imaging the same animal with a range of TR/TE's and number of averages. The parameters tested were TR/TE; 500/7.6, 2000/7.6, 2000/20 ms for a T_1 weighted image, proton density image, and T_2 weighted image respectively. The acquisition time for each image was approximately 19 minutes.

In a separate series of experiments, we compared SWI and RARE sequences. One mouse was prepared as described above. MR images of the mouse were obtained using RARE sequence, TR/TE 2000/20. An extra processing step was performed on the RARE sequence to obtain the SWI. Phase and magnitude images are obtained from the Bruker console. Spin software was used to process the phase and magnitude images into an SWI. SWI and RARE images were compared visually to determine whether SWI gave more information than RARE images.

2.3.3 Results

The bur-hole injuries were detected as hypointense areas within the marrow region and as interruptions of the dark line of the cortical bone. They could be readily seen in the RARE images (Figure 2-5 C). GE-FLASH and FISP had higher susceptibility artefacts and hypointense areas surrounding the sites of injuries making it hard to detect the fractures (Figure 2-5 A & B). The True-FISP sequence showed significant banding artefacts caused by field inhomogeneity. The banding in the FISP image could potentially be reduced, however, it would still have limited our ability to visualize bone. We concluded, based on qualitative assessment of the three different MRI sequences used, that RARE produced the best contrast between bone and

surrounding tissues and the least artefacts. It was selected as the pulse sequence for imaging the bone fracture model.

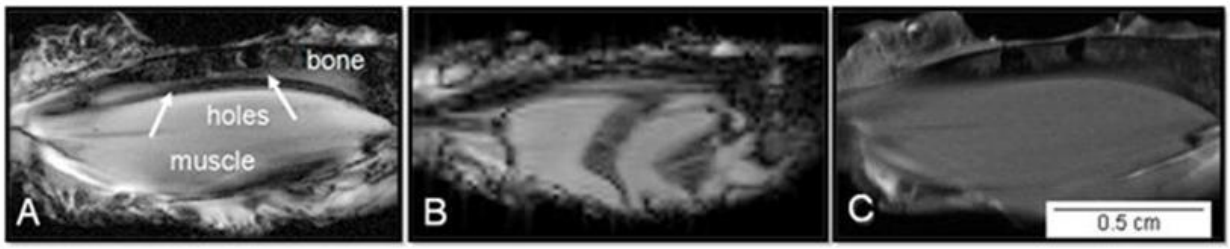

Figure 2-5 A, B & C are example MR images from the same mouse leg with three MRI sequences (A) GE-FLASH, (B) TRUE-FISP, and (C) RARE T_1. For parameters see Table 2-1.The foot is to the left and the pelvis to the right. The tibia runs along the top of the image and the gastrocnemius muscle makes up the bulk of the tissue.

Among the different RARE parameters tested, all showed the holes in the bone (Figure 2-5). Since the ultimate goal of the study, is to track labelled cells in the bone fracture model, the RARE T_1- weighted image and the RARE T_2-weighted image will be used interchangeably for the remainder of this study, according to the type of contrast agent used whether T_1 or T_2 contrast agent. The parameters of RARE T_1 and RARE T_2-weighted image are TR/TE 500/7.6 and 2000/20 ms, respectively, RARE factor = 4. This resulted in an acquisition time of 19 min.

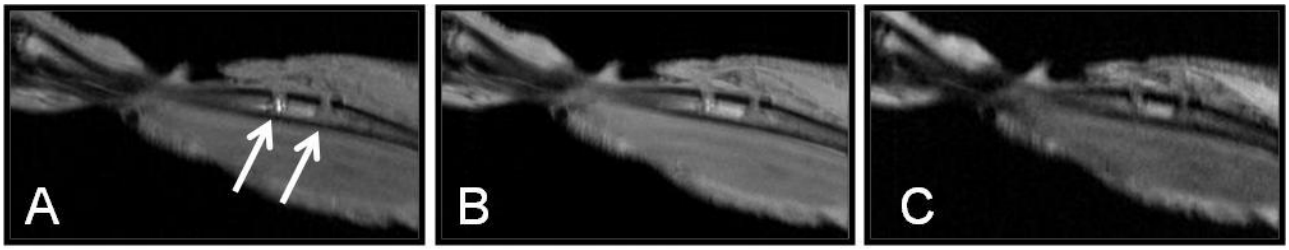

Figure 2-6 A, B & C are RARE images of bone injuries with different weightings. (A) T_1 weighted image, (B) proton density image, and (C) T_2 weighted image. Two bur-hole injuries were drilled in the tibia and both are visible with each set of parameters as noted by the arrows in (A).

By comparing the MR images from our standard RARE protocol (Figure 2-7 G&H) with the SWI processed images (Figure 2-7 E&F), it was shown that SWI increased the contrast between tissues. However, it did not more information than our standard RARE protocol.

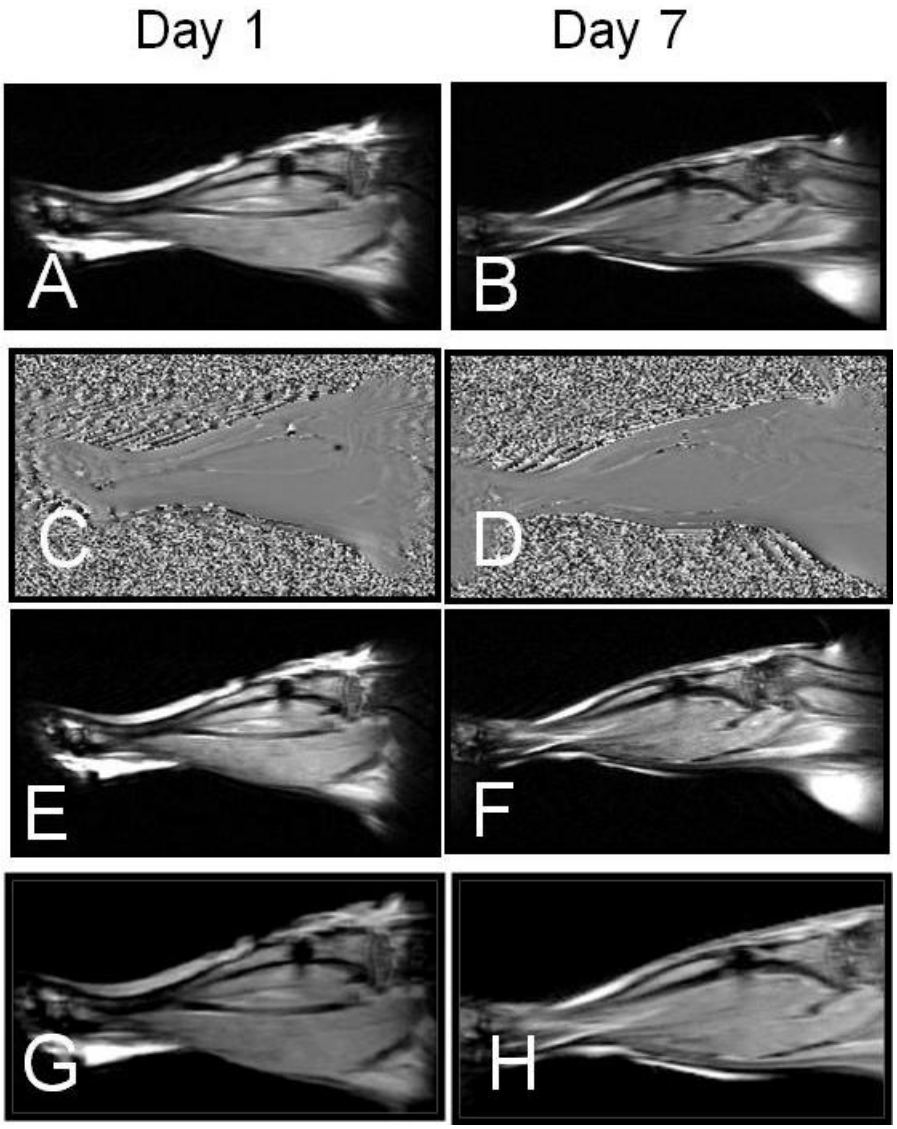

Figure 2-7 Images of a mouse leg with a bone fracture with iron-labelled cells. A & B are magnitude images, C & D are phase images. E & F are SWI obtained by combining the magnitude and the phase images together. G & H are RARE images of the same mouse.

2.3.4 Conclusions

Based on the MRI results, RARE proton density is the sequence of choice for this study. RARE provided good contrast between the soft and hard tissue and enabled the visualization of the fractures clearly. It had minimal artefacts compared to the other sequences used. Lastly, we were able to acquire RARE images in a reasonable acquisition time, i.e. the short acquisition

time allowed a superior recovery of the mice from anaesthesia after the imaging sessions. The strengths of the RARE sequence are the lack of susceptibility artefacts in the images and the good contrast provided between the tissues[77].

SWI based on RARE sequence did not provide any more information than the standard RARE imaging. This might be due to the insensitivity of the RARE sequence to susceptibility effects[91]. Possibly, if SWI was done based on GE, it would have provided additional information. Nevertheless, GE sequence is not the scope of this study because of the generated images artefacts that obstructed the visualization of the bone fracture model. Therefore, the extra processing steps done to obtain SWI processed images are not needed in this project, and consequently SWI was not performed in the rest of the study.

Therefore, we selected RARE as the sequence of choice for this thesis. RARE could additionally be used in humans for assessing bone fracture repair and for evaluating tissue engineered-based therapies *in vivo*, non-invasively.

Chapter Three: **MR imaging of bone fracture repair and of biomaterials used as stem cell scaffolds and its validation using µCT and histology**

The aim of this chapter is to compare MRI with µCT to determine whether MRI could be used to track tissue changes of bone fracture repair using high-resolution µCT as a standard. Moreover, we wanted to study the effects of some biomaterials, commonly used in bone regenerative therapies, on signal intensity in MR images.

The following chapter is a modified version of a manuscript published in the Journal of Magnetic Resonance Imaging. For this manuscript May Taha contributed to the experimental design, data collection, data analysis and manuscript preparation. The part of the original manuscript that compares RARE, GE-FLASH and True-FISP and discusses their optimization was presented and discussed in chapter 2. Thus, this part has been removed from this chapter. Additional information appears in this chapter that was not in the original manuscript due to space constraints. The title of the manuscript is Assessment of the Efficacy of MRI for Detection of Changes in Bone Morphology in a Mouse Model of Bone Fracture[27].

3.1 Introduction

Non-invasive imaging is needed to study bone repairing treatment approaches and to follow outcomes in animal models as well as in patients. Previous studies have demonstrated the potential of tissue engineered therapies to promote healing of skeletal injuries, but further animal studies are required to optimize such treatments[6,7,32,39,93]. Micro-computed tomography (µCT) is a well-established tool for assessing bone healing[94]. However, the ionizing radiation emitted during µCT imaging becomes hazardous when a research subject or animal needs to be examined repeatedly[95]. By contrast, magnetic resonance imaging (MRI) is based on non-ionizing

radiation and can be used for repeated examinations. It also highlights soft tissues, including bone marrow, periosteum, and surrounding muscles.

Studies of animal models are required to determine optimum treatment approaches including the potential use of stem cell therapies[93, 32,39,93]. We used the murine model because a similar model has been used previously to study many aspects of bone repair. It was used to provide a standardized environment for studies on induction and remodelling of trabecular new bone in normal and genetically engineered mice[86,96], to test a new method for differentiating ESCs into osteoblasts, to promote bone healing[30]. Thus, it was important to develop a tool for assessing new therapies in bone and study their outcome.

MRI is challenging for studying injuries in bone, especially in very small animal models such as the mouse. This is due to the high resolution required and the susceptibility artefacts generated by the bone-soft tissue interfaces. We are using this bone fracture model to provide a new optimized imaging modality for assessing bone healing in an already well-used system. It also gives an insight on the effect of tissue-engineered based therapy on the bone marrow and surrounding soft tissue. The increased availability of a range of MRI sequences might make it possible to overcome this issue, but standard protocols have yet to be developed.

Various materials have been used previously to improve bone repair[6,7,97,98] and to carry stem cells, which also have been shown to improve bone healing[97]. These materials are important in tissue engineered-based bone healing therapies, for example, matrigel and purecol have been used as carriers for stem cells[33]. Hydroxyapatite (HA) has been shown to contribute to bone formation by providing an alternative to bone grafts[8]. Therefore, studying the effects of these biomaterials on bone healing is crucial. However, monitoring the behaviour of these biomaterials *in vivo* non-invasively is challenging. Therefore, optimizing imaging modalities such as MRI and

µCT, which can monitor these biomaterials *in vivo*, will be of great importance. It will pave the way for using these biomaterials in human therapeutic applications and be able to monitor them during the healing process.

The primary goal of this study was to compared the ability of MRI and µCT to image bone fracture, bone marrow, transplanted biomaterial, and the progress of healing, then we compared the imaging results with histology to understand the association between histological and imaging observation and to verify the imaging outcomes. Therefore, it is important to correlate the stages of healing in histomorphological findings with the observations obtained from imaging.

3.2 Materials and methods

Animal model. Bone injuries (holes) were made as described in chapter 2.3.2. Twelve mice were used to compare MRI and µCT. The mice were divided into three study groups based on the type of biomaterial used to fill the bone fracture site and the number of holes drilled in the tibia, as described below. Animals were scanned at days 1 & 14 (groups 1 & 2) or days 1 & 13 (group 3). Two animals from each group were sacrificed immediately after MRI and tissues removed for histology.

In group one (n=4)**,** three holes were drilled into the right tibia. The proximal hole was not filled (control hole); the middle hole was filled with hydroxyapatite (HA) (BD Biosciences, Canada) using forceps; and the third hole was filled with matrigel (100 µl of BD Matrigel in 8-9 mL of DMEM/F-12) using a scalpel and needle tip.

In group two (n=5), three holes were drilled and filled similarly to group one, but the third hole was injected with purecol bovine collagen I (3.0 mg/mL, pH 2.0, Advanced Biomatrix,

USA) instead of matrigel. The pH of purecol was adjusted to 7.2. To form the gel, the solution was warmed to 37ºC[99].

In group three (n=3), two holes were drilled. The proximal hole was filled with embryonic stem cell (ESC)-derived osteoblasts in purecol collagen matrix. The ESCs were isolated from male Sv129 mice. Purecol was prepared as a 3-dimensional (3D) gel using 10mM beta-glycerol phosphate (BGP). Specifically, 80% v/v 3mg/mL purecol solution was mixed with a single ES cell suspension (1 million cells/mL) and 20% v/v BGP dissolved in 5X concentrated DMEM (Invitrogen)[99]. The produced gel was applied on top of the hole using a scalpel and then tucked into the hole using a needle tip. The distal hole was left empty.

High resolution MRI

Hardware -- MRI was undertaken using a 9.4T, 20cm horizontal bore Magnex magnet with a Bruker Avance console. A custom built loop gap resonator coil (slotted tube solenoid) (1.5 cm length, 0.7 cm internal diameter) was used because it provided a high signal to noise (S/N) ratio and a uniform magnetic field, as discussed in Section 2.2. The coil was oriented perpendicularly to B_0. The body of the mouse was aligned along B_0 and the leg was positioned within the solenoid coil[100,101].

Imaging Sequences – The MRI pulse sequence used was RARE proton density weighted sequence was selected for imaging of the bone fracture model. The optimum parameters were TR/TE= 2000/7.6 ms, matrix = 256 x 256, FOV= 1.28 x 1.28 cm and RARE factor = 4. This resulted in an acquisition time of 19 min.

Micro CT. All µCT images were acquired using an *in vivo* µCT scanner (vivaCT40, Scanco Medical, Brüttisellen, Switzerland). For Groups 1 and 2, the images were acquired with a

resolution of 12.5 μm and integration time of 200 ms, while for Group 3 the resolution was changed to 10.0 μm. The scanning time was 19 min.

For 2-dimensional (2D) visualization, we present gray-scale μCT images of a longitudinal section of the bone. For 3D visualization of the bone only, the μCT images were Gaussian filtered (sigma=1.2, support=1) and segmented so that only voxels with attenuation greater than 25.5% of the maximum gray scale value were included.

Image alignment. *In vivo* high resolution MRI and μCT images were compared side-by-side for the same mouse, at the same time point, to contrast both imaging modalities. The comparison was based on number of visible holes, appearance of bone, bone marrow, surrounding soft tissue, transplanted biomaterial, and the progress of healing.

Histology. Histology was performed at the same time points as the imaging. Mice were euthanized using euthanyl (Bimeda-MTC, Cambridge, ON). Tibiae were fixed in 10% NBF (Sigma Aldrich, USA), decalcified with Cal-Ex II (Fisher Scientific, USA) and embedded in paraffin. 10 μm sections were stained with hematoxylin Gills III stain (VWR, Canada) and Harleco eosin Y solution (1% alcohol) (EMD chemicals Inc. NJ). An Olympus microscope was used to acquire the histology images.

3.3 Results

MRI Longitudinal study -- The muscles, bone marrow and bone were detected in MRI, allowing us to verify that the fracture did not extend through the cortical bone on the opposing side. At day 1, 16/17 bone injuries in all study groups were detected using MRI. One hole was missed in MRI, which could have been due to the curvature of the tibia (Figure 3-1). Each fracture appeared as a gap in the hypointense line that represents the cortical bone, had

hyperintense spots in the medullary space, and had hyperintensities in the surrounding soft tissue which suggested edema[102] (Figure 3-2 A & G). In contrast, at day 14, MRI showed continuity of the hypointense line that represents the cortical bone. It also showed changes in the signal intensity in the medullary space and the surrounding soft tissue, and the skin and muscles appeared intact (Figure 3-2 D & J).

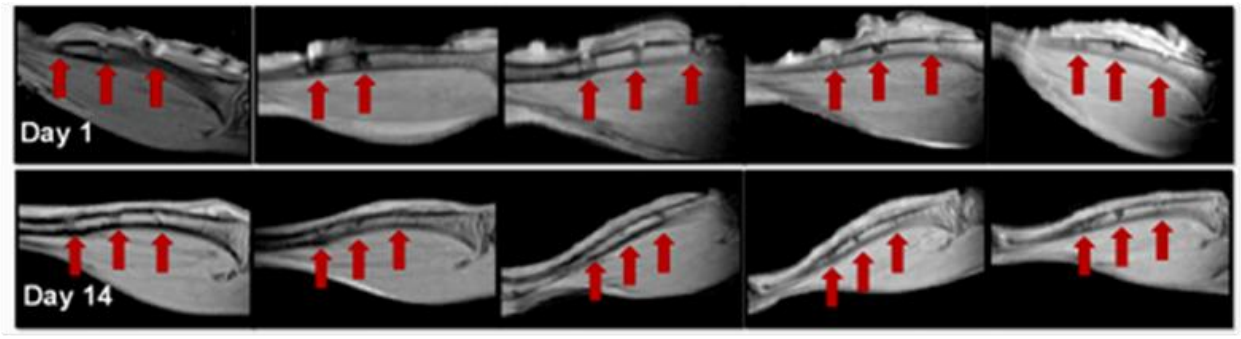

Figure 3-1 Example MRIs at day 1 and day 14 post surgery. At day 1, the images show bone holes and soft tissue damage. At day 14, images show the healing progress in bone and soft tissue.

μCT findings -- Bone was clearly visible with μCT. In both 2D and 3D images, calcified regions, including bone tissue and HA implants, appeared as radiopaque areas. All bone injuries in all study groups were clearly detected on day 1 and day 14. Similar to MRI, μCT imaging verified that the cortical bone opposite to the side of the fracture was not breached. At day 1, μCT showed gaps in the cortical bone at the fracture sites and the HA implant was clearly detected in the middle fracture site (Figure 3-2 B & C). At day 14, the 2D μCT image showed bridging of the cortical bone at the three holes, but each hole showed different amounts and patterns of trabecular bone in the medullary space. Control holes showed a few bony spicules. The middle holes showed newly formed bone around the HA implant. Profound trabecular bone

formation was shown in the distal hole (Figure 3-2 F). The 3D µCT was thresholded to the bone only and it showed continuity of the bone surface by day 14 (Figure 3-2 E).

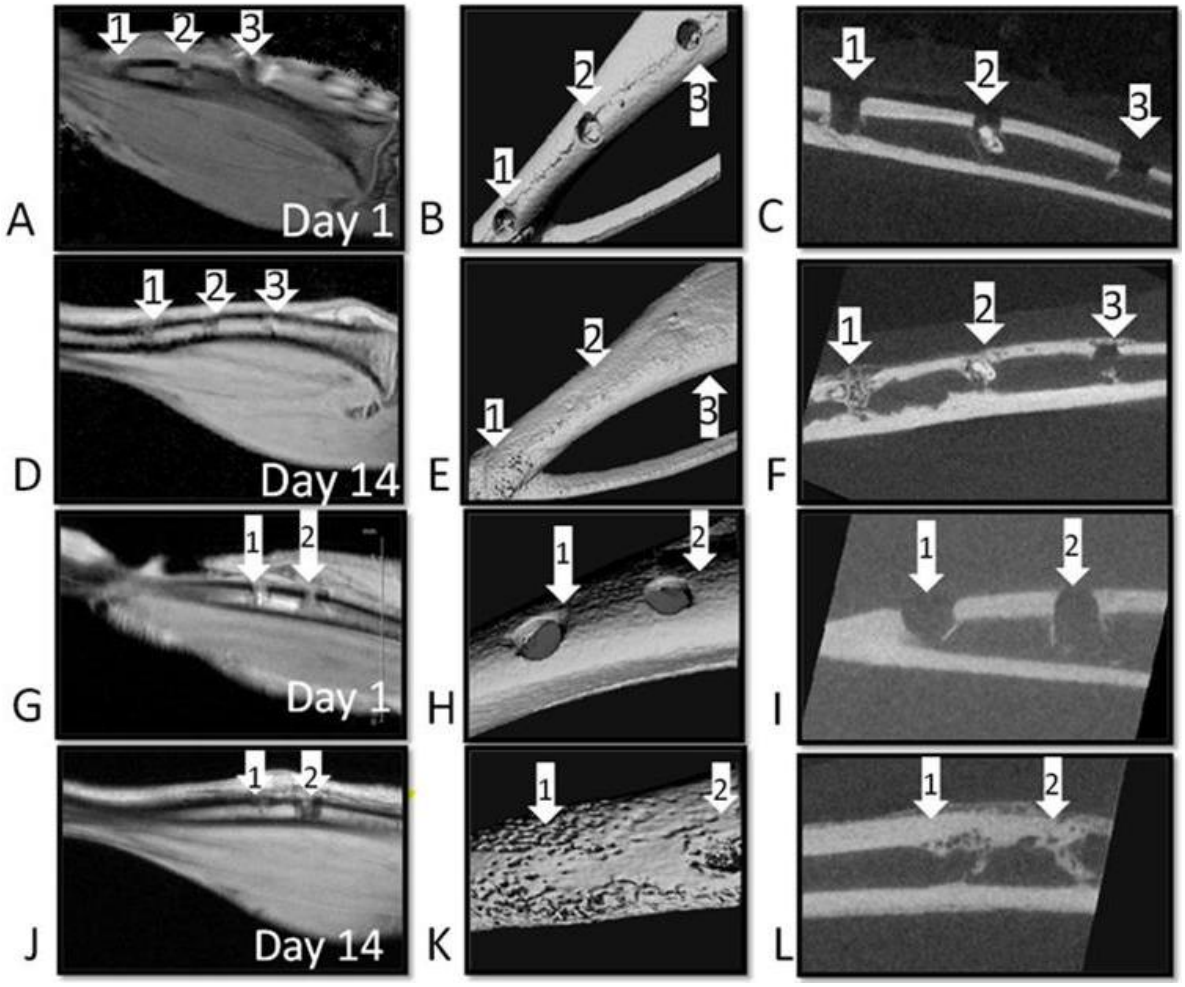

Figure 3-2 (A-F): Mouse tibia images from group 1. (A & D) MRI, (B&E) 3D µCT, and (C & F) 2D µCT, on day 1 (upper row) and day 14 (second row). Three bone injuries are visible on day 1 and day 14. The fractures have been treated with: 1-matrigel, 2-HA and 3-non-treated control. The fractures treated with the biomaterials (holes 1 & 2) showed a different healing pattern than the control fracture (hole 3). The lower MRI signal in the marrow of hole 1 (D) corresponds to a hole with significant "trabecular type" growth as seen in the µCT (F). In all the subjects, when major differences in healing were observed

with µCT, differences could also be seen in MRI. In MRI, it often occurred that not all 3 holes were visible in one image plane. For this reason, not all holes are visible in (A). We chose this example due to the excellent alignment in (D), showing the different signal intensities associated with the different holes. (G-L): images from group 3 (two fracture: hole 1 received no treatment, hole 2 received purecol loaded with ES cells). (G & J) MRI, (H& K) 3D µCT, and (I & L) 2D µCT. Upper panel shows the bone at day 1 and the lower panel shows the same bone at day 14. At day 1 (G) the MR image showed high signal intensity at the site of fracture. By day 14 ossification of the callus was observed by µCT and MRI in the control fracture (hole 1) while the treated fracture (hole 2) showed limited healing. This MR image (J) clearly shows the difference in signal in the marrow, and the restoration of the black line associated with cortical bone in a drill hole that is healing (hole 1) versus one that is not healing well (hole 2).

MRI and µCT common findings –At day 14, a thin layer of bone bridging the cortical defect was detected in the fractures using both imaging modalities. Fractures treated with biomaterial implants had trabecular-like bone in their marrow spaces (Figure 3-2 D, F, J & L).

Both imaging modalities detected callus ossification at the defect site in a mouse from group two (Figure 3-3 E & F). Also, the direction of the newly formed bone shown in the µCT corresponded to the intermediate intensity apparent in the MR images (Figure 3-3 A & B). In 2D µCT, the HA appeared more radiopaque than the trabecular-like bone in the distal fracture (Figure 3-3 D), while in MRI it appeared more hypointense than the trabecular-like bone in the distal fracture (Figure 3-3 C), which might be due to the condensed and highly calcified structure of the HA particles.

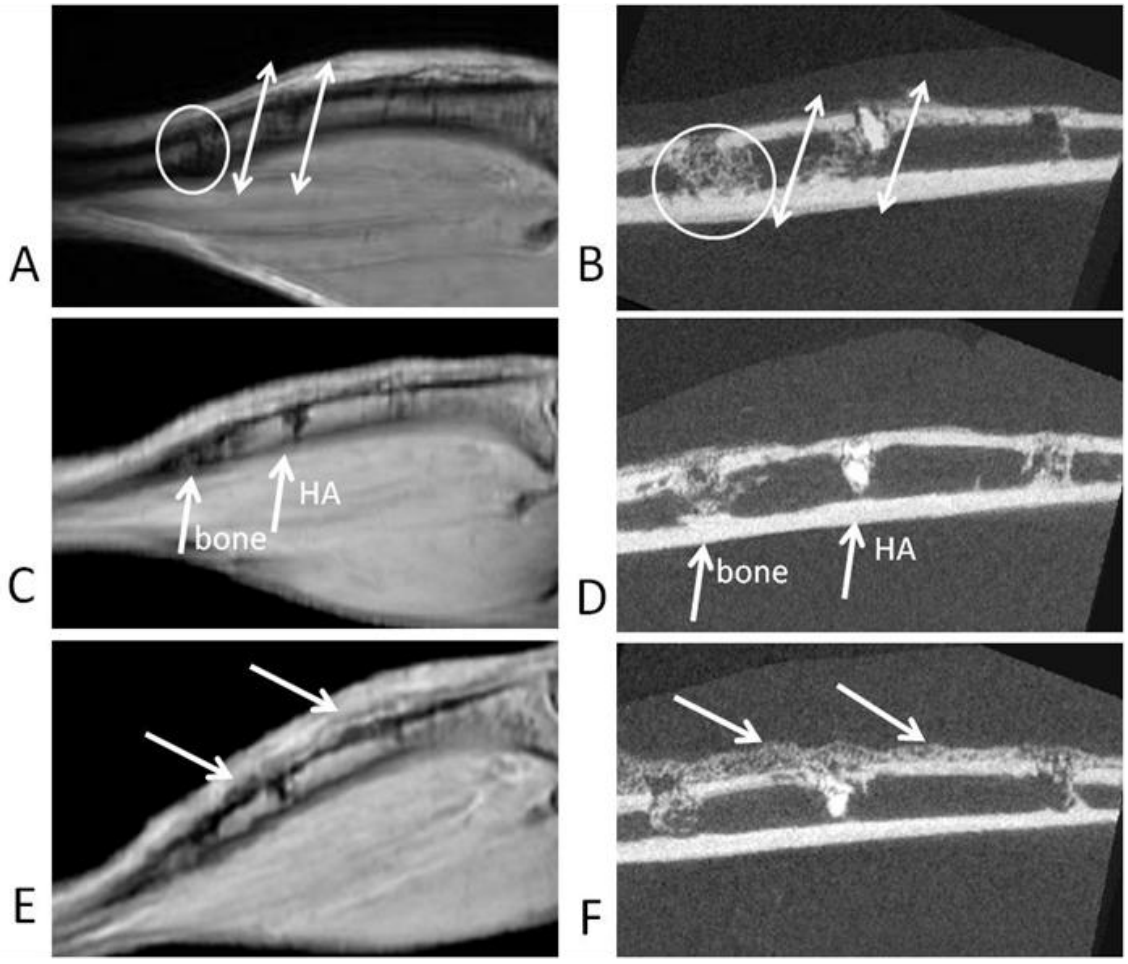

Figure 3-3 (A, C & E) are MRI and (B, D and F) are 2D µCT of three example mice at day 14. All images show visualization of bone healing and biomaterials. (A & B) the direction of the newly formed bone shown in the 2D µCT corresponds to the intermediate MRI signal intensity data. (C & D) MRI and 2D µCT of a mouse from group 2. The MRI (C) shows intermediate intensity areas where there is bone and a hypointense area where there is hydroxyapatite. (E & F) Visualization of callus ossification. In one mouse from group 2 a more dramatic ossification of the callus at the fracture site (the arrows point to the ossification) was observed using both MRI and µCT imaging modalities. The MRI (E) shows the ossification as a medium intensity region of mottled appearance that exists above the cortical bone and below the skin (arrows).

Histology findings – At day 1, fractures were identified as gaps on one side of the cortical bone with disruption in the bone marrow tissue, in histology. This mirrors what we saw in MR and μCT images. In all fractures, the presence of a soft tissue reaction, composed of a mixture of hematoma, granulation tissue and the implant material, was visualized (Figure 3-4 A). In the non-treated control fractures, hematoma was predominant (Figure 3-4 D). In contrast, in the middle fracture (treated with HA), a cavity was detected at the site of the implant where the HA had been dislodged during sectioning, and the defect was surrounded with mostly granulation tissue (Figure 3-4 C). Where the distal hole was treated with purecol (group 2), the hole was filled largely with a hematoma (Figure 3-4 B). Where the distal hole was treated with matrigel (group 1), the gel implant appeared as a white lump (histology not shown).

At day 14, in groups 1 and 2, the control holes had the least amount of trabecular bone in their medullary spaces compared to the treated holes, while in group 3 there was apparent trabecular bone in the control hole. This suggests that the model can be variable in its recovery time-course. Factors potentially affecting the recovery time-course in this study include the biomaterial used and the number of holes drilled. Histology validated the MRI and μCT findings by demonstrating the fracture at day 1 and the remodeling callus at day 14.

In the middle hole, by 14 days, the HA implant was integrated in the newly formed bone. It can be seen as a dark spot on MRI (Figure 3-2 D, Figure 3-3 A, C & E: middle hole). A greater amount of trabecular bone was detected in the medullary space of the distal hole (with matrigel and purecol gel, depending on the group) than was detected in the medullary space of other holes.

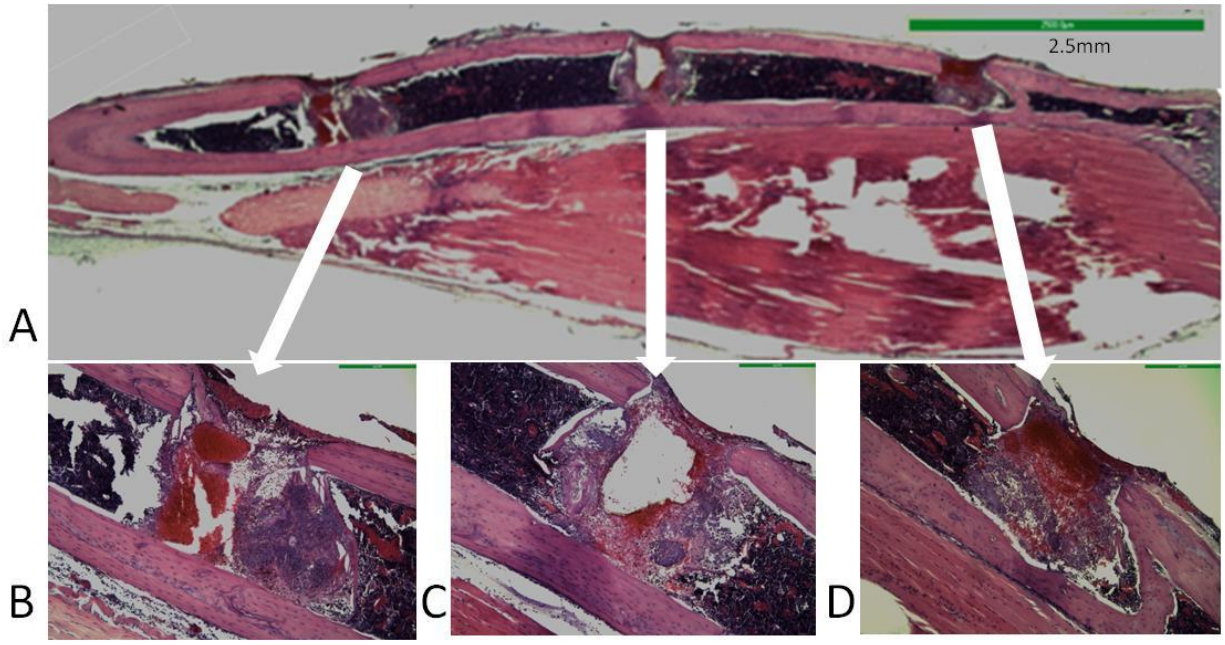

Figure 3-4 H & E stained section of a mouse from group 2 (purecol) after day 1 (A). Three fractures are clearly visible, showing a soft tissue reaction composed of a mixture of haematoma and granulation tissue. (B, C & D) Higher power images of each fracture shown in (A). (B) Fracture treated with purecol. (C) Fracture treated with HA, and (D) control fracture (non-treated). Scale bar at B, C and D is 250 µm.

In group three (two holes: control; dESCs in a gel construct) day 1, areas in the control hole where edema appeared as hyperintense regions in MRI (Figure 3-2 G), was reflected in histological sections by the presence of haematoma and granulation tissue at the site of fracture (Figure 3-5 A). In the treatment hole at day 1, a cortical gap was detected filled with the implanted dESCs construct in the medullary space (Figure 3-5 B). At day 14, the control hole showed a stage of trabecular bone remodeling (Figure 3-5 C). A different healing pattern was observed at the treatment hole, where the dESC 3D collagen construct appeared as a bone-like tissue in the medullary space of the treated hole (Figure 3-5 D).

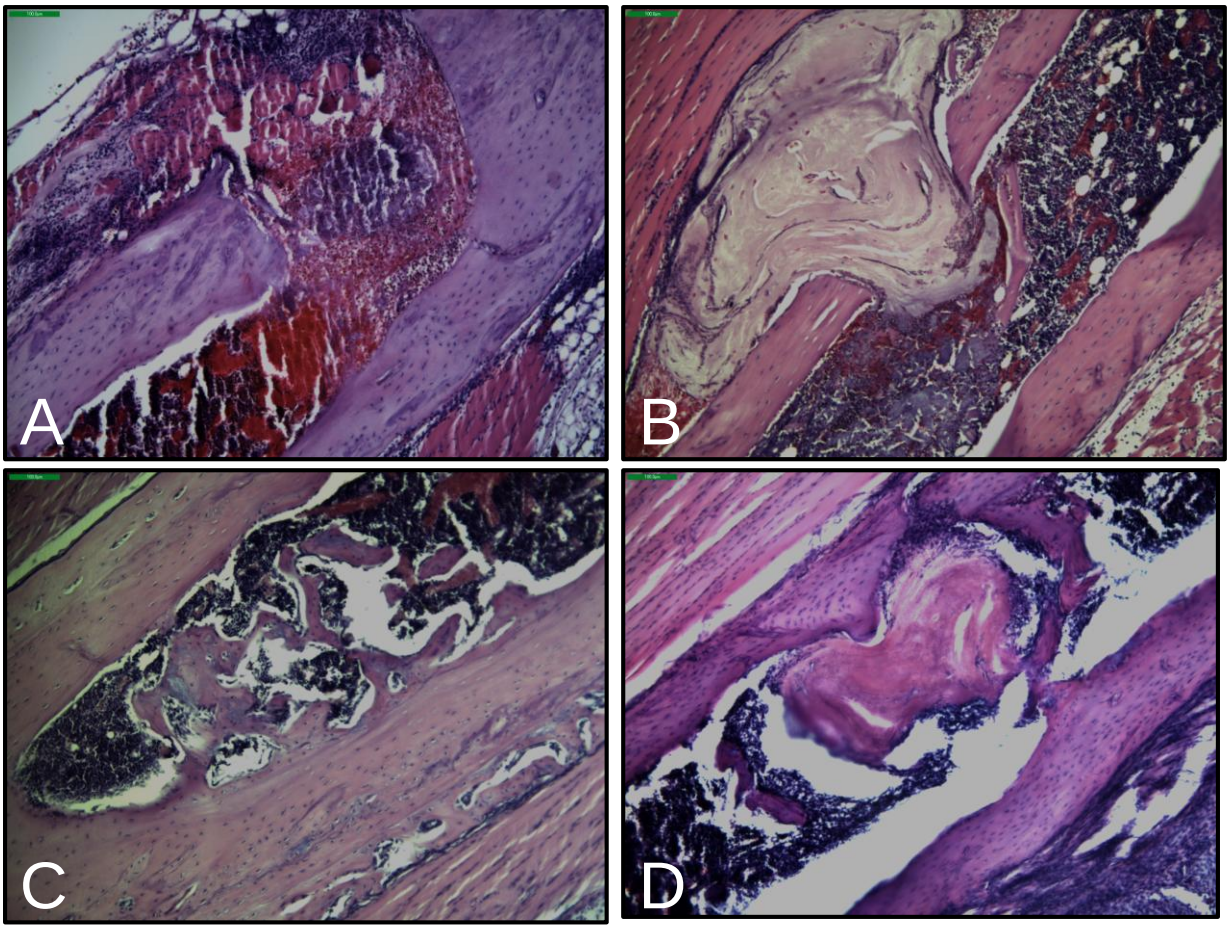

Figure 3-5 H & E stained sections of a mouse from group 3 (ESCs) at day 1 and 13. (A & B) Two fractures of the same mouse at day 1 post surgery. (A) Control fracture with no treatments. A gap in the cortical bone appears filled with infiltration of cells indicating inflammation. (B) Treatment fracture filled with dESCs in a 3D collagen construct. (C & D) Images of a mouse from the same group at day 13 post surgery. (C) Control fracture shows trabecular bone at the medullary space indicating a stage of bone remodelling. (D) Treatment fracture with bone-like tissue at the medullary space. Scale bar 100 µm.

3.4 Discussion

MRI offered additional information about soft tissue and biomaterial properties during fracture healing over µCT. MR images also corresponded to histological findings. Thus, MRI could be a useful tool in fracture healing assessment, especially in cases where assessment of the gross morphology is all that is necessary (i.e., clinical imaging of skeletal injuries in larger bones).

Evidence from the grey-scale images indicates that MRI, using the RARE sequence, and µCT showed similar data about the bone response at several stages of healing in response to bur-hole fracture. µCT has been the most common imaging modality for examining bone morphology and micro-architecture in animal models. In the current study, µCT provided higher contrast and resolution of the bones than MRI. However, µCT imaging has some drawbacks, such as exposing the subject to radiation. For repeated measures studies, as for repeated clinical scans, radiation exposure might be hazardous or could induce secondary effects that decrease the efficacy of a therapy[95] (i.e., cell-based implants may be affected by multiple radiation exposures). µCT also has less contrast than MRI when studying soft tissues such as the medullary space, bone marrow tissue, transplanted biomaterials and skeletal muscles. The sensitivity of MRI to soft tissues allowed for the detection of edema at day 1 at the site of fracture[103].

Recent technological developments, including the increasing availability of relatively low-cost MRI scanners, may further expand the application of MRI for detection of bone injuries. The awareness of these findings is very important, since early diagnosis leads to early recovery. Therefore, MRI could be more widely used in the assessment of patients with bone injuries,

especially when serial imaging is needed to avoid unnecessary radiation exposure, or when tissue engineered-based therapies are involved[104].

Different biomaterials appear to stimulate different patterns of healing. The loaded holes had more trabecular-like bone tissue than the control holes, in their medullary spaces, at day 14. This suggests a pre-remodeling stage in the loaded holes and a more advanced stage of healing in the control holes[86]. The ability to non-invasively monitor these biomaterials and their effect on bone healing *in vivo* is of great importance; since they are widely used in tissue engineered based therapies[105] and they have the potential to be applied in human in the future. Stem cells have a potential role in repair of bone[105]. We used ESCs with purecol to induce osteoblasts cell fate[30,44]. Matrigel and purecol are commonly used as carriers for stem cells[33]. HA became part of the newly formed bony structure suggesting that it can fill the bone defects and contributed to bone formation[8,106]. Overall, various biomaterials have shown to improve fracture healing, however further investigations are required to optimize these approaches[6,7,97,98] .

To diagnose the stage of healing based on non-invasive imaging tools such as MRI and µCT, it is important to correlate the stages of healing in histomorphological findings with the observations obtained from imaging[107]. We correlated the signal intensities obtained from MRI with the type of tissue observed in histological sections. At day1, the moderate hypointensity areas, seen at the medullary space at the sites of injuries, were probably due to interrupted blood flow and damaged bone marrow tissue. This was correlated to histology by disruption of normal bone marrow tissue and invasion of the site of fracture with various cell types, suggesting an inflammatory reaction and the formation of a clot[86]. Later, this clot will be invaded by osteogenic repair tissue. The medullary space in the middle hole, contained HA, appeared as darker hypointensity signal than the proximal and distal ones, this might be due to the absence of fluid

content and the high calcification level of the HA particles. Additionally, the interruption of the hypointense line, that represents the cortical bone, was correlated to the gap in cortical bone at the sites of fracture in histology. Finally, the soft tissue surrounding the fracture site showed hyperintensity signal which indicates the presence of high fluid content, suggesting edema or hematoma[108]. Though, histology couldn't show the soft tissue surrounding the fracture because it was lost during processing. At day 14, the hypointensity signals in MRI at the medullary space and cortical bone were correlated to the presence of trabecular-like bone in histology. These findings suggest partial healing. In brief, tissues with high calcification appear as hypointensities in RARE images, such as; bone and HA[107]. Conversely, tissues with low calcification and higher fluid content appear as hyperintensities, for example, bone marrow, hematoma and edema.

In conclusion, we used high spatial resolution MRI and μCT scanners to obtain images. This was done to determine if MRI could detect the bur-holes and recovery in the holes. We found that MRI can be used as an alternative to μCT to examine the role of various biomaterials in fracture healing, especially when ionizing radiation is contraindicated or when soft tissue and edema are end points. We also found that MRI was capable of detecting signal intensity changes associated with the different biomaterials.

These findings indicate that MRI is a useful tool in imaging bone fracture repair and biomaterials used for bone regeneration. This opens the way for using MRI to track cells in bone fracture.

Chapter Four: **MRI of bone-targeted nanoparticles for potential use as carriers of therapeutic or diagnostic materials to the bone fracture site**

The aim of this chapter is to test new bone-targeted nanoparticles that were developed by our collaborators in Dr. Uludag's lab as part of a collaborative research project. Our contribution was testing the nanoparticles' efficiency in encapsulating and retaining gadolinium contrast agent. If the nanoparticles successfully retained Gd, they could be used as a T_1 bone-targeted contrast agent to improve the contrast in MR bone imaging.

4.1 Introduction

Normally bone has the capacity to heal itself after a fracture[15], however in some diseases such as osteoporosis, it loses its healing capacity[109]. Tissue-engineered therapies can help in the bone healing process[30]. However, it could be difficult to deliver therapeutic materials in a controlled manner to the bone fracture without a bone-targeted drug delivery system. Bone-targeted drug delivery systems used to encapsulate therapeutic agents could be potentially used to encapsulate diagnostic agents as well. Many studies have reported using nanoparticles (NP) made of liposomes as carriers for MRI contrast agents[110,111] but only few of them investigated the use of bone-targeted ones to carry MRI contrast agents specifically to the bone[112], which could be used to diagnose and monitor bone injuries, while avoiding the unnecessary systemic adverse effect and improve the quality of bone imaging using MR.

Many research groups are currently developing new bone-targeted delivery systems to produce one that is biocompatible, non-toxic and has control over the release of the material they carry whether therapies or contrast agents[9]. Recently, a bisphosphonated ligand (BP) was conjugated to NP to add bone- targeting potential to them[112]. The bisphosphonated ligand binds to the hydroxyapatite crystals in bone[112]. This will reduce the non-specific delivery and the

undesirable systemic side effects associated with therapeutic materials or contrast agents. For example, lipid nanoparticles were previously used to encapsulate Gd particles and decrease their toxic effects on the tissues[110].

Uludag's group developed a new bone-targeted NP with a BP ligand[9]. The mentioned NP successfully retained the drugs in a bioactive form and released it at the site of bone fracture, which indicates that the new NP can deliver drugs to the bone[9,113]. Because these particles proved to be biocompatible and non-toxic[9], this opened up the possibility for testing them as carriers for MRI contrast agents because encapsulating contrast agents reduce their toxic effects[111]. Previous studies have investigated the use of bone-targeted NP in carrying MRI contrast agents; however the maximum relaxivity obtained with these Gd-NPs was 22.1 $mM^{-1}s^{-1}$ [114-116]. Current research aims at synthesising new Gd-NPs that have higher relaxivity values, which translates to lower doses of contrast agents required for MRI visualization. This study is an attempt to produce a bone targeted, non-toxic, biocompatible and efficient T_1 contrast agent.

As part of our project, developing *in vivo* tracking system of therapeutic agents in bone fracture models, we were interested in the newly developed particles for our system. The NP loaded with Gd was developed in our collaborators lab (Uludag's lab at U of A). Our contribution was to use MRI to test whether the BP-NP can efficiently incorporate the Gd particles, and whether the encapsulation affected the MR relaxivity of the Gd. We described a method to assess the encapsulation process of the new NP using MRI. Similar methods has been previously use by Sandiford group to assess the effectiveness of a newly developed BP-SPIO as an MRI contrast agent[79,80,117]. A relatively similar concept was used in this chapter to test the encapsulation efficiency of non-bisphosphonated NP (NP1) and compare it to the encapsulation efficiency of bisphosphonated NP (NP2) to know whether the BP ligand affect the encapsulation

process or not. Additionally, we tested the effect of encapsulation on the relaxivity of Gd to know whether the liposome coating affected the overall relaxivity of Gd or not.

4.2 Materials and Methods

Calculating the encapsulation efficiency of Gd-NP takes several steps which are summarized in this paragraph to explain the logical flow. The steps are explained more fully below to explain the technical procedures. Briefly, to calculate the encapsulation efficiency of the NP, we did an MRI relaxivity measurement. The T_1 values obtained from the relaxivity measurement were used to calculate the final concentrations of Gd in the newly developed NP. Then, the final concentrations were used to calculate the encapsulation efficiency of Gd-NP1and compare it to that of Gd-NP2, to know whether the BP ligand affect the encapsulation process or not. Also, we compared the relaxivity values of the Gd-NP before and after dissolving their liposome coat, to know whether the encapsulation affects the relaxivity or not.

T_1 is the longitudinal relaxation rate (explained in Section 2.1.3).

r_1 is the change in relaxation rate per molar concentration. It is obtained from the slope of the curve of R_1 ($1/T_1$) plotted against the molar concentration.

Preparation of Gd-loaded nanoparticles. The NP were developed at Uludag's lab at U of A, and then shipped to us. They were composed of liposomes and were prepared in two different formulations. Both formulations had distearoylphosphotidylcholine (DSPC) and cholesterol (CH). The first formulation, NP1 had distearoylphosphoethanolamine-polyethylene glycol (DSPE-PEG) while the second formulation NP2 had DSPE-PEG-bisphosphonate (DSPE-PEG-BP). The molar ratio for these compounds was 2:1:0.1 for DSPC/CH/DSPE-PEG and DSPC/CH/DSPE-PEG-BP. Two additional formulations were prepared similar to NP1 and NP2 but with Gd encapsulated into them. The gadodiamde (Gd, Omniscan) was added during the

preparation and entrapped into the core of the liposomes. Then, the unencapsulated Gd was removed. This gave us Gd-NP1 and Gd-NP2[9]. That is to say the NP1 formulas does not have BP group while the NP2 formula has a BP group.

Phantom preparation. The compounds tested were NP1, NP2, Gd-NP1, Gd-NP2, and Gd. The Gd-NP1 and Gd-NP2 were imaged before and after lysing of the liposome coat with 20 % sodium dodecyl sulfate (SDS) to compare the effect of encapsulation on the relaxivity of Gd. This means we had 7 compounds to test in phantoms.

Six different dilutions of each of the compounds in Table 4-1 were used. Thus, a total of 42 phantom tubes were prepared. The dilutions tested were 0, 1.25, 2.5, 5, 10, and 20 µM. All the compounds were put in glass tubes and arranged in 7 groups for MR imaging and the tubes were inserted into a container containing agar type I [10 g/L] to minimize the image artefacts caused by air.

Table 4-1 Formulations used for MR relaxivity measurement of the newly developed NPs.

Formulations	Composition
NP1	DSPC/CH/DSPE-PEG
NP2	DSPC/CH/DSPE-PEG-BP
Gd-NP1	DSPC/CH/DSPE-PEG with Gd (pre and post lysing)
Gd-NP2	DSPC/CH/DSPE-PEG-BP with Gd (pre and post lysing)
Free Gd	Gd omniscan [concentration 50 mM]

MR phantom imaging to determine T_1 and r_1. In order to determine the r_1 of each formulation, we estimated the T_1 relaxation time of each of them using an inversion recovery True-FISP sequence which has been frequently used for T_1 quantification[79,80]. In this sequence balanced opposite gradients are used to correct phase discrepancies. An inversion pulse 180 º is applied to flip the magnetization into the negative z-axis. A T_1 map was created by using

different inversion times, with each followed by a FISP scan segment (Figure 4-1). A series of 60 inversions ranging from 305-5969 ms, TR/TE= 3/1.5 ms, flip angle = 15º, scan repetition time= 30,000 ms, acquisition time = 4 min, in our standard 9.4 T Bruker magnet. The temperatures of the phantoms were maintained at 37º. After acquiring the data, we processed them to generate a T_1 map. The values of T_1 relaxation time were obtained by using the following formula[118].

$$S(TI) = S_0(1 - 2e^{-\frac{TI}{T1}})$$

where S(TI) is the signal measured at time TI (inversion time), and S_0 is the signal at steady state equilibrium of the longitudinal magnetization. After that, we calculated the relaxation rates R_1 in which $R_1=1/T_1$. Then, using Sigma Plot software, the relaxivity (r_1) was calculated. r_1 is the slope of the line resulted from plotting R_1 versus concentration. The r_1 value was obtained by using the regression wizard equation $y=y_0+rx$, where r is the slope of the line, and is equal to the relaxivity (r_1).

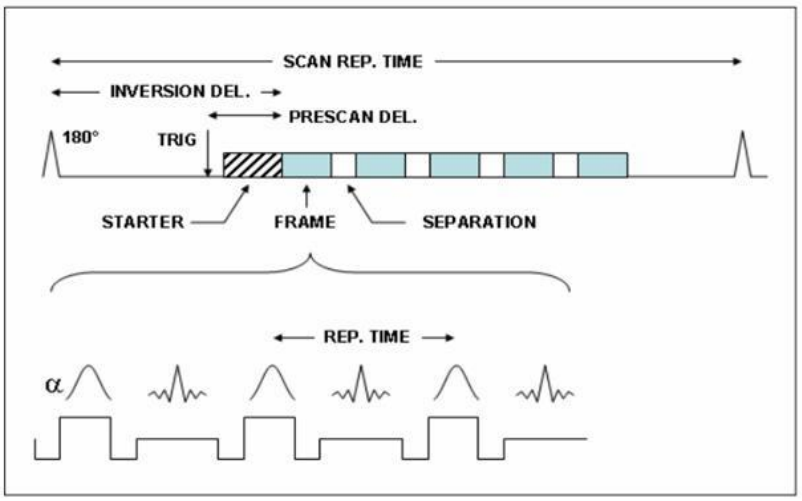

Figure 4-1 A diagram illustrating the Inversion recovery True FISP sequence (reproduced from Paravision user manual)[119].

Calculation of the final concentrations of Gd to determine the encapsulation efficiency.

In order to determine the encapsulation efficiency of the Gd-NP1 and Gd-NP2, first we calculated the final concentration of Gd in Gd-NP1 and Gd-NP2. Second, we compared the final concentration to the assumed concentration to find the encapsulation efficiency.

First, the final concentrations of Gd in the Gd-NP1 and Gd-NP2 were calculated using the following equations, respectively

$$final\ Gd-NP1\ concentration = \frac{\frac{1}{T1(\mathrm{Gd-\ NP1})} - \frac{1}{T1(\mathrm{NP1})}}{r1}$$

$$final\ non\ Gd-NP2\ concentration = \frac{\frac{1}{T1(\mathrm{Gd\ -NP2})} - \frac{1}{T1(\mathrm{NP2})}}{r1}$$

Where r_1 is the relaxivity of free Gd. T_1 is the relaxation time of each of the dilutions of the compounds used in the phantoms. Since Gd-NP1 had 6 dilutions, we used the previous equation to calculate the Gd concentration in each dilution, and then we multiplied the resulted concentrations by their corresponding dilution factors. The resulted concentrations were averaged to obtain the final concentration of Gd in Gd-NP1. The same procedure was repeated to obtain the final concentration of Gd in Gd-NP2.

The second step was to calculate the encapsulation efficiency for each formulation using

$$encapsulation\ efficiency = \frac{final\ concentration}{Assumed\ concentration} \times 100\%$$

The final concentrations are the ones calculated in the first equation. The assumed concentration is the hypothetical concentration assumed at the time of preparation. It is calculated based on that the concentration of DSPC in the liposomal suspension was 20 mM. The Gd solution used for encapsulation was 0.1 M, and the encapsulation efficiency was assumed to be around 20-30%, which means that the assumed concentration of Gd is 20-30 mM.

4.3 Results

The inversion recovery True FISP sequences was used to generate a T_1 map for each formulation, an example of a T_1 images used to generate the map is shown in Figure 4-2. It shows the images with different T_1 weighting. The phantom set up with agarose surrounding the phantom tubes was good at minimizing the artefacts around the phantom tubes, however at the first image some banding artefacts were noticed but they disappeared soon after the second inversion. Image artefacts did not affect the data analysis or results. The relaxivity measurements were successfully completed by plotting R_1 ($1/T_1$) against the different concentrations of each formulation to obtain the r_1 value. The r_1 and T_1 obtained were used to calculate the encapsulation efficiency.

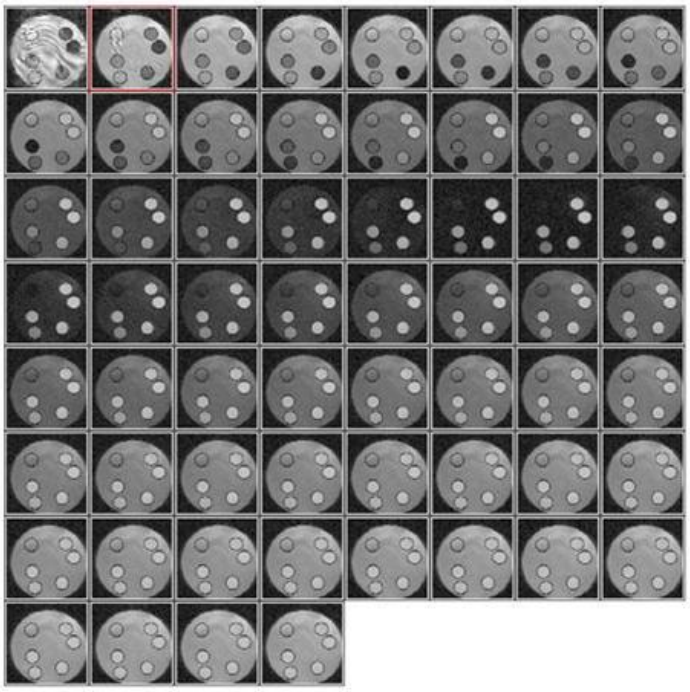

Figure 4-2 Inversion recovery True-FISP T_1 images of Gd-NP2 phantoms, showing 6 tubes, at concentrations from 0-5 mM.

The NP1 had a r_1 of 0.13 $mM^{-1}sec^{-1}$ which is close to zero (Figure 4-3 A). Their r_1 increased after they were loaded with Gd to 183.9±17.9 $mM^{-1}sec^{-1}$. The r_1 increased again after dissolving their liposome coat with SDS to 212.8±9.5 $mM^{-1}sec^{-1}$(Figure 4-4 A & B), demonstrating that the unbound Gd had higher relaxivity than encapsulated Gd. A similar trend was seen in the NP2, although the r_1s were consistently lower, they had r_1 0.9±0.3 $mM^{-1}sec^{-1}$ (Figure 4-3 B). Their r_1 increased after they were loaded with Gd to 40.2±1.05 $mM^{-1}sec^{-1}$. The r_1 increased again after dissolving their liposome coat with SDS to 148±9.5$mM^{-1}sec^{-1}$(Figure 4-4 C & D), confirming that the encapsulation of the Gd decreased its relaxivity. Relaxivity values are summarized in Table 4-2.

Table 4-2 Relaxivity values of the compounds tested represented in $mM^{-1}s^{-1}$ with standard errors.

Compound	r_1 before lysing the liposome coat	r_1 after lysing the liposome coat
NP1	0.13±0.4	NA
Gd-NP1	183.9±17.9	212.8±9.5
NP2	0.9±0.3	NA
Gd-NP2	40.2±1.05	148±9.5

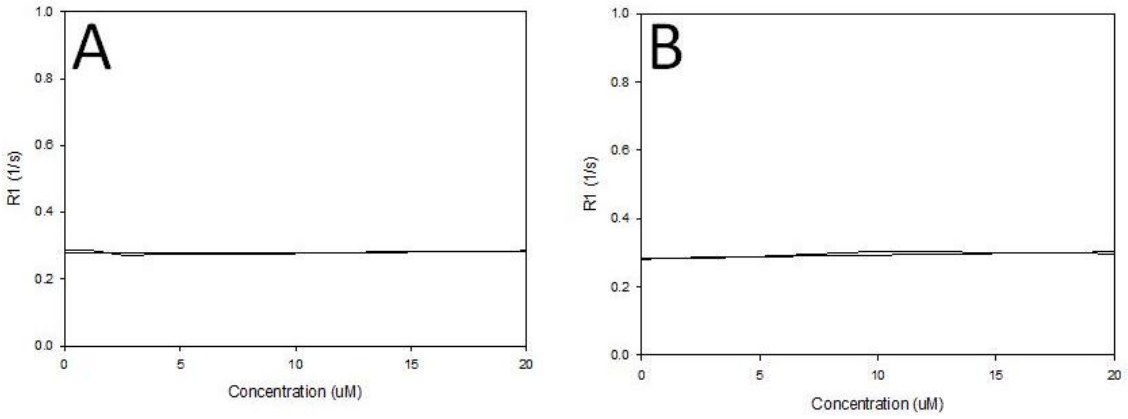

Figure 4-3 Relaxivity graphs of the (A) NP1 and (B) NP2. The line has a negligible slope, which translates to a very small relaxivity.

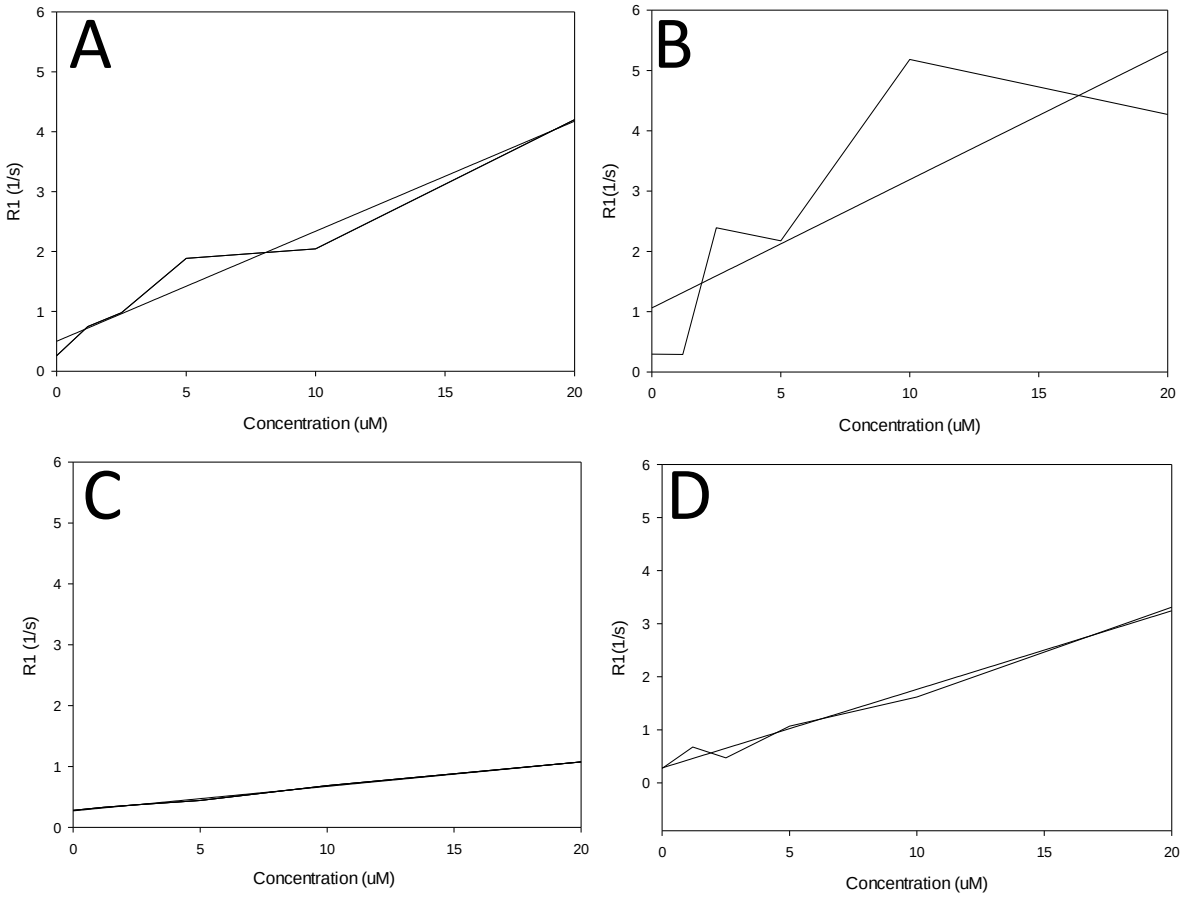

Figure 4-4 Relaxivity graphs showing the increase in the relaxivity of the Gd-NP1 and Gd-NP2 before and after lysing their liposome coat. A & C are Gd-NP1 and GD-NP2 before lysing of their liposome coat, respectively. B & D are Gd-NP1 and Gd-NP2 after lysing of their liposome coat.

Based on our calculations the final concentration of Gd in the Gd-NP1 was 36.8 mM and the final concentration of Gd in the Gd-NP2 was 6.37 mM. Since, the assumed concentration of Gd was 20-30 mM; therefore the encapsulation efficiency for the Gd-NP1 was 147% while for Gd-NP2 it was 25%. This means that the non BP formula (NP1) had higher Gd concentration and encapsulation efficiency than the BP formula (NP2). This might be due to the chemical

complexity of the interaction between the BP group and the Gd which decreased the ability of the BP-liposome to entrap it.

4.4 Discussion

In an effort to contribute to the development of a new bone targeted nanoparticles that can carry Gd contrast agent, we used MRI to assess their encapsulation efficiency. We used MR inversion recovery sequence was used to create a T_1 map where T_1 and r_1 values were obtained and used to calculate the Gd encapsulation efficiency (the ability of the nanoparticles liposomes to encapsulate Gd, explained in Section 4.2) in Gd-NP1 and Gd-NP2. Gd-NP1 had higher encapsulation efficiency and was able to incorporate more Gd than Gd-NP2. These findings are important in the evaluation of the new NP capabilities in carrying MR contrast agents to the bone.

The MRI protocol used in this study was inversion recovery true FISP with variable inversion times which is considered one of the desirable sequences for quantifying T_1[79,80]. It generated a T_1 map with high S/N ratio, minimal artefacts, and in a short acquisition time. The banding artefacts noticed at the first image were cause by magnetic field inhomogeneities which were minimal in this scan due to the good shimming applied.

Gd contrast agents are known to have a T_1 shortening effect which leads to increases in the signal intensity in a T_1 weighted MR image[120]. Additionally, they also have a T_2 shortening effect which decreases the signal intensity in an MR image[120]. Both, T_1 and T_2 shortening effects compete together and usually the T_1 effect dominates leading to an increase in the signal intensity[120, 121]. Yu *et al.*, found that at low concentrations of Gd compounds the T_1 effect dominated and the signal intensity increased[121]. This is in concurrent with our finding in which

we found signal intensity increase and a T_1 shortening effect when we used Gd at concentrations from [0-40µM].

The encapsulation efficiency results showed that, the Gd-NP2 encapsulation efficiency was only 25%, which means it did not meet the assumed encapsulation efficiency. On the other hand, the Gd-NP1 encapsulation efficiency was 147%, which means it exceeded the assumed encapsulation efficiency. The only difference between the two formulas was the bisphosphonated ligand which could be the reason behind complicating encapsulation process[115], making the NP1 more capable of encapsulating Gd particles than the NP2. A similar finding was demonstrated in study where the bisphosphonated group decrease the stability of a bisphosphonated Gd compound[115].

Our work demonstrates that, despite the low encapsulation efficiency presented by the Gd-NP2 (25%), they had a high relaxivity value (40.2±1.05 $mM^{-1}sec^{-1}$), which exceeded the relaxivity of the clinically available Gd contrast agents (22.1 $mM^{-1}s^{-1}$)[114]. Since, the results of the relaxivity measurements demonstrated that the relaxivity of the outer liposomes had a negligible value, this means that they did not contribute to the high relaxivity value of the Gd-NP2. However, the high relaxivity of the Gd-NP2 could be due to the altered design of the external liposome coating which allows more interaction between the Gd and the surrounding water, subsequently, more reduction in T_1 relaxation time. Changing the relaxivity value of contrast agents by altering their polymeric coat properties was previously reported by Ladd[122].

The development of these bone targeted particles will help improve MRI bone imaging. Since bone does not produce signal[78] and since positive contrast agents increase the signal and appear bright in MRI[115,123], therefore using positive contrast agents to image bone can reduce the lack of signal problem and improve the imaging outcome. Several attempts have been made to

develop bone targeted positive contrast agent that have enough relaxivity, safety, and stability for *in vivo* detectability. Yet, none has proven to fulfil all these criteria to be used *in vivo*. Continuous efforts are made to develop one that is stable, safe and have enough relaxivity to allow its detectability *in vivo*[114,116]. Given that the newly developed bone targeted contrast agent have relaxivity that exceeds the clinically available ones[116], this indicates that the new agent will have sufficient relaxivity as a T_1 contrast agent for *in vivo* MR imaging.

Despite that the newly developed bone targeted Gd-NP2 did not meet the expected encapsulation efficiency; yet they proved to have a relaxivity that exceeded the previously used ones MR T_1 contrast agent[114]. Given that their relaxivity exceeded that of the already available Gd-NP[116], they can be used at lower doses to achieve the same T_1 shortening effect in *in vivo* MR imaging. These findings are important because increasing the relaxivity of a contrast agent will improve its detectability in MRI. Further exploration is needed to test those particles *in vivo* and measure their relaxivity and capability of targeting bone.

Overall, the bone targeting capability of these particles will increase the specificity of their delivery to the bone, and thus reduce the unnecessary side effects on other tissues. Besides, the brightening effect of the of the Gd contrast agent will aid in overcoming the lack of signal problem of bone, plus it will enhance the contrast between the targeted tissue and the surrounding tissues. Thus, the new bone targeted NPs could potentially improve the visualization of bone in MRI. The particles could be potentially used in diagnosing bone pathologies and treatment follow up.

Chapter Five: **Studying the properties of the MRI contrast agents used in this project and measuring their relaxivities**

In this chapter we assessed the properties of three negative and one positive contrast agent. We quantified their relaxivity using in vitro MR imaging. The information obtained from this chapter will guide us in the process of cell labelling using these contrast agents in chapter 6.

5.1 Introduction

Contrast agents are used to increase the contrast between tissues, by changing the relaxation time[73]. MRI contrast agents usually belong to one of three families: positive, negative and fluorinated contrast agents[111,124,125]. In this study we focused on the first two families; they are most commonly used in the field of cell tracking[10,69,123,126,127]. Quantifying the efficiency of MRI contrast agents allows us to assess whether they have sufficient relaxivity for MR visualization.

We used a relaxivity measurement method, also called relaxometry, to evaluate the efficiency of contrast agents[128]. The relaxivity value (r_1, r_2 and r_2*) reflects the ability of a contrast agent to change the relaxation rate ($1/T_1$, $1/T_2$ and $1/T_2$*) of water per concentration of contrast agent[54]. It varies according to the field of strength of the used magnet, the temperature and the parameters of the sequences used[48].

Negative contrast agents such as iron have much stronger paramagnetism than positive contrast agents (Gd), and they are usually called superparamagnetic for this reason[48]. They are surrounded by their own small magnetic field and thus when they are placed in the MR magnet they causes local disturbance in the main magnetic field at the site of the iron particles[48]. Their magnetic moment is about 4 orders of magnitude higher than paramagnetic contrast agent[125]. They have a predominant T_2 and T_2* shortening effect which causes loss of signal, and appear dark on T_2 and T_2* weighted MR images[69]. Iron oxide particles are usually composed of an iron

core and an outer coating such as dextran, to minimize the toxic effects caused by the contrast agent[129]. The advantage of using negative contrast agents is they have a strong effect on disturbing the magnetic field which produces a dark area in the image that is larger than the actual size of the contrast agent particles[125]. This phenomenon is called the blooming effect [125]and is useful in increasing the visibility of the contrast agent *in vivo*. The disadvantages of using negative contrast agents are that they interfere with visualizing the underlying anatomical structures and they do not represent the true size of the lesion or labelled cells. The latter is problematic when imaging is being used to assess lesion sizes. In this thesis we studied the characteristics of two negative contrast agents (Ferex and Bangs) and compared them to Feridex, one of the standard MRI iron-based contrast agents that was discontinued from production in 2008[130].

One of the iron based contrast agents that we studied had dual labelling properties. The Bangs particles are magnetic particles tagged with fluorophores, and they were manufactured specifically for cell labelling and tracking purposes. They can be detected *in vivo* by using the IVIS xenogen system which offers real time *in vivo* non-invasive imaging. This system could be of great benefit in longitudinal studies monitoring regenerative therapies. It can detect up to 50 cells *in vivo* for over 40 days. It utilizes the light emitted by the fluorescent particles and then analyzes its location and intensity[131]. The images obtained are in the form of calibrated photon emission. This means that the data displayed are a representation of the data and not the actual raw data. The obtained image is composed of a fluorescent image overlaid on a photographic image. We used it at this stage to test the Bangs fluorescent capabilities and the possibility of tracking the Bangs-labelled ESCs later in mice, in assistance to MRI cell tracking.

Positive contrast agents, such as the Gd are paramagnetic particles that have a predominant T_1 shortening effect, producing more signal and appearing as a bright area in T_1 weighted MR image. They are toxic in their free state so they have to be chelated to polymers such as albumin or dextran, to ensure their safety and stability *in vivo*[48,122]. They have less paramagnetism and smaller particle size than iron based contrast agents[48]. We studied Gado celltrack, a novel contrast agent that is manufactured specifically for cell tracking[132,133]. It has a much bigger size (50 nm) that conventional Gd contrast agents[134]. Gado celltrack has been investigated in *in vitro* studies to label human endothelial cells, smooth muscle cells and inflammatory cells[132-134]. To our knowledge our study is the first study to label ESCs using Gado celltrack and track them *in vitro* and *in vivo*.

In this study, we used the relaxivity measurement method to assess the MR capabilities of relatively new contrast agents (Ferex, Bangs and Gado celltrack) and compare them numerically with the previously used contrast agents in the field. Given that negative contrast agents affect the T_2 and T_2* relaxation times, and positive contrast agents affect the T_1 relaxation time, we used r_2 and r_2* relaxivity measurement to evaluate the efficiency of negative contrast agents[135], while for positive contrast agents we used r_1[123].

5.2 Materials and methods

Four contrast agents were studied (Bangs, Ferex, Feridex, and Gado celltrack). Different concentrations of the contrast agents were prepared in phantoms to measure their relaxivity. Method development included determining the concentrations of the contrast agents that would result in an appropriate amount of signal for T values to be obtained. It also, included determining how to make a phantom with no air bubbles or cracks in the agar because such cracks and air bubbles cause signal voids and imaging artefacts. The final phantom set up

consisted of NMR tubes filled with contrast agents at different concentrations, embedded into gelatin or agar to minimize artefacts. The imaging conditions such as imaging parameters and temperature were standardized to keep our relaxivity results consistent. The temperature of the phantoms was maintained at 37ºC during MR imaging.

Negative contrast agents. The characteristics of these contrast agents are presented in Table 5-1 A comparison between Feridex, Ferex and Bangs contrast agents. To determine the relaxivities of the contrast agents, we prepared phantoms of Bangs- Ferex and Feridex, at concentrations ranging from 0.1 to 1.5 µM fe/mL. Then, MRI was used to generate T_2 and T_2* maps to determine r_2 and r_2* values.

To obtain a T_2 map, we used a Carr Purcell Meiboom Gill Sequence (CPMG) sequence with variable TEs[80]. It is a spin echo-based sequence that starts with a 90º radio frequency pulse followed by 180º pulses. The parameters were TR=7500 ms, number of averages=1, FOV= 3x3 cm, matrix=128x128, acquisition time =16 minutes, number of echo times used was 128. Echo times started at 4ms and went to 512 ms in 4 ms increments.

To obtain a T_2* map, we used a multiple gradient echo sequence which is a gradient echo-based sequence commonly used with variable TEs to generate T_2* maps[128]. The parameters used were TR=1500 ms, number of averages=2, FOV= 3x3 cm, matrix=128x128, acquisition time=4 minutes, number of echo times used was 7. Echo times started at 3ms and increased in 4 ms increments to 27 ms.

These sequences use variable TEs and each TE was used to generate an image. The generated images were used to create a T_2 map which allowed the quantification of the SI value of a region of interest for each time point of a different TE, and then the SI values obtained were plotted against the variable echo times used in those sequences. The resultant T_2 and T_2*

relaxation curves were used to calculate the relaxation times T_2 and T_2* for each concentration of the contrast agent. The T_2 and T_2* values were computed by fitting the data to the monoexponential decay function. This process was automatically done by our Bruker MRI console using the following equation, to calculate T_2

$$Y = A + C \cdot \exp(-t/T_2)$$

where A is a constant that represents the absolute bias, C is the signal intensity and t represents the different echo times used in the imaging protocol.

And the following equation to calculate T_2*

$$1/T_{2^*} = 1/T_2 + 1/T'_2$$

where T'_2 is the effect of the inhomogeneities of magnetic field.

The obtained T_2 and T_2* values were used to calculated the relaxation rates R_2 and R_2*, where R=1/T. The final step to determine the relaxivity values r_2 and r_2* was plotting the R_2 and R_2* values against the different concentrations of the contrast agents used in phantoms. Then, a line was fitted through the resulting curve and its slope was measured by using the following equation from the Sigma plot software

$$y = y_0 + rx$$

r is either r_2 or r_2*.

As mentioned earlier, Bangs particles have a dual detection method. Aside from being detected with MRI and Prussian blue staining in histology, they can also be detected optically using fluorescent microscopy or xenogen system due to its fluorescent properties. The fluorophores incorporated into the Bangs particles were in the range of flash red (660-690 nm). To visualize the Bangs particle under a fluorescent microscope, a few drops of undiluted Bangs

particles were added to a histology slide and examined under the microscope. The images show that the particles could be detected clearly as red particles under TRITC filter.

To image Bangs particles in the xenogen system, the particles were diluted to different concentrations and put into glass NMR tubes for imaging. The IVIS xenogeny system (Dr. Peter Forsyth lab) was adjusted to the 660 nm wave length for imaging, and then images were taken.

Table 5-1 A comparison between Feridex, Ferex and Bangs contrast agents.

	Feridex	**Ferex**	**Bangs**
Size	80-180 nm	50-150 nm	0.9 μm
Chemical formula	$FeO_{1.44}$	$FeO_{1.44}$	Fe_3O_4
Cellular uptake	By lipofectamine	By lipofectamine	By lipofectamine
Fluorescent properties	N/A	N/A	Flash red (660-690nm)
Concentration of Fe	11.2 mg Fe/mL	10 mg Fe/mL	10 mg/mL
company	Advance Magnetix	Biopal Inc.	Bangs Laboratories
Approval for Human	Approved	Approved	Not approved

Positive contrast agent. Gado celltrack (Biopal, USA) is composed of gadooxide at a concentration of 10 mg Gd/mL and a size of 30nm. The same procedure, as negative contrast agents, was used to prepare the phantoms. The r_1 of Gado celltrack was calculated using inversion recovery True FISP[80] similar to the method presented in Section 4.2.

5.3 Results

The inversion recovery True FISP, CPMG and multi echo gradient echo sequences generated T_1, T_2 and T_2* maps, respectively, which allowed obtaining relaxation times and relaxivity values of the different contrast agents, with no artefacts as shown in Figure 5-1 and Figure 5-3.

Negative contrast agents (Bangs, Ferex and Feridex). The phantom relaxivity graphs r_2 and r_2* are shown in Figure 5-1 and the calculated relaxivity values are presented in Table 5-2.

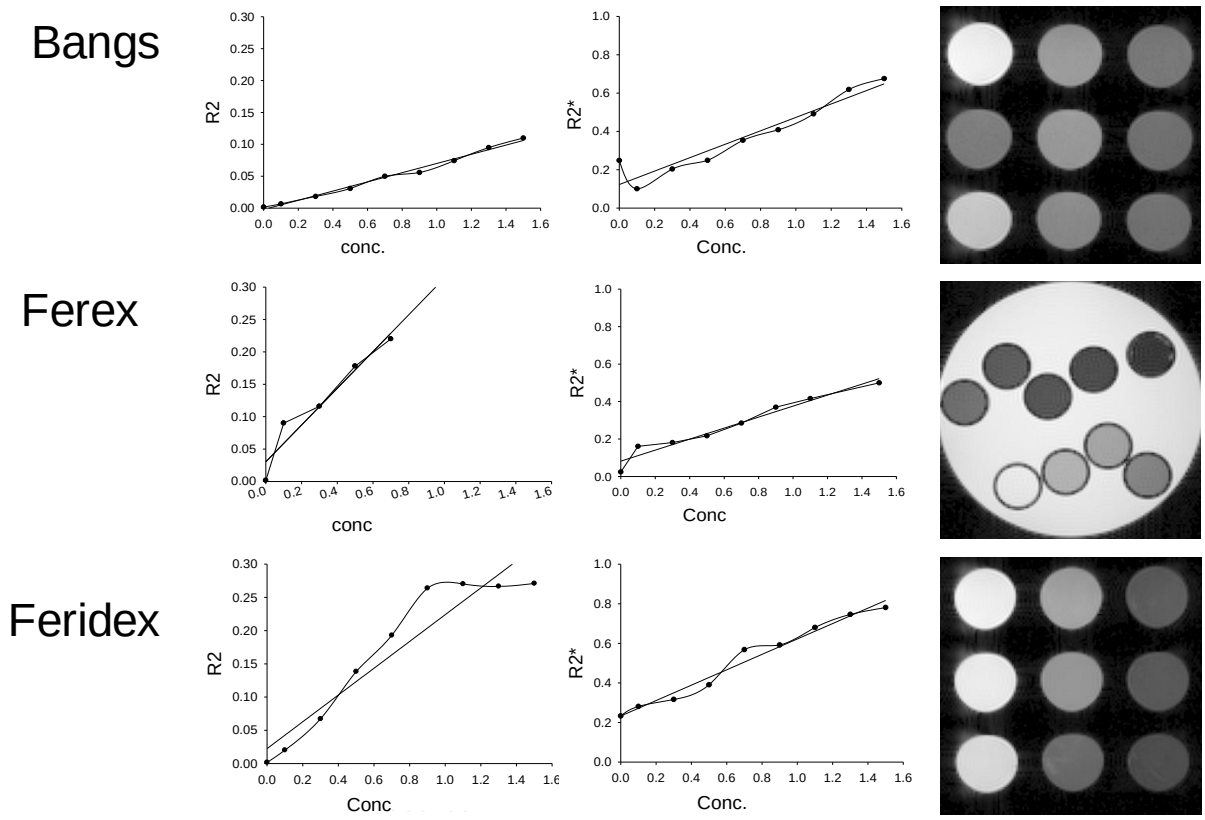

Figure 5-1 Relaxivity graphs for Bangs, Ferex and Feridex particles and the corresponding MRI phantom images showing the different concentrations of contrast agents dissolved in PBS in small tubes, then embedded in a bigger containers containing agarose to minimize the imaging artefacts.

Table 5-2 The relaxivity values of the Feridex, Ferex and Bangs contrast agents.

	Feridex	**Ferex**	**Bangs**
Relaxivity ($mM^{-1}s^{-1}$)	r_2=201.5±24.9 r_2*=389.4±22.9	r_2=283.6±44.1 r_2*=293.7±25.6	r_2=72.1±2.6 r_2*=350.3±40

In the xenogen system (Figure 5-2 A), the different concentrations of contrast agent appeared as dark-red to black colour (Figure 5-2 B). The Bangs fluorescent properties were detected under fluorescent microscope and appeared as red particles (Figure 5-2 C).

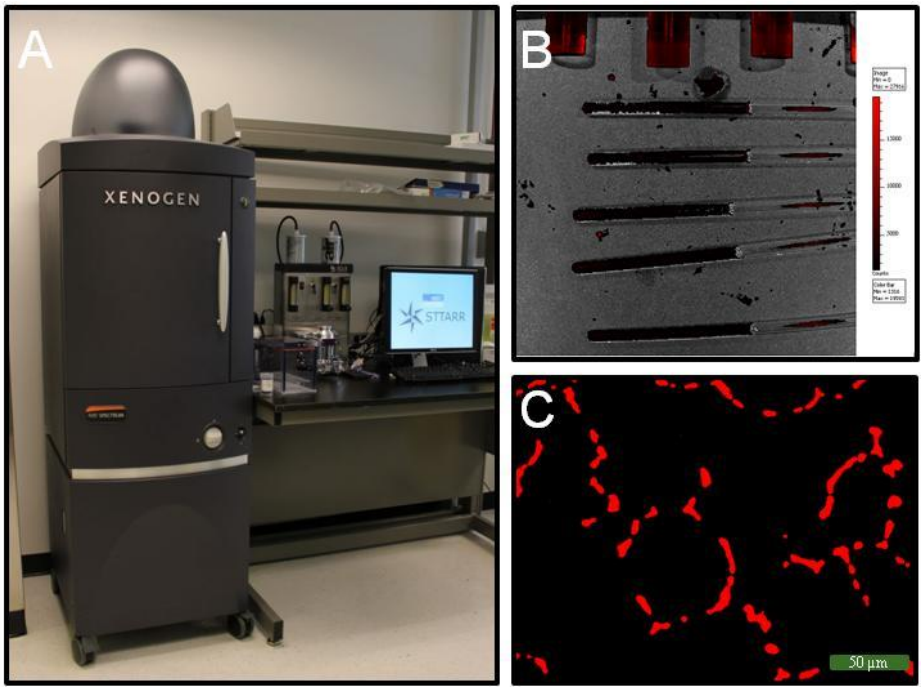

Figure 5-2 Assessment of the fluorescent properties of the Bangs particles. (A) The xenogen machine and the processing console. (B) An image generated by the xenogen system showing the five NMR tubes filled with different concentrations of Bangs particles appear as dark red to black. (C) Bangs particles examined under fluorescent microscope using TRITC filter.

Positive contrast agent (Gado celltrack). The phantom relaxivity graph is shown in Figure 5-3 and the calculated relaxivity value of Gado celltrack was $r_1 = 31.2 \pm 0.8\ mM^{-1}\ s^{-1}$.

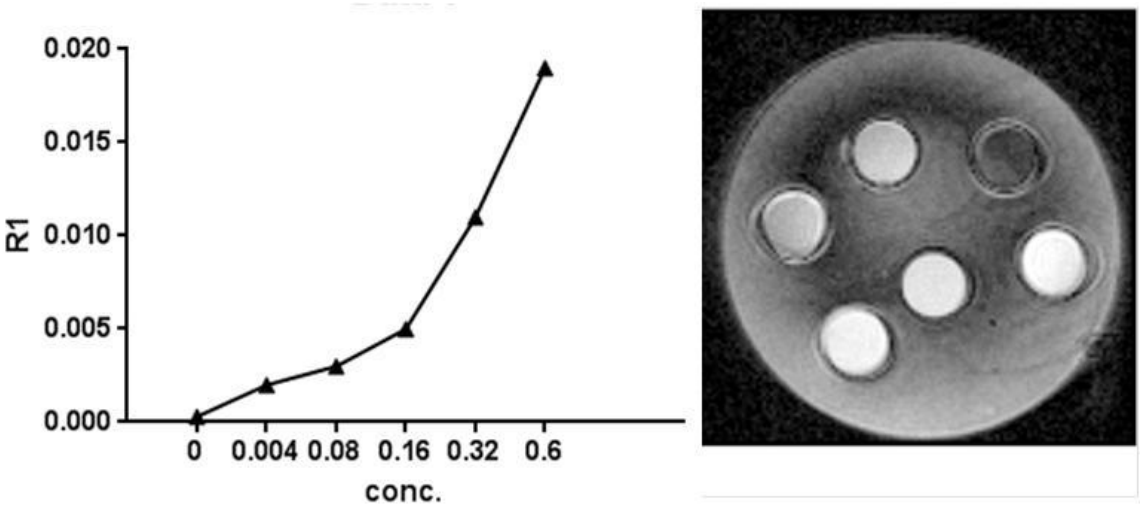

Figure 5-3 Gado celltrack relaxivity graph and an inversion recovery True FISP image of its phantom containing showing the different concentrations of Gado celltrack dissolved in PBS in small tubes, then embedded in a bigger tube containing agarose to minimize the imaging artefacts.

5.4 Discussion

The MR relaxivity results obtained enabled the evaluation of the relatively new contrast agents (Ferex, Bangs, Gado celltrack). It indicated that Ferex and Bangs had sufficient relaxivity as T_2 contrast agents and that Gado celltrack had sufficient relaxivity as a T_1 contrast agent.

To compare relaxivity results from different systems, one has to bear in mind the variables that affect the relaxivity results such as: the imaging sequence and parameters, the temperature, the PH, and the strength of the magnet used in the study. This made our results different from the previously obtained relaxivity values. Our calculated r_2* relaxivities at 9.4 T for the Bangs

particles was 350.3 $mM^{-1}s^{-1}$ and for the Ferex was 293.7 $mM^{-1}s^{-1}$, while the r_2* relaxivity obtained by Hinds *et al.* at 11.7 T for the Bangs particles was 851 $mM^{-1}s^{-1}$and for other iron particles was 498 $mM^{-1}s^{-1}$ [135]. For this reason, we needed to investigate the relaxivities of new and old contrast agents using our MRI system and compare their relaxivities together for accurate evaluation of the new contrast agents. A similar concept was used by Hinds in his study to compare the new Bangs particles with the previously used ferumoxide particles[135].

For our negative contrast agents, we found that Ferex and Bangs had r_2* relaxivity values that are close to the r_2* of the previously used Feridex. Moreover, the Ferex r_2 value was higher than Bangs and Feridex r_2. This indicates that Ferex and Bangs have sufficient relaxivity to be used as T_2 contrast agent for our model; meeting or exceeding what was obtained with Feridex. The Bangs particles showed significant fluorescent properties when examined under fluorescent microscope. This dual detection system will be useful in the detection of labelled ESCs in histological section and validation of MRI results. However, the xenogen results did not provide enough distinction between the different concentrations of contrast agent. This suggests that further optimization of the imaging parameters are needed.

Ferex had the highest r_2 value compared to the Bangs and Feridex which means it can be used as an efficient T_2 contrast agent with T_2 weighted images obtained by SE sequences. Relative to GE sequences, SE sequences minimize imaging artifacts that are caused by magnetic field inhomogeneity which made it more favourable[48]. Knowing that T_2* weighted images could only be obtained with GE[48,128], we tried to avoid using Ferex as a T_2* contrast agent, and instead we used it as a T_2 contrast agent with SE sequence. The latter combination was more favourable than using T_2* contrast agent with GE sequences because SE sequences will minimize the imaging artefacts[27].

For our positive contrast agent, we found that Gado celltrack had an r_1 of 31.2 ± 0.8 mM^{-1} s^1, which is similar to the previously obtained Gd r_1 (32 mM^{-1} s^-1) at 9.4 T by Fatouros *et al.*[136]. This indicates that the Gado celltrack particles can be used as an efficient T_1 contrast agent similar to the ones previously used.

Based on our work, it can be concluded that Bangs and Ferex will have sufficient relaxivity as T_2 contrast agents for our study, assuming that labelling efficiency can meet or exceed that previously obtained with Feridex. Also, Gado celltrack had sufficient r_1 relaxivity value which suggests it can be used as a T_1 contrast agent for our study.

Chapter Six: **Labelling and differentiation of embryonic stem cells with different contrast agents and imaging them *ex vivo* with MRI**

6.1 Introduction

Implantation of differentiated Embryonic stem cells (dESCs) in bone fracture has proved to enhance the healing process[30]; however the exact *in vivo* behaviour and fate of the cells is not fully understood. The use of a non-invasive cell tracking method will assist in understanding the *in vivo* behaviour and fate of the cells. Magnetic resonance imaging (MRI) could be a promising tool for non-invasive imaging and tracking of cells[10]. While MRI offers high resolution and reasonable signal to noise ratio, it is still important to use contrast agents to improve imaging sensitivity and generate enough contrast between the host tissue and the implanted cell therapy[10,74,75]. This is done by labelling of the cells with MRI contrast agents, which could be challenging due to the toxic effects of the contrast agents on the cells. These toxic effects might adversely affect the cell proliferation and differentiation capacity[10,137], and consequently affect the treatment outcome[137]. Additionally, it is not easy to make stem cells internalize the label without external assistance[81]. Therefore, it was important to develop a way to label cells that does not adversely affect the cell health, and results in the cells containing sufficient contrast agent to make them visualized in MRI. This section describes the development of an optimized protocol for labelling and differentiation of ESCs, and using a quantification method to track the cells with MRI. All the work done in this section was *ex vivo*.

When labelling the ESCs with contrast agents the adverse effect of the labelling procedure on the cells should be assessed. Optimization of the labelling procedure by adjusting the dose and timing should be considered to avoid the toxic effects on cell viability, proliferation and differentiation capacity. It was previously reported that specific doses of iron oxide labelling

have no significant adverse effects on the cells because it is coated with a dextran coating[81]. However, some adverse effects, such as reduced differentiation capacity of MSCs, have been reported[137]. Iron oxide and gadolinium particles have been used to label and track different types of cells, such as neural, cardiac, blood, immune and stem cells *in vivo*[10,64,69,81,111,124,132,138].

Transfection agents play an important role in the labelling process of stem cells[71,81]. They are negatively or positively charged molecules that bind to the contrast agents by electrostatic interaction[139]. In our experiments, both the cell membrane and the contrast agents were negatively charged, therefore the transfection agent, lipofectamine, was used to assist the labelling process.

The cell labelling process can be carried out either *in vivo* or *ex vivo*[10,73,140]. *In vivo* cell labelling was previously done to label phagocytic cells by systemic or local injection of the label[73]. After administration of the labelling material, the phagocytic cells such as kupffer cells in the normal liver tissue will uptake the iron leading to increase the detectability of lesions[73]. This technique was also used with the contrast agent SPIO to image inflammatory events such as tumours[141]. The problem with this technique is the non-specificity which can cause systemic adverse effects such as hypotension and lumbar pain[73]. However, it offers simplicity, which makes it feasible to apply in clinics. In contrast, *ex vivo* cell labelling requires cell isolation, culturing, labelling *in vitro* and then implanting the cells back *in vivo*[135]. This technique is costly and time consuming but it guarantees the efficiency and specificity of cell labelling[10]. In our study, we chose *ex vivo* cell labelling because the cells used were derived from embryos and they had to be differentiated *in vitro* before implantation.

Undifferentiated ESCs have the potential to form tumours *in vivo*. For this reason, it is important to differentiate ESCs before implanting them. In our study, we used a 3D collagen

construct differentiation protocol that was previously developed by Krawetz et al.[29,44]. An advantage of using the 3D collagen differentiation protocol is that it eliminates the possibility of tumour formation *in vivo*[30]. It also directs the cells into an osteogenic lineage which will provide the bone fracture with needed cells such as osteoblasts[44]. Finally, the 3D cell-construct acts as the mechanical support needed to keep the cells at the site of fracture after implantation. Because the dESCs obtained by this protocol was previously well characterized[44], we decided to use only one stain (Toluidine blue) to confirm differentiation. We looked for extracellular matrix fibers.

The final step in this study was to examine the detectability of the labelled cells *ex vivo* using MRI before moving to the *in vivo* stage. We investigated the MR imaging of labelled ESCs suspended in media and dESCs in 3D collagen constructs to study how the labelling affected the SI changes. We used the SI analysis as a quantitative measure to assess labelled cells *ex vivo* and *in vivo*[128]. SI corresponds to the proton concentration, relaxation rate and the sequence used. Thus it can be used to reflect changes in the relaxation rate. It has been previously used to assess labelled stem cells[127,142,81,63].

In this chapter, we investigated how to combine cell labelling and differentiation protocols for use in the rest of this project. In addition, we determined the labelling doses and an estimate of the number of cells required to cause SI changes for MRI visualization.

6.2 Materials and methods

ESCs Culturing. The cell line used was a D3 ESCs line obtained from male Sv 129 mice. ESCs were maintained in a pluripotent state on either gelatinized (0.1% solution, Type B gelatin from Bovine Skin, Sigma) primaria treated dishes (general laboratories) or plates containing a layer of mouse embryonic fibroblasts (MEF). The culture medium used contained high-glucose Dulbecco's modified eagle medium (DMEM, Gibco, CA) supplemented with 15% fetal bovine

serum (FBS, Gibco, CA), 1% nonessential amino acids (Invitrogen), 2.5 mL Penicillin/Streptomycin (Gibco, CA), 0.1 mM 2-Mercaptoethanol (Sigma), and 1,000 U/mL leukemia inhibitory factor (LIF, Invitrogen)[72] .Cells were sub-cultured every second day.

ESCs labelling. To label the cells with a negative contrast agent, a stock solution was prepared. It was composed of iron label (Feridex, Ferex or Bangs) and lipofectamine 2000 (Invitrogen life technologies, Canada) at a concentration of 25 µg/mL in serum-free optimem medium (Invitrogen)[81]. Then, the stock solution was added to an 80% confluent ESCs monolayer and incubated for 24 hours in 5% CO_2 at 37ºC. After 24 hours, the cells were washed with phosphate buffered saline (PBS, Invitrogen), trypsinized (0.25% Trypsin EDTA, Gibco), then washed again and collected for further experiments. This is our standard cell labelling protocol that will be used in the following experiments unless otherwise stated.

To label the cells with a positive contrast agent, a stock solution of Gado celltrack (Biopal Inc. USA) and lipofectamine at a concentration of 0.08 mg/mL in optimum (Invitrogen) medium was prepared[132]. The stock solution was added to 80% confluent cells and incubated for 24 hours in 5% CO_2 at 37ºC. After 24 hours, the cells were washed, trypsinized and collected for further experiments.

Labelled ESCs viability and proliferation assessment. To assess cell viability after labelling, a haemocytometer-based trypan blue exclusion cell counting technique was used. This technique is used to determine the number of viable and non-viable cells in a cell suspension. Viable cells possess an intact cell membrane that does not allow the passage of dyes while dead cells do not, allowing them to be detected by uptaking the trypan blue stain and turning blue. Briefly, a 100 µl of cell suspension was mixed with 100 µl of trypan blue stain (Sigma) and then visually examined under the microscope to determine whether the cells were stained or not.

Viable cells had a clear cytoplasm while dead cells had a blue cytoplasm. The cell counting was done manually; the numbers were recorded and used for analysis.

To assess the effect of labelling on the cell viability, ESCs were labelled with Ferex, Bangs, and Gado celltrack, per our standard labelling protocol and their viability was assessed. Unlabelled ESCs viability was assessed as a control. To assess the proliferation capacity of the labelled cells, we compared cell counts of Ferex-labelled ESCs at day 1 and day 4 post labelling to detect the increase in cell number.

ESCs differentiation. To differentiate ESCs into the osteogenic lineage a 3D collagen construct *in vitro* differentiation protocol was used. In this protocol, bovine collagen 1 (Advanced Biomatrix, USA) was polymerized into a two-dimensional gel using 10mM beta-glycerol phosphate (BGP). Specifically 80% v/v 3 mg/mL collagen 1 solution was mixed with a single cell suspension (1 million cells/mL) and 20 % v/v BGP dissolved in 5X concentrated DMEM. The 5X concentrated DMEM was generated by dissolving powered DMEM (Invitrogen, USA) in 1/5 the recommended amount of water and supplemented with 15 % FBS (Invitrogen, USA), 1 % non-essential amino acids, 50 U/mL penicillin and 50 µg/mL Streptomycin, and 0.1 mM β-mercaptoethanol.

To test the differentiation capacity of ESCs, the cells were differentiated for 16 days into the osteogenic lineage[44]. After differentiation, the cells were fixed, sectioned, and then stained with toluidine blue stain. Toluidine blue is an acidophilic dye which stains acidic tissue components such as bone[15,143].

Combining the labelling and differentiation protocol. After establishing the labelling protocols, we needed to combine them with the differentiation protocol to obtain labelled, dESCs that could be used for our cell tracking bone fracture model. We tested two different methods to

develop an ESCs labelling-differentiation protocol. In the first protocol, undifferentiated ESCs were labelled with Ferex using our standard labelling protocol, and then differentiated into osteogenic lineage using a standard differentiation protocol[44]. In the second technique ESCs were differentiated then labelled. The success of labelling was confirmed by Prussian blue (PB) staining of cells.

***Ex vivo* MRI of labelled cells.** Four phantoms were studied; three of them had undifferentiated labelled cells suspended in agarose while the fourth phantom had differentiated labelled cells in a 3D collagen construct.

Phantom1. The purpose of this phantom was to compare Ferex and Gado celltrack-labelled cells with their corresponding MRI contrast agents as a positive control. MR imaging was performed using RARE T_2 and FLASH sequence to study how the iron appeared in both sequences.

A chambered cover slide was filled with agarose. For Ferex-labelled cells, ~ 4000 undifferentiated ESCs suspended in 5 µl of cell culture media were injected at one side of the chamber while 5 µl of Ferex were injected at the other side. Then, the phantom was imaged with FLASH MRI with the following parameters; TR/ TE=125/4 ms, FOV=2.5x2.5 cm, matrix=256x256 cm, flip angle=30º, and scan time= 32 s. Additionally RARE T_2 MRI sequence was used and compared to FLASH MRI. The parameters of the RARE T_2 was; TR/TE= 2000/20 ms, rare factor=4, number of averages=1, FOV=2.5x2.5 cm, matrix=256x256, and scan time=2m 8 s.

For the Gd-labelled cells, we used almost triple the number of labelled cells used in Ferex labelling because Gd-labelled cells has lower detectability than Ferex in MRI. 5 µl of cell suspension containing 13,500 undifferentiated ESCs were injected at one side of the chamber

while 5 µl of Gd were injected at the other side. Then, RARE T_1 MRI was performed with the following parameters; TR/TE= 500/7.5 ms, rare factor=4, FOV=2.5x2.5 cm, matrix=256x256, and scan time=24 s.

Phantom 2. The purpose of this phantom was to estimate the amount of labelled cells needed to be detected in MRI. Gado celltrack-, Bangs- and Ferex-labelled cells were tested in this phantom. Two holes were drilled at the top of a plastic syringe. Then the syringe was filled with agarose. Two concentrations of each type of labelled cells (335 and 3350) were injected into the syringe from the top holes. Three syringes were prepared, one for each contrast agent. Then, the syringes were imaged with RARE T_1 sequence for Gd-labelled cells (TR/TE 500/7.5 ms) and RARE T_2 for Bangs-and Ferex-labelled cells (TR/TE 2000/20 ms).

Phantom 3. This phantom was used to study how the different concentrations of labelled cells affect the SI values in Bangs, Ferex-and Gado celltrack-labelled cells. Small glass tubes were filled with two concentrations of labelled cells suspended in cell culture media. The lower tube had about 2000 cells while the upper tube about 500 cells. The glass tubes were then immersed in agar and imaged with MRI. In this phantom, the cell suspension was put in glass tubes instead of injecting it directly into the agarose to avoid the dissociation of the cell solution into the agarose and to minimize the imaging artefacts caused by plastic tubes. The contrast agents used to label the cells were Gado celltrack, Bangs and Ferex. After that, the phantoms were imaged with MRI. Bangs and Ferex were imaged with RARE T_2w sequence while Gado celltrack was imaged with RARE T_1w sequence with the same parameters mentioned in the previous phantoms. Then, MR data were fed into Marevisi software to obtain SI values of the different cell concentrations. Briefly, mean SI values were computed from manually defined regions of interest (ROIs) of equal number of pixels applied on each cell concentration.

Phantom 4. The last phantom study was performed to determine the minimum detection threshold of cells. Unlike the previous phantoms, Ferex-labelled dESCs in 3D collagen constructs were used in this phantom. Different numbers of cells within their gel construct were put into small epindorf tubes then immersed into a bigger agarose filled tube to minimize imaging artefacts caused by air. Cell numbers used were (1)170.000, (2) 42.500, (3) 21.250 and (4) a negative control tube with unlabelled ESCs. RARE T_2w and FLASH MRI were undertaken and data were analysed similar to phantom 3.

Histological detection of iron based contrast agents ex vivo

Prussian blue stain. In order to confirm the uptake of negative label, we used a histochemical stain, Pearl's Prussian blue (PB) (Biopal Inc. USA). It stains iron dark blue. The PB stain can identify iron-based contrast agents such as Ferex ($FeO_{1.44}$), Feridex ($FeO_{1.44}$), and Bangs (Fe_3O_4). Additionally, any ferric ions (+3) present in the tissue combines with the ferrocyanide and form a bright blue pigment of potassium ferric ferrocyanide $Fe_4[Fe(CN)_6]_3$[144]. Iron is normally present in the tissue in the form of iron-bound proteins (eg; ferritin, transferin, and hemosidrin). Therefore, PB can identify ferric iron loosely bound in protein complexes such as ferritin and hemosidrin because free Fe^{+3} is released upon the treatment of tissue with hydrochloric acid[145]. Iron that is strongly bound as heme in hemoglobin does not react [146]. In conclusion, PB stain stains iron-based contrast agents, hemosidrin and other ferric ions but it does not stain hemoglobin[147]. This test is sensitive and can detect single granules of iron.

Before staining, cells were fixed using a solution of 40% formalin (Biopal Inc. USA) and 25% glutaraldehyde (Biopal Inc. USA) in PBS for 10 minutes. After fixation, the PB staining protocol was applied. In the first part of the PB reaction, the iron (ferric ions) was released by

denaturing the binding proteins with 20% hydrochloric acid, followed by treatment with 10% potassium ferrocyanide.

Fluorescent detection of Bangs. The Bangs-labelled ESCs were examined under a fluorescent microscope to detect their fluorescent properties. The images obtained were co-registered with PB stained images of the same section to verify that the fluorescence was emitted from the Bangs particles.

No histological detection method was used to investigate the Gado celltrack uptake by the cells. Instead, Gado celltrack cellular uptake was assessed using MRI and SI measurements from phantom 3.

Statistical analysis of labelled cell viability. For cell viability data, Kruskal-Wallis non-parametric test was used to compare the number of viable cells for 4 groups (Ferex, Bangs and Gado celltrack-labelled cells, and a single control group of unlabelled cells), followed by Dunn's multiple comparison test. The statistical test was performed using GraphPad Prism software package. The confidence level of $P<0.05$ was considered statistically significant.

6.3 Results

Ex vivo MRI of labelled cells.

Phantom 1 (In a chambered covered glass slide, Ferex- and Gado celltrack-labelled cells were injected in agarose on one side and their corresponding contrast agents on the other side as a positive control). The 4000 Ferex-labelled ESCs were detectable and they appeared as a hypointense area with susceptibility artefacts surrounding it in FLASH and RARE T_2 sequence (Figure 6-1 C & D). Gd-labelled cells appeared as hyper and hypointense areas in a RARE T_2 sequence (Figure 6-1 E). Despite the high number of Gd-labelled cells they were less detectable than Ferex-labelled cells. The low detectability of Gd could be due to the unoptimized phantom

design where air bubbles were formed at the site of Gado celltrack injection, which caused signal voids into the images and interfered with the detection of Gado celltrack-labelled cells.

In the FLASH GE image, the Ferex-labelled cells and the Ferex contrast agents were detected as a bloom in the MR image due to the susceptibility effects of iron particles that is enhanced in GE sequences (Figure 6-1 A & C).

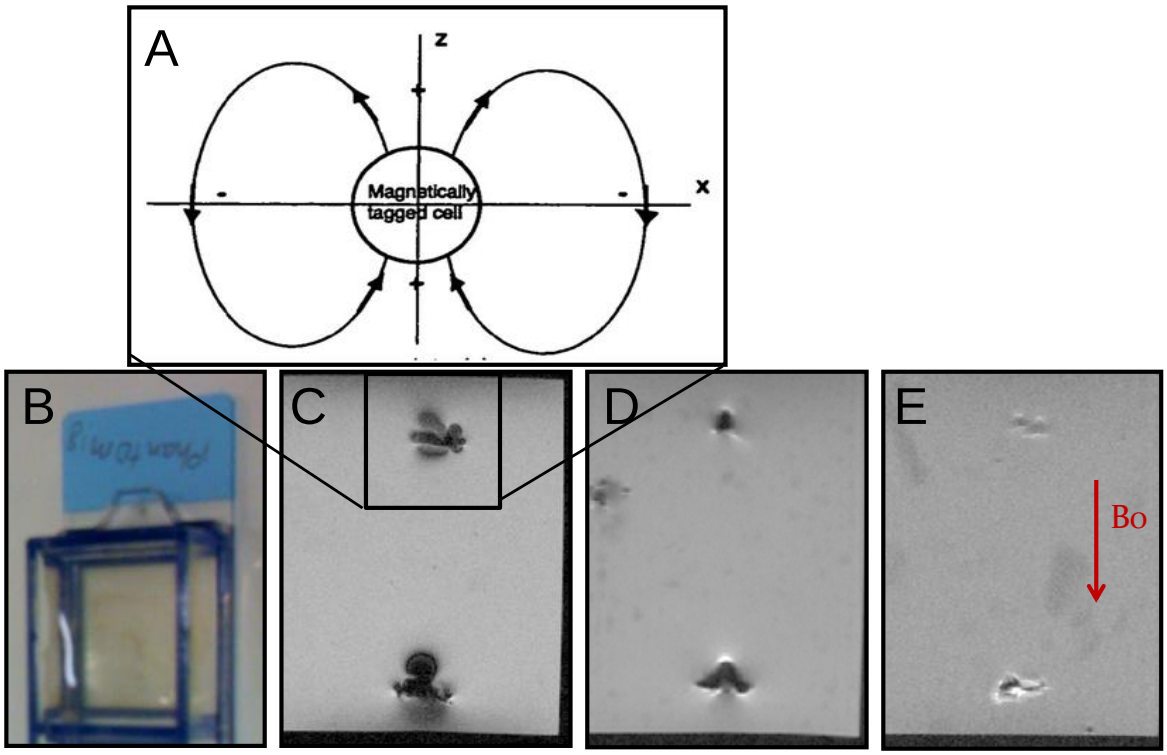

Figure 6-1 (A) The magnetic field of an iron-labelled cell and its relation to the main magnetic field, the magnetic field is enhanced in the z-direction and suppressed in the x-direction (reproduced from Cunningham)[148]. (B) Chambered covered slide filled with agarose. (C) FLASH image. (D) RARE T_2 w image. (C & D) has Ferex-labelled ESCs (4000 cells) at the top of the image and 5 µl of Ferex solution at the bottom. (E) RARE T_1 w image has Gado celltrack-labelled ESCs (13,500 cells) at the top and 5 µl Gado celltrack solution at the bottom.

Phantom 2 (Gado celltrack-, Bangs- and Ferex-labelled cells at different concentrations were placed in a syringe full of agarose) Phantom 2 was not appropriate for determining the number of labelled cells needed to be detected in MRI, but was useful for method development. Initially, the set up did not enable the detection of the cells because the cells dissolved right after the injection when they were injected in fluid state agarose. In the second attempt, the cells were injected after the solidification of agarose. Likewise, this approach failed because the injection of the cells led to the formation of air bubbles at the site of injection, which appeared as signal voids in the MRI (Figure 6-2). Subsequently, we decided to use a different phantom set up to measure the minimum detection threshold.

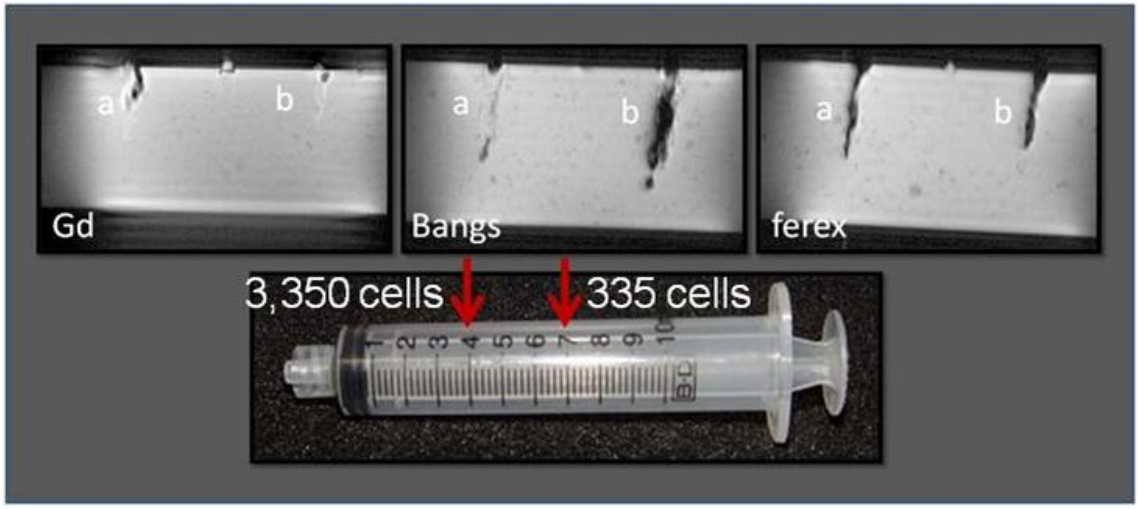

Figure 6-2 MRI phantom of labelled ESCs. The plastic syringe is filled with agarose. Labelled ESCs were injected from the holes at the top of the syringes as illustrated by the red arrows. Hole (a) 3,350 cells and hole (b) 335 cells.

Phantom 3. (Different numbers of Bangs-, Ferex-and Gado celltrack-labelled cells were suspended in solution in glass tubes, then the tubes were immersed in agar) The lower tube with 2000 cells in the Bangs and the Ferex phantoms appeared more hypointense than the upper tube

with 500 cells which was confirmed in the corresponding SI measurements. Increasing the number of Bangs-and Ferex-labelled cells from 500 to 2000 cells decreased the corresponding SI values from ~ 2.3 x 10^7 to ~1.2 x 10^7 (Figure 6-3 A & B). In the Gado celltrack phantom, the lower tube with 2000 cells appeared more hyperintense and it had higher SI value than the upper tube with 500 cells. Increasing the number of Gado celltrack-labelled cells from 500 to 2000 cells increased the corresponding SI value from 8.4 x 10^6 to10 x 10^6 (Figure 6-3 C).

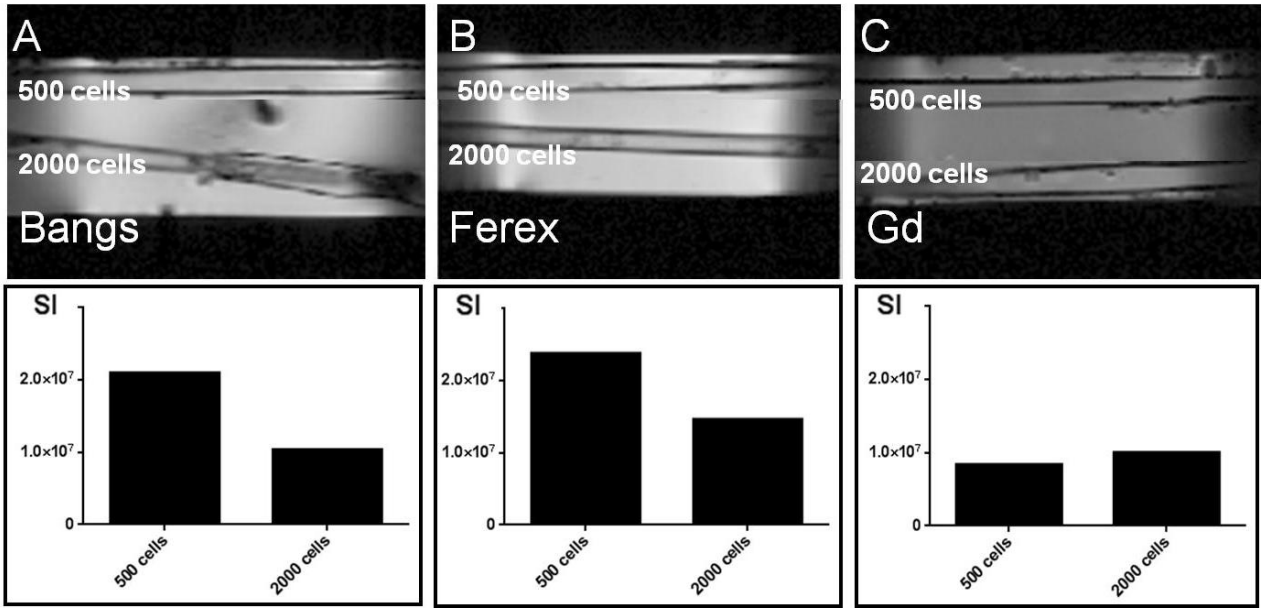

Figure 6-3 MRI phantom of Bangs, Ferex and Gado celltrack-labelled cells (500 and 2000 cells) and their corresponding SI measurements.

Phantom 4. (Different numbers of dESCs were imaged to determine the minimum detection threshold of cells) All the different numbers of the Ferex-labelled dESCs in 3D collagen constructs were detected in the MRI (Figure 6-4 B). Thus, we did not know the minimum detection threshold of labelled cells, but we were able to detect up to ~21,250 labelled cell. Interestingly, increasing the number of labelled cells from 21,250 cell to 170,000 cell decreased the signal intensity from 13185 to 9922 (Figure 6-4 C).

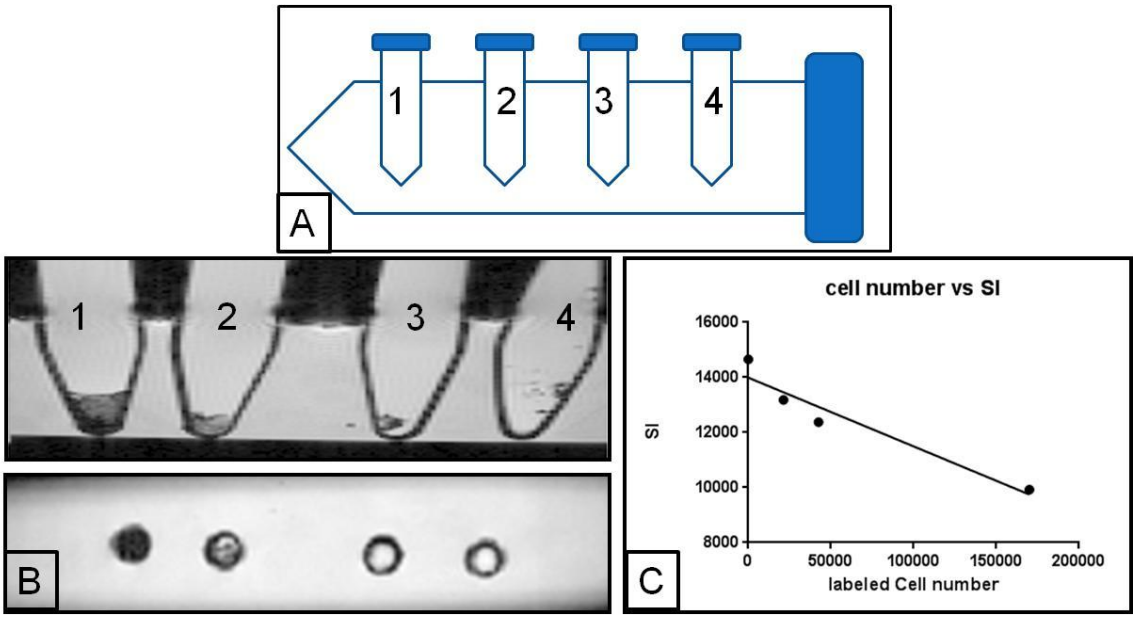

Figure 6-4 MRI phantom of Ferex-labelled dESCs with different cell numbers. (A) Plastic centrifugation tube filled with agarose and cut opened from the top to fit four epindorf tubes containing the different numbers of labelled cells. (B) FLASH MR images of phantom 4. This phantom contained four tubes, three of which had different numbers of Ferex-labelled dESCs in 3D scaffolds. (1) 170,000 cells, (2) 42,500 cells, (3) 21,250 cells. The fourth tube was a control with unlabelled cells. (C) SI data plotted against the different cell numbers showing decrease in SI values with increasing the number of Ferex-labelled cells.

Confirmation of labelling using Prussian blue (PB) stain. Examples of PB stains of ESCs labelled with Ferex and lipofectamine for 24 hours are shown in Figure 6-5A & B. The iron appeared as bright blue pigment. For better visualization of iron location within the cells we used nuclear fast red as a counter stain to detect the ESC nucleus and cytoplasm. The resulting images showed that the iron (blue spots) and the cells (red) were co-localized. This confirms that iron is inside the cells as illustrated in (Figure 6-5 C).

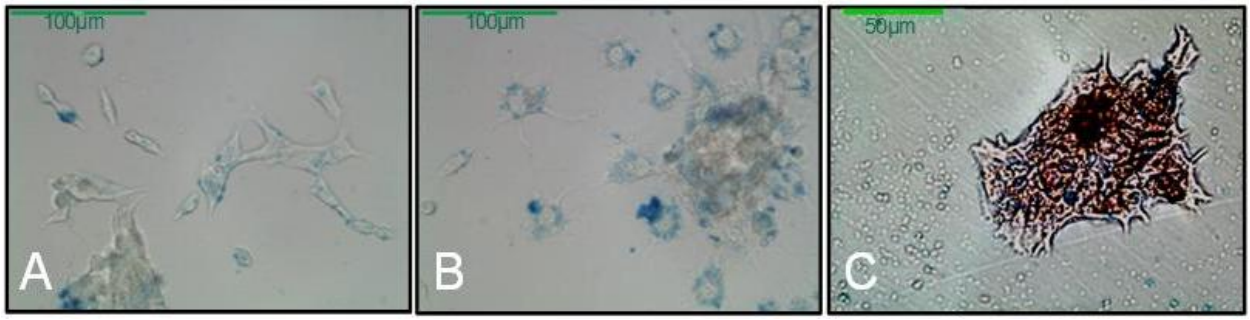

Figure 6-5 Ferex-labelled single layer of ESCs. (A & B) stained with PB and iron appears as blue spots. (C) PB stained section and counterstained with nuclear fast red. Different aggregates of ESCs appears as red areas and iron appears as blue spots.

Assessment of ESCs differentiation. Toluidine blue staining of dESCs showed positively stained cells (Figure 6-6) which suggested osteogenic[149] or chondrogenic[5] differentiation.

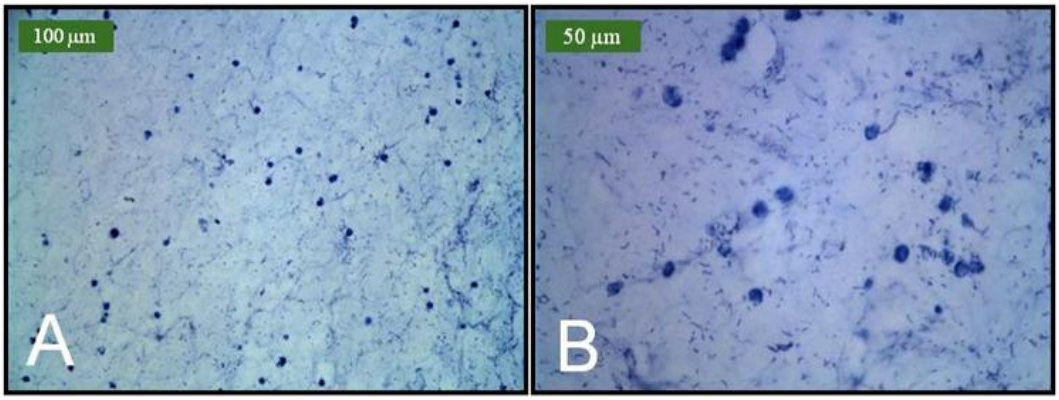

Figure 6-6 ESCs differentiation in gel constructs for 16 days, and then processed and stained with toluidine blue stain. It shows blue cells and matrix, suggesting differentiation.

Fluorescent detection of Bangs. The Bangs cells showed positive fluorescent properties upon examination under fluorescent microscope. The location of iron positive cells co-registered with the location of positive fluorescent cells (Figure 6-7).

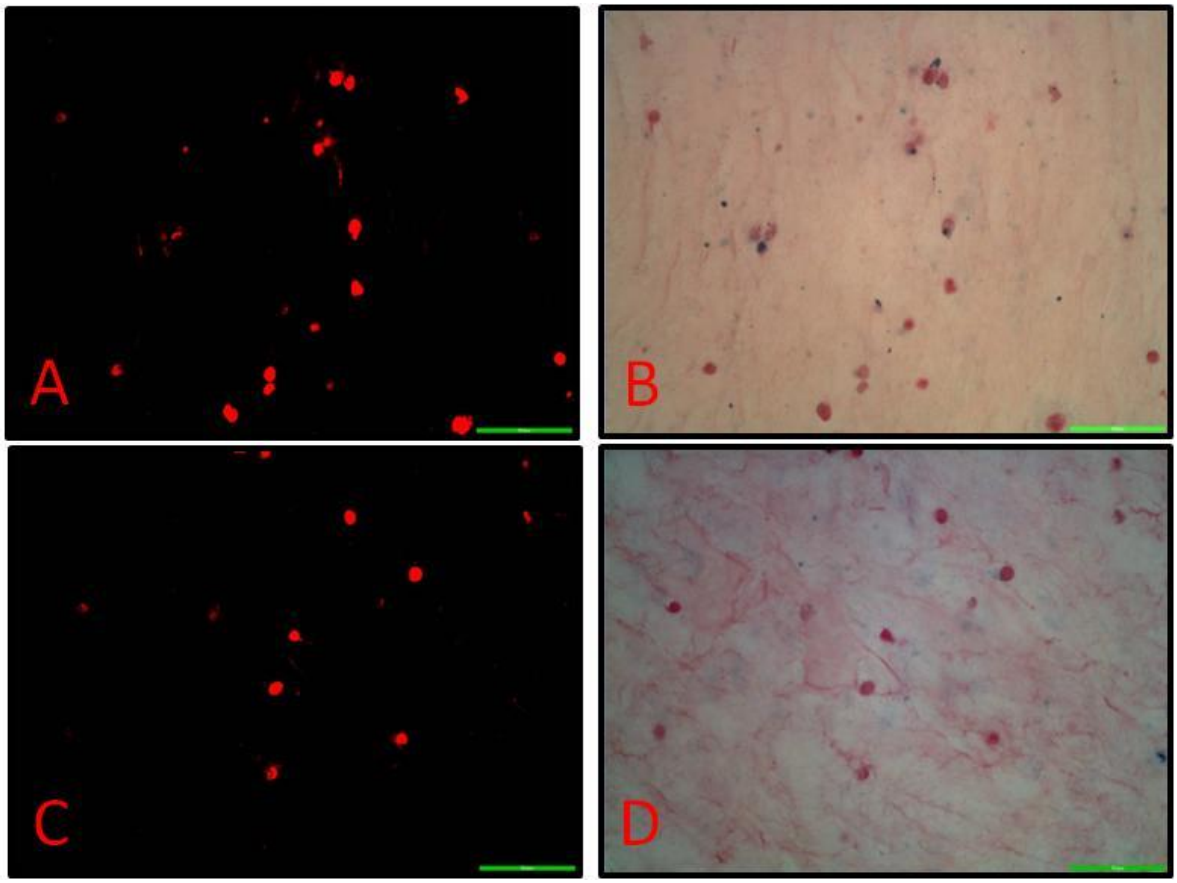

Figure 6-7 Bangs-labelled ESCs then differentiated for 16 days examined under TXred showing positive fluorescing signal (A) and under bright field stained with PB showing iron particles inside the cells (B). Unlabelled ESCs examined under TXred showing positive fluorescent signal (C) and under bright field stained with PB demonstrating absence of iron particles (D). Scale bar 50 µm.

The labelling-differentiation protocol selection. In the ESCs that were differentiated then labelled, the PB stain showed negative results and no iron was detected inside the cells (Figure 6-8 A), while in the ESCs that were labelled then differentiated, positive results were demonstrated by the presence of blue iron spots inside the cells (Figure 6-8 B). In both protocols, where the labelled or unlabelled cells were differentiated for 16 days, the resulted tissue constructs showed similar morphology. This means that the labelled cells had a similar differentiation pattern like the unlabelled cells which indicates that labelling of the ESCs with Ferex contrast agent did not compromise their differentiation capacity.

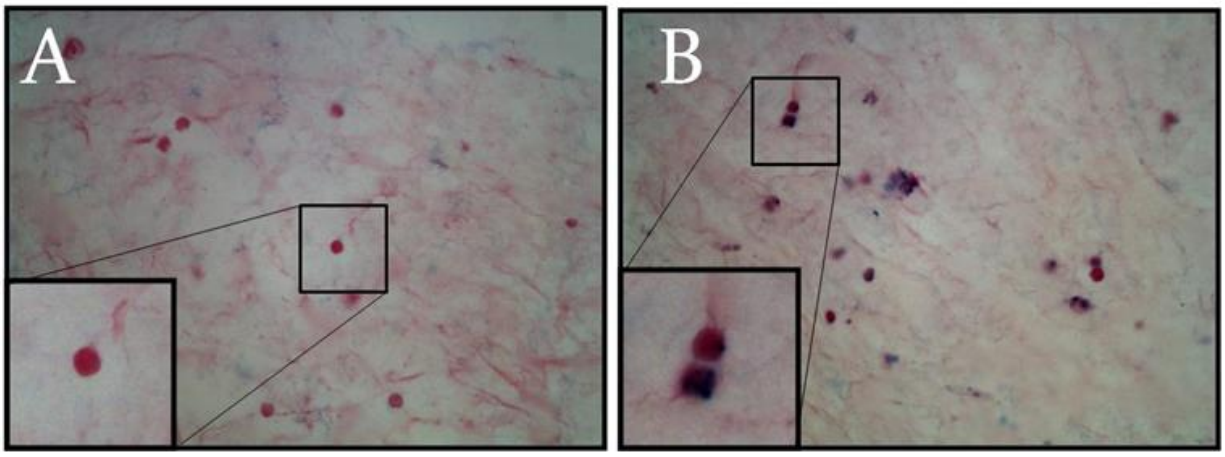

Figure 6-8 Labelled ESCs at 25 µg fe/mL stained with PB and nuclear fast red. (A) ESCs which were differentiated first then labelled stained negatively. (B) ESCs which were labelled then differentiated stained positively.

Labelled ESCs viability and proliferation assessment. The viability assay demonstrated no statistically significant decrease of cell viability after labelling with the different contrast agents when compared to the control unlabelled cells (P value=0.11 in Kruskal-Wallis test) (Figure 6-9 A). The cell proliferation assessment showed that the cells tripled their number within 3 days from 12×10^4 to 38×10^4 (Figure 6-9 B).

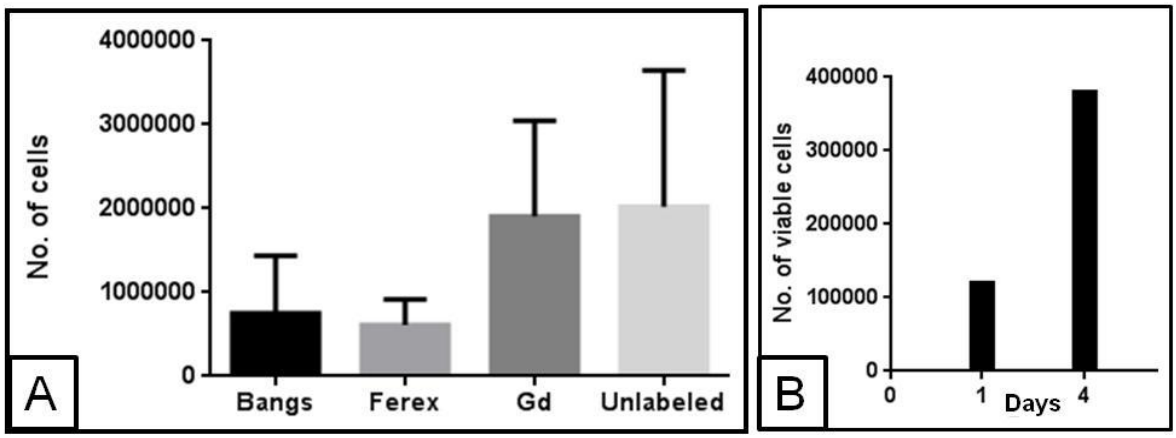

Figure 6-9 (A) Cell viability of labelled ESCs with Bangs, Ferex and Gado celltrack, and a control group of unlabelled ESCs. (B) Cell density at day 1 and day 4 post Ferex labelling.

6.4 Discussion

To monitor stem cells *in vivo* in tissue-engineering applications, the cells need to be labelled and tracked efficieintly[10]. An ideal cell tracking system is one where the cells are effectively labelled without adversely impacting their proliferation and differentiation capacity. Furthermore, the labelled cells should be visualized in MRI. The ESCs labelling protocol used in this study enabled the cell uptake of the contrast agents without adversely affecting the cells. Additionally, the labelled cells were detected in MRI through the SI changes associated with changing the number of labelled cells being imaged.

The signal intensity measurement method was previously used to assess labelled cells by Frank *et al.*[81] . The other commonly used method to assess labelled cells is the relaxivity method[128]. The signal intensity method is faster than the relaxivity method because it uses MR weighted images instead of maps which take longer to acquire[150]. The short acquisition time is more favourable *in vivo* studies with live subjects. However, the relaxivity method gives more

precise results[128,150]. Based on our application, we use relaxivity method for most of our *ex vivo* work and SI method for the live cells and subjects.

We used the SI measurements to assess the labelled cells *in vitro* and determine the amount of cells needed to be detected in MRI. The SI value decreased with increasing the number of iron-labelled cells, and the cells appeared as hypointense areas which indicate T_2 shortening effect. On the other hand, the increase of the Gado celltrack-labelled cells increased the SI value which indicates T_1 shortening. Given that the mentioned contrast agents changed the relaxation times, this means they could be used as effective T_2 and T_1 contrast agents.

The phantoms in which cells were directly injected into agar (phantom 1 & 2) were not appropriate for assessing the labelled cells and calculating their corresponding SI values. This was due to the formation of signal voids at the areas of cracks or bubbles at the site of cell injection. The formed signal voids overlapped the labelled cells and interfered with their visualization. This problem was solved in phantom 4 and 5 by containing the cells in small tubes first then immersing them into bigger ones that contain agarose to minimize imaging artefacts. The later two phantoms allowed the detection of the labelled cells and the determination of their corresponding SI measurement.

Both imaging sequences showed the labelled cells and allowed the SI measurement. However, the GE sequence was more sensitive to iron which made the cells more visually prominent due to the susceptibility artefacts associated with it. These findings are in agreement with a study comparing the visualization of labelled mesenchymal stem cell in a SE and GE sequence, where cells were detected in both sequences but each of them showed a different pattern of SI changes corresponding to iron labelling[81].

Our data show that cells labelled with Bangs and Ferex have strong effects on T_2 and T_2* while Gd-labelled cells changed T_1 relaxation time. Gado celltrack was less detectable than iron contrast agent and higher labelling doses or concentrations of cells were required to detect it in MRI. Also, we demonstrated that the developed label-differentiation protocol yielded cells that can be visualized in MRI *ex vivo* using SE or GE sequences. MRI was able to detect changes in SI associated with cell numbers as low as 20,000 Ferex-labelled cells. At the same time, the cells were healthy and could be used in tissue-engineering applications.

Prussian blue (PB) stain has been the gold standard histochemical stain for iron detection[71]. In our study, the uptake of iron based contrast agents was confirmed using PB stains. Counterstaining the PB stain with nuclear fast red gave additional information about the relation between the cells and the iron. It verified the presence of the label inside the cells. The Gd contrast agent did not have a specific histological stain which makes it difficult to confirm its uptake by the cells histologically. However, there are other methods to confirm cellular uptake of Gd such as energy-dispersive X-ray spectroscopy[151] or MR relaxometry[128]. In our study, we used Gd signal analysis to evaluate the Gd uptake by the ESCs.

Our results demonstrated that ESCs had auto-fluorescent properties; this agrees with Santin *et al.* results, where he showed that mouse ESCs, especially in the phases of differentiation, possess auto-fluorescent properties[152]. Thus, for accurate interpretation of the Bangs fluorescent results, the auto-fluorescent properties of ESCs should be carefully considered.

The use of the transfection agent, lipofectamine, assisted the uptake of contrast agents by the cells. The produced cells were viable and preserved their capacity to differentiate and proliferate. This result is in agreement with *Frank et al.* findings in which stem cells labelled with SPIO-transfection agent complex showed viability and proliferation capacity similar to that of

unlabelled cells[81,153]. There are other methods for transfecting the stem cells with contrast agents such as adding an antigen-specific internalizing monoclonal antibody to the surface of the contrast agent that can target specific cells which has the corresponding surface antigen[154]. The mentioned method requires the prior synthesis and preparation of the contrast agents, and the availability of the internalizing antibody which limits its use[154].

It is important to differentiate cells before implanting them *in vivo* to avoid tumor formation. Additionally, the collagen gel scaffold produced after the differentiations process provides the cells with the needed mechanical support to stay at the site of fracture[30]. The used differentiation protocol proved to direct the cells into osteogenic lineage[44] and we combined it with our optimized cell labeling protocol. However, combining the differentiation and the labelling protocol together was challenging. This was due to the formation of a strong extracellular matrix upon differentiation which prevents the labelling material from penetrating to the cells. Consequently, labelling the cells after differentiating them was unsuccessful. For this reason, we used the "Label then differentiate" protocol which could be applied in many tissue-engineering purposes without hindering the capacity of cells to proliferate or differentiate. The developed *ex vivo* cell labeling-differentiation protocol will be used in the subsequent stages of our project.

Our main aim was to develop an MRI protocol to monitor tissue engineered based therapies where new therapies could be tested and followed up non-invasively across a time course. Our results demonstrated that labelling of ESCs with Ferex, Bangs or Gado celltrack did not adversely affect their viability. Furthermore, Ferex cell labelling proved that Ferex did not compromise the cell's capacity to proliferate or differentiate. This shows that our developed cell label-differentiation protocol is effective and the cells can uptake the label without being adversely affected. Also, we developed a method for MR imaging and analysis of the labelled

dESCs *ex vivo* using SI measurement. In conclusion, this protocol could be applied in tissue-engineering purposes assuring the labelling will not adversely affect the treatment outcomes. Our next stage would be translating these findings to *in vivo* work.

Chapter Seven: **MR tracking of labelled embryonic stem cells in muscle**

7.1 Introduction

It could be challenging to visualize labelled cells *in vivo,* on a time course using MRI because it requires the optimization of a cell labelling and an MR imaging protocol[10]. Many studies have investigated MR cell tracking in various models such as myocardial infarction and the cardiovascular system[64,126,127], ischemia[155], neural transplant[69,75], and muscles[127]. However, to our knowledge, cell tracking in a bone model has not been investigated.

Although we previously developed an ESC labelling (chapter 6) and an MRI protocol (chapter 2), it remains to be seen whether these can be used together *in vivo* to image and to detect labelled ESCs. In this experiment we applied MR imaging parameters and cell labelling techniques we developed in previous *in vitro* work to an *in vivo* bone fracture model. The muscles were chosen in this preliminary set of experiments because they acted as a plain background for MR visualization of labelled cells[127], before moving to cell tracking in a bone fracture model. The same method was previously used to determine if labelled ESCs could be tracked in a myocardial infarction for further development of their therapeutic approach[126].

Different contrast agents have different properties. Iron-based agents are detected using sequences that are more sensitive to susceptibility artefacts[128]. These artefacts can be severe near bone, making cell tracking with iron a challenge in bone fracture[27]. Thus, we will use the spin-echo based sequence (RARE) that was studied in chapter 2, for imaging the mouse bone fracture model and we will combine it with a GE based sequence (FLASH) to benefit from its sensitivity to susceptibility artefacts that are caused by iron contrast agents[73].

The aim of this study is to qualitatively assess the ability of our labelling and imaging standardized protocol in enabling the MRI visualization of (Gd, Ferex and Bangs) labelled ESCs

injected into the muscles of mice, on a time course, as a preliminary step before moving to cell tracking in a bone fracture model.

7.2 Materials and methods

Cell culturing. ESCs were cultured and maintained in a pluripotent state as previously described in Section 6.1.1. Briefly, ESCs were cultured on gelatin coated plates or mouse embryonic fibroblasts and supplemented with cell culture media containing leukemia inhibitory factor. Cells were sub-cultured every other day.

Cell labelling. Three sets of ESCs were labelled with Ferex, Bangs or Gado cell track according to our standard labelling protocol described in Section 6.1.1. Briefly, two sets of ESCs were incubated with Ferex or Bangs at a concentration of 25 µg/mL plus lipofectamine for 24 hours, and then washed with PBS. For the third set, ESCs were incubated with Gado celltrack at a concentration of 0.08 mg/mL plus lipofectamine for 24 hours, and then washed with PBS. Then labelled ESCs were suspended in cell media to be injected into the mouse muscle. Undifferentiated cells were used in this study to be able to suspend them and inject them in the mice muscles as a proof of concept study for MRI visualization of cells *in vivo*.

Mice groups and cell injection. Two groups of mice were used in this set of experiments. In group one, 25 µl of suspended, undifferentiated ESCs (equivalent to 67,500 cells), labelled with 25 µg fe/mL Ferex were injected into the thigh muscle of the mouse (n=1). *In vivo* mouse thighs were imaged with MR at day 1 and 8 post injection.

In group 2 (n=3), Gado celltrack (0.08 mg Gd/mL), Bangs-or Ferex-labelled (25 µg fe/mL), undifferentiated ESCs were injected in the gastrocnemius muscle of each mouse (~3,400 cells). Mice were imaged at day 1 and 7 post injection.

MR imaging. A 9.4T Bruker Avance system and a slotted tube resonator coil were used for imaging. Mice were anaesthetized with isoflurane. Mice with Bangs-and Ferex-labelled cells were imaged with a RARE T_2w sequence using the following parameters: TR/TE=2000/20 ms, RARE factor=4, FOV=2.5 x 2.5 cm, matrix= 256 x 256, slice thickness= 0.5 mm, and acquisition time=19 min. Mice with Gado celltrack-labelled cells were imaged with a RARE T_1w sequence with the following parameters: TR/TE=500/7.5 ms, RARE factor=4, FOV=2.5 x 2.5 cm, matrix= 256 x 256, slice thickness=1 mm, and acquisition time=8 min. All mice were also imaged with a FLASH sequence using the following parameters: TR/TE = 125/4 ms, flip angle 30º, FOV= 2.5 x 2.5 cm, matrix=256 x 256, slice thickness=1 mm to verify the location of iron. Between scans, mice were housed in the half way house facility under standard conditions. After 7 or 8 days, all mice were rescanned.

7.3 Results

Group 1. ESCs labelled with Ferex were detected as a dark, hypointense area *in vivo* (Figure 7-1A). At day 1post-injection, the iron remained largely in the area of injection. Due to the susceptibility artefacts caused by iron in the FLASH sequence, the cells appeared as a bloom which is a typical appearance of iron in GE sequences. The bloom artefact meant that the anatomy of the tissues adjacent to the iron could not be clearly visualized in the FLASH image (Figure 7-1 A). Conversely, the SE-based RARE T2w sequence showed the anatomy of the bone, muscles, bone marrow and periosteum clearly. However, the iron-labelled cells were less detectable in this sequence (Figure 7-1 B). At day 8, the Ferex-labelled ESCs could not be detected at the site of injection (Figure 7-1 C).

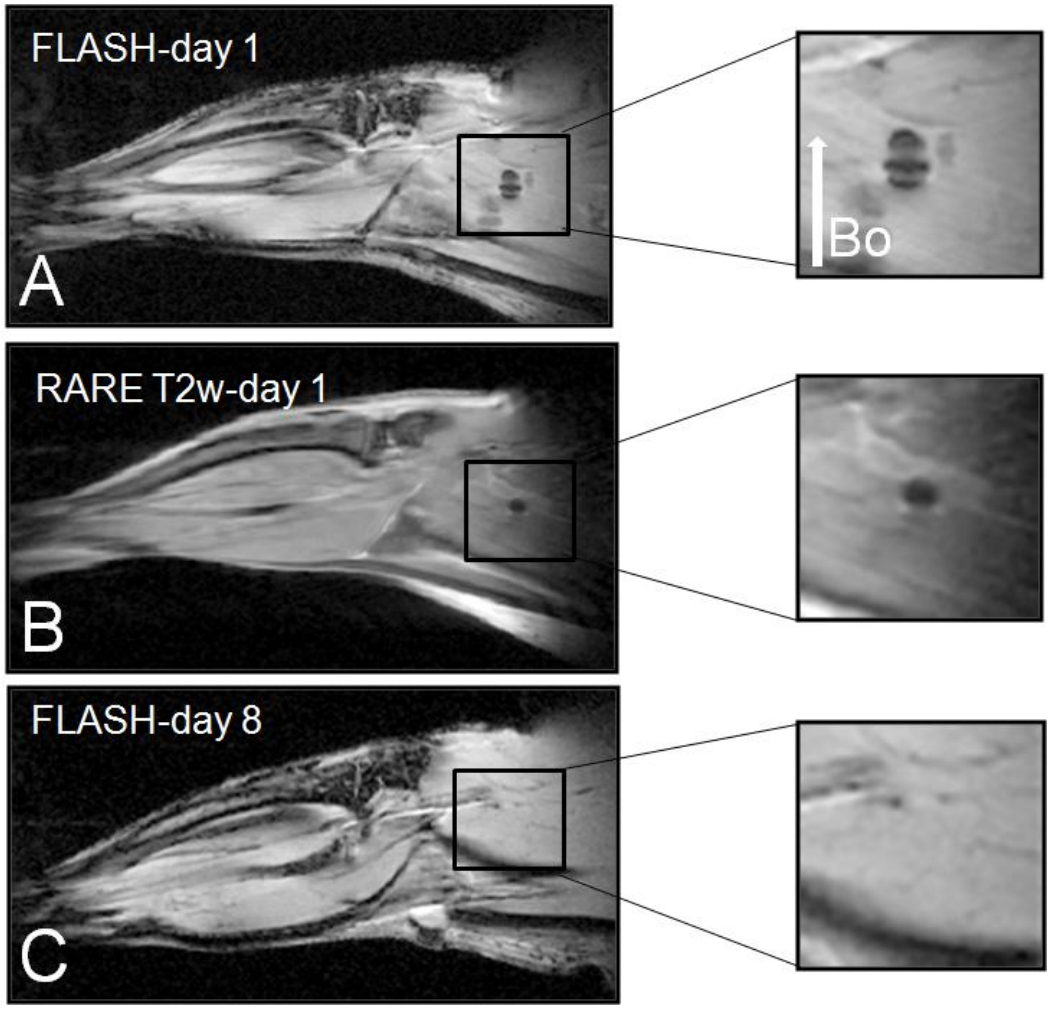

Figure 7-1 MR images of labelled ESCs transplanted into the thigh of a mouse. A. FLASH at day 1 post-injection, B. RARE T_2w image at 1 day post-injection. C. FLASH image 8 days post-injection. Arrow indicates the direction of B_0.

Group 2. Bangs- and Ferex-labelled cells were detected as a hypointense region in RARE T_2w and FLASH images. At day 1 post-injection, the Bangs-labelled cells were more prominent in the MRI than Ferex. The Gado celltrack-labelled cells were only detected in a cross sectional view of the mouse leg in a RARE T_1 w image. They were not detected in other views or sequences. At day 7 post injection, Bangs-labelled ESCs appeared as a localized hypointense

area and the Ferex-labelled ESCs appeared as a diffuse hypointense area. In both of them, the size of the hypointense area decreased. Seven days post-injection, the Gado celltrack-labelled cells were undetectable in either MRI sequence (Figure 7-2).

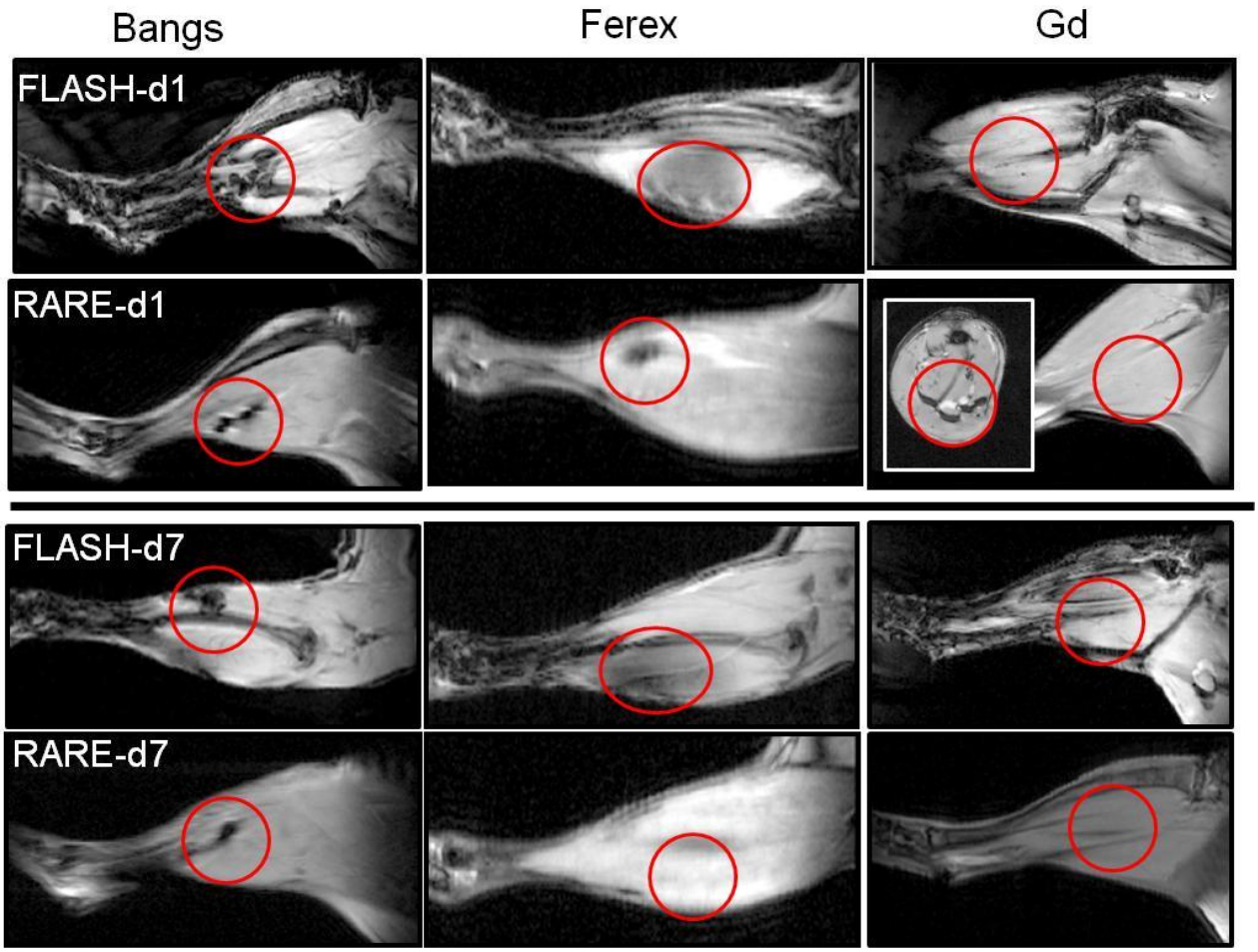

Figure 7-2 RARE and FLASH MRIs of labelled ESCs in the thigh of the mice at day 1 and 7 post injection. The Bangs- and Ferex-labelled cells were detected in both MRI sequences at both time points. At day 7, the size of the hypointense area decreased. The Gado celltrack-labelled cells could only be detected in a cross section at day 1 (as shown in the inset).

7.4 Discussion

The RARE sequence detected the iron-labelled cells *in vivo* (Bangs and Ferex), at day 1 post injection. It also revealed the anatomy of the bone and muscles with minimal artefacts. The FLASH sequence was more sensitive to iron and its effect on magnetic field homogeneity. This is because GE-based sequences are affected by magnetic field inhomogeneities and do not have a mechanism to compensate for them[48]. At day 8 post injections, the iron-labelled cells were less detectedable. This could be due to dilution of the label caused by cell migration, death or proliferation. Cell migration was previously suggested by Cahill in a study tracking iron-labelled cells in muscles[156]. Additionally, label dilution proved to be a major limitation in MRI tracking of iron-labelled cells across time[67].

The Bangs-labelled cells were more prominent in the MRI than Ferex-labelled cells. This could be attributed to the large size of the Bangs particles (0.9 μm) compared to the Ferex particles (50-150 nm). This was similar to Hinds *et al.* findings, where he proved that using larger sized iron particle creates more magnetic momentum within the labelled cell than the magnetic moment created around cells labelled with conventional nano-sized iron particles[135]. Consequently, Bangs-labelled cells more detectible in MRI than Ferex-labelled cells.

Iron-based contrast agents have superparamagnetic properties[48]. This generates susceptibility effects around cells that are labelled with iron-based contrast agents and makes the cells appear larger than their actual size. This is a drawback for the FLASH sequence because it decreases the accuracy of cell quantification using the FLASH sequence. However, this made iron-labelled cells easier to detect using the FLASH sequence compared to using the RARE sequence. The FLASH sequence suffered from artefacts at the interfaces between the different tissues due to the field inhomogeneity problem. Therefore, using both sequences to image iron-

labelled cells would have the benefit of showing the anatomy of the MSK system and the iron-labelled cells clearly. This agrees with Riviere *et al.* study, where GE sequence was better at detecting signal intensity loss areas of iron-labelled cells than SE sequence[127].

The detection of the Gd-labelled cells *in vivo* was challenging in both MRI sequences, at both time points. This could be due to the paramagnetic properties of Gd which makes it less sensitive to MR magnetism than iron-based contrast agents[48]. Also, the magnetic nature of the Gd makes its T_1 effect confined to a very small area not much larger than the Gd complex[48]. Consequently, Gd-labelled cells were less detectable in MRI than Ferex-labelled cells. Thus, we suggest increasing the number of Gd-labelled transplanted cells to improve their *in vivo* MRI visualization.

Our findings from this chapter show that it is possible to label and visualize ESCs *in vivo* using MRI. In this study, we used the plain background of muscle to establish that the labelled ESCs were visible. The next task is to determine whether the labelled cells are also visible inside the bone fracture.

Chapter Eight: **MR tracking of embryonic stem cells in bone fracture model**

A cell labelling protocol was already established in chapter 6 and the cells were imaged *in vitro* (chapter 6) and *in vivo* in mice muscle (chapter 7) as a proof of concept. The focus of this chapter is to use 9.4T MRI to study the cell trafficking of labelled, transplanted embryonic stem cells (ESCs) in an *in vivo* mouse bone fracture model. This chapter includes two studies to develop and further investigate cell tracking in bone using MRI and followed by immunohistochemistry (IHC) to learn about the behaviour and fate of cells and iron.

8.1 Introduction

Cellular therapies have great potential in healing bone fractures[30,157]. However, the behaviour and the fate of the cells, once injected, are not fully understood[158]. Until cellular fate is determined, the use of these therapies *in vivo* is limited. A non-invasive cell tracking method is needed to study cellular therapies and their possible outcomes. MRI cell tracking is rapidly evolving due to its potential applications in this field[10]. It has been previously used to track labelled cells *in vivo* in different soft tissues such as the heart[63,64], lymph nodes and the brain[10]. However, to our knowledge no studies investigated tracking labelled cells in bone injuries. Two studies attempted to synthesize implants with labelled osteogenic cells and imaged them *in vitro*[159] and subcutaneously[160], yet no studies have visualized labelled cells *in vivo* inside bone.

One hurdle that must be overcome in MR cell tracking is interpreting signal intensity (SI) changes linked to the labelled implanted cells *in vivo* because similar SI changes could be reflecting different phenomena. Give that, we standardized the MR imaging conditions for all our experiments; we assume that the SI changes obtained reflect the changes in the tissue relaxation times caused by the contrast agents or changes in the proton concentration caused by the bleeding at the site of bone fracture. Thus, similar SI changes could be obtained from dead or

alive cells as long as they both carry iron. Additionally, Berman *et al.* showed that dead cells that had their labelled transferred to phagocytic cells can produce more SI changes and lower the signal intensity more than live labelled cells that proliferated and subsequently had their label diluted[74]. Thus, care should be taken when interpreting the SI changes associated with MR labelled cell tracking due to its complexity[74]. Despite all this, the SI measurement is commonly used method in the quantitative assessment of iron or Gd content *in vivo*[123,128,133,150,161] as well as in cell tracking purposes[130].

In this context, iron oxide and Gd contrast agents have different mechanisms for changing the SI and generating contrast in an MR image[125]. Iron-based agents have a T_2 shortening effects in T_2 weighted images which decrease signal intensity and appears as a dark area[129]. In contrast, Gd contrast agents have a T_1 shortening effects in T_1 weighted images which increases the signal intensity and appears as a bright area[110]. Iron oxide and Gd also differ in their sizes; Gd agents are usually nanometer-sized while iron particles ranges from nanometer-to micrometer sized particles. Hinds *et al.* showed that the size of the contrast agent can impact the amount of signal changes produced[135], he was able to obtain higher SI changes when he imaged micron-sized Bangs particles compared to nano-sized iron particles[135]. Gd contrast agents pools in the extracellular space after cell death, then they get rapidly eliminated through the kidney due to their low molecular weight[158]. This makes it is less likely for Gd compounds to get endocytosed by other cells[158]. In contrast, iron oxide contrast agents have high molecular weight which makes them a target for phagocytic cells. This means that after death of the labelled transplanted cells the iron gets transferred to phagocytic cells which gives false positive results[156,158]. Despite the complexity of interpretation of the SI changes associated with iron oxide labelled cells, still iron oxides are more favourable than Gd compounds due to their higher relaxivity and detection

sensitivity[158]. In this chapter we mainly used Ferex-labelled cells, but also tried Gd-labelled cells in a small number of animals to confirm cell distribution results from the iron labelled cells.

Commonly, the fate of cellular therapy could result in one or in some combination of the three following outcomes 1) the cells integrate in the host tissue, proliferate, and become part of it[158], 2) the cells die due to immunologic rejection[74], 3) the cells migrate to other locations[67,162]. To improve our understanding of SI data about the fate of the cells, we correlated it with the IHC and histology data. A similar protocol has been previously used to study the fate of labelled myoblast[3] and neural[9] implanted cells and correlated the IHC data with the MRI data.

To determine how cells needed to be introduced into mouse bone injuries we did a pilot study to test implanting undifferentiated cells without the scaffold in the bone fracture. Also, we tried a 3D collagen differentiation protocol that differentiate the cells and provide them with the needed mechanical support to stay at the site of fracture. An advantage of using the 3D collagen differentiation protocol is that it eliminates the possibility of tumour formation *in vivo*[30]. It also directs the cells into an osteogenic lineage which will provide the bone fracture with needed cells such as osteoblasts[44].

*Two studies were performed in this chapter***. Study 1, development of tracking**, was used to test undifferentiated ESCs as well as different contrast agents (Bangs, Ferex and Gado celltrack). We used one pilot mouse to test transplanting undifferentiated ESCs suspended in media in a bone fracture model but found that it was important to differentiate the cells first. In 7 more mice, we compared the potential use of three contrast agents (Bangs, Ferex and Gado celltrack) in tracking dESCs cells in bone fracture. In order to verify that iron was within cells, we stained for iron and used the IHC Y-chromosome protocol to detect the transplanted cells in the host tissue (we transplanted male ESCs in female mice).

In Study 2, cell tracking using Ferex, we focused on Ferex as it was the contrast deemed most useful in study 1. We used dESCs which was deemed more successful based on study 1. We undertook what I consider to be the key experiment of the thesis, that of tracking and determining the fate, of these cells in a bone fracture model. The ESCs used in this study were transfected with green fluorescent protein (GFP) gene, and IHC staining for GFP was performed to identify the implanted cells in the host tissue. Additionally, macrophage staining was done to determine if the label transferred from the implanted cells to macrophages. In both studies (1 & 2) the fractures were made at the same locations in the mid shaft of the mouse tibia to ensure a consistent healing pattern.

In this chapter we tried to address the pitfalls associated with using SI changes to identify labelled cells in a bone fracture model by studying the fate of the implanted cells and final distribution of contrast agents.

8.2 Materials and Methods

8.2.1 Study 1, development of tracking, Protocol

We used one pilot mouse to test the possibility of transplanting undifferentiated ESCs suspended in media in a bone fracture model. The rest of the mice used in this study received dESCs in collagen constructs. Beside the pilot mouse, three groups of mice (n=7) were used to test the possibility of tracking labelled dESCs in the bone fracture model. The groups were divided based on the contrast agent used for cell labelling (Bangs, Ferex and Gado celltrack) (Figure 8-1). Two holes were drilled in the tibiae of each mouse, one received labelled dESCs in collagen construct and the second was left empty as control. Mice were imaged with MRI at day 1, 7 and 14 post surgeries. Signal intensity analysis (SI) was done to analyze the MRI data. Y-

chromosome and Prussian blue (PB) staining were used to verify the MRI data and study the behaviour and the fate of the transplanted cells and iron.

The results of this study showed that transplanting undifferentiated labelled cells was not applicable in the bone fracture model, and only dESCs in collagen constructs can stay at the site of implantation. The results also showed that Ferex-labelled cells could be tracked *in vivo* using MRI, plus it answered some questions about the behaviour of the cells *in vivo* (migration-integration in host tissue). However, it did not determine whether the iron transferred to macrophages which might have affected the MRI results. Thus, further investigations with bigger number of mice were needed to confirm the results and to determine whether the iron transfers to macrophages after cell death.

8.2.2 Study 2, tracking of Ferex-labelled cells, Protocol

Based on the results of Study 1, we decided to focus on Ferex for cell labelling and the dESCs (in collagen construct) as the cell therapy of choice. The ESCs were also transfected with GFP gene to become traceable in the host tissue with IHC. Bigger number of mice (n=10) was used in this study (Figure 8-1). Two holes were drilled in the tibiae of each mouse, one received Ferex-labelled dESCs in collagen construct and the second was left empty as control. Mice were imaged with MRI at day 1, 7 and 14 post surgeries. SI measurements were done to analyze the MR images. GFP, macrophage and PB staining were used to verify the MRI data and determine whether the iron transferred to macrophages.

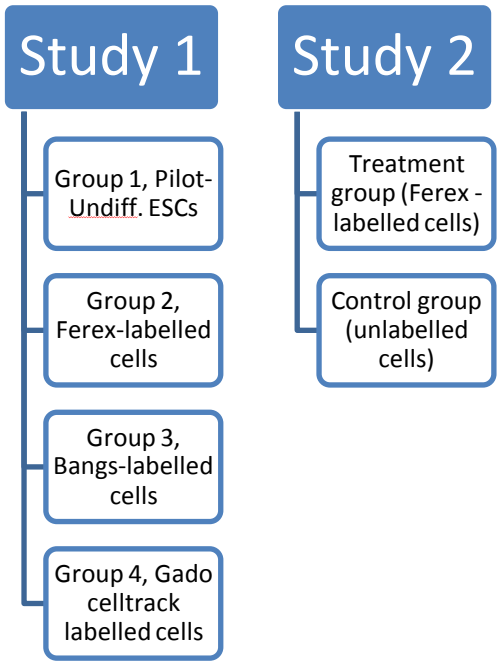

Figure 8-1 The animal experimental design of the two studies performed in this chapter.

8.2.3 ESCs culture, label, GFP transfection and differentiation.

ESCs culturing. ESCs were cultured and maintained in a pluripotent state as previously described in Section 6.2. Briefly, ESCs were cultured on gelatin coated plates or mouse embryonic fibroblasts and supplemented with cell culture media containing leukemia inhibitory factor. Cells were sub-cultured every other day.

ESCs labelling. Three sets of ESCs were labelled with Ferex, Bangs or Gado cell track according to our standard labelling protocol described in Section 6.2. Briefly, two sets of ESCs were incubated with Ferex or Bangs at a concentration of 25 µg/mL plus lipofectamine for 24 hours, and then washed with PBS. For the third set, ESCs were incubated with Gado celltrack at a concentration of 0.08 mg/mL plus lipofectamine for 24 hours, and then washed with PBS.

GFP transfection of ESCs (for use in Study 2). At 70 % confluency of ESCs, they were transfected with 5 µl of GFP lentivirus (generously given by Dr. Roman Krawetz) and 2 µl of the

transfection agent polybrene (Sigma) and incubated for 12 hours at 37ºC. Cells were checked under a fluorescent microscope to confirm transfection and expression of the GFP, and then washed with PBS. Viability of Ferex-labelled GFP-ESCs was confirmed before implanting them in bone (94%).

ESCs differentiation (for Study 1-Group2- 4 and Study 2). ESCs were differentiated into the osteogenic lineage in 3D collagen constructs[44], as described in Section 6.2. Briefly, to differentiate the ESCs, bovine collagen 1 (Advanced Biomatrix) was polymerized into a two-dimensional gel using 10mM beta-glycerol phosphate (BGP). Specifically 80% v/v 3 mg/mL collagen 1 solution was mixed with a single cell suspension (1 million cells/mL) and 20 % v/v BGP dissolved in 5X concentrated DMEM. The 5X concentrated DMEM was generated by dissolving powered DMEM (Invitrogen) in 1/5 the recommended amount of water and supplemented with 15 % FBS (Invitrogen), 1 % non-essential amino acids, 50 U/mL penicillin and 50 µg/mL Streptomycin, and 0.1 mM β-mercaptoethanol.

8.2.4 Preparation of the bone fracture and in vivo implantation of the cells.

For Study 1. Eight female 129 Sv mice (6 weeks old; Jackson laboratories) were used in this study. They were strain matched to the ESCs used in this study. Male ESCs were implanted into female hosts to identify the transplanted cells in the host tissue using the Y-chromosome IHC protocol[30].

To create the bur-hole fracture, all 8 mice were anesthetized with isoflurane, and then were given buprenorphine (0.03 mL) and penicillin (0.01 mL) intraperitoneally prophylactically as analgesic and antibiotics, respectively. The applied surgical technique is a modified technique from Taiani *et al.*[30]. Surgery was performed unilaterally. Hind legs were shaved and draped in a sterile fashion, and then a skin incision was made over the medial aspect of the proximal end of

the tibia. Soft tissue was pushed away to expose bone. A dental drill was used to drill two 0.5-0.7 mm holes in the cortical bone of the tibial shaft. The distance between the tuberosity and the hole was 3mm and the distance between the two holes was 3 mm. The mice were divided into four groups. The first group (n=1) was a pilot experiment to test the procedure of implanting undifferentiated ESCs (suspended in culture media) in the bone fracture model. Ferex-labelled undifferentiated ESCs (cell density ~2 x 10^5 cells/mL) suspended in culture media were injected in the distal hole using a Hamilton syringe. Groups 2-4 were divided according to the labelling material used, and all used dESCs in collagen constructs as the implant. Group 2 (n=2) had Ferex-labelled cells, Group 3 (n=2) had Bangs-labelled cells. Group 4 (n=3) had Gd-labelled cells. Approximately one-fifth of the 1 mL gel construct (~20 x 10^4 cells) were picked up from the culture dish using a scalpel blade, and gently implanted inside the distal hole. A needle was used to gently push the cell-gel construct into the drilled hole. The skin was sutured closed and mice were returned back to their cages.

For Study 2. 10 female Sv/129 mice (6 weeks old, Charles River laboratories) were used in this experiment and the same standard surgical procedure was applied to all mice. The treatment group (n=8 mice) had Ferex-labelled GFP-dESCs implanted in the distal hole. The proximal hole was left empty. The control group (n=2 mice) had unlabelled GFP-dESCs implanted in the distal hole. As with the treatment group, with the proximal hole was left empty. Two mice from the treatment group were euthanized at 1 day post surgery and 8 mice were euthanized at day 14 post surgery.

8.2.5 In vivo MRI imaging.

Mice were anesthetized and imaged at day 1, 7 and 14 post-surgery. Mice with Bangs- or Ferex-labelled cells were imaged with a RARE T_2w sequence using the following parameters:

TR/TE=2000/20ms, Rare Factor=4, Matrix=256 x 256, Slice=0.5 mm, Resolution=100 x100 x500 µm. Mice with Gado celltrack-labelled cells were imaged with RARE T_1w sequence with the following parameters: TR/TE=500/7.5 ms, RARE factor=4, FOV=2.5 x 2.5 cm, matrix= 256 x 256, slice thickness=1 mm, and acquisition time=8 min.

8.2.6 In vivo µCT (done in Study 1).

µCT was used to verify the location of bone injuries in the MRI. The tibiae of mice from group 2-4 were excised, fixed, and then scanned with a Viva CT machine with 11.4 mm tube. The x-ray source had an energy level of 55 kVp, a current of 144 µA and an integration time of 400 ms. The imaging resolution was 12 µm isotropic, 1024 x 1024 matrix, FOV 12mm 12µ, and 500 projection/180 degrees. After the experiment was done, mice were euthanized using euthanyl (Bimeda-MTC, Cambridge, ON).

8.2.7 Histology

Prussian blue staining for iron. Cells in collagen constructs (Ferex-GFP-, Ferex-, Bangs- and Gado celltrack-labelled ESCs) were stained with PB to confirm the uptake of iron by the cells before implanting them *in vivo*. Also, the excised tibiae of mice from Study 1 and Study 2 were stained with PB as described previously in Section 6.2. Briefly, tissues were fixed, embedded in paraffin blocks, sectioned, and prepared for staining. For the PB staining, the iron was released by denaturing the binding proteins with 20% hydrochloric acid, followed by treatment with 10% potassium ferrocyanide to form a blue pigment of potassium ferric ferrocyanide.

H & E stain. For mice, tibiae were fixed in 10% neutral buffered fromaldehye (NBF) (Sigma Aldrich, USA), 10% ethylene-diamine tetra acetic acid (EDTA)[163]. The EDTA solution was changed daily for the first 7 days, then every 2 days for 7 more days. Then, samples were washed

every hour using distilled water and soaked in between washes, this was repeated 5 times. After that, samples were put in an automatic bone processor in gradually increasing concentrations of alcohol overnight (80%, 98% and 100%), followed by xylene for clearing of the samples. Then, they were embedded in paraffin blocks. For sectioning, we cut 10 µm sections deparaffinised and hydrated in gradual dilutions of ethanol. Two stains were used. The first was hematoxylin Gills III stain (VWR, Canada) and Harleco eosin Y solution (1% alcohol) (H & E) (EMD chemicals Inc. NJ), which was used to reveal the implanted tissue construct at the site of bone fracture, and the surrounding tissue. The second was PB staining, which was used to confirm the presence of iron (explained in details in Section 6.2). After staining, slides were rinsed twice in distilled water, dehydrated using alcohol, and cleared with xylene. Cover slips were mounted on them using a mounting media. An Olympus microscope was used to acquire the histology images.

Fluorescent microscopy. Mice from Study 1-Group 3 (Bangs-labelled cells) were examined under fluorescent microscope using TxRed filter. It was also examined under brightfield illumination to visualize iron.

For Study 2 (Ferex-labelled GFP-ESCs), fluorescent GFP cells were examined under fluorescent microscope using a FITC filter to cover the excitation range of 475-495 nm and emission range of 520-560 nm.

8.2.8 Immunohistochemistry.

For all immunohistochemistry work, the slides were deparaffinized in two changes of xylene (10 minutes each), followed by rehydration in gradual dilutions of ethanol and washing in distilled water.

Y-chromosome in situ hybridization (for Study 1). We used this protocol to investigate *in vivo* cell migration and compare their location with the distribution of iron from the PB stained

sections to determine. We chose Group 2 because it will allow us to detect the iron label in the tissues by using the PB stain.

The male ESCs implanted in female mice were identified using Y-chromosome *in situ* hybridization staining[30]. Briefly, the tissues were sectioned at 5 µm. For antigen retrieval, the sections were pretreated, with 2x saline sodium citrate (SSC) at 70º for 30 minutes, and then allowed to cool at room temperature for 5 minutes. Then, the sections were washed twice for 5 minutes in distilled water. To break protein cross linking, sections were covered with a mix of pepsin 0.5% and 0.05M HCL for 10 minutes at room temperature, then rinsed twice with distilled water (3 minutes each). After that, they were dehydrated by placing them for 5 minutes in each of 4 gradually increasing concentrations of ethanol (70%, 80%, 95%, and 100%), then left to dry for 20 minutes at room temperature. To denature the sections, they were covered with 70% formamide/30% 2x SSC for 10 minutes at 60ºC, and then quenched in ice-cold 70% ethanol for 4 minutes. Then, the sections were dehydrated again in gradually increasing concentrations of ethanol (70%, 80%, 95%, and 100%) and left to dry at room temperature for 20 minutes. We used biotinylated mouse Y-chromosome (Cambio 1187-YMB-01) as a probe. It was denatured at 65º for 10 minutes, and then 10 µL of the denatured probe were applied to each slide and incubated in a humidity chamber at 37º for 18 hours. After that, sections were washed with 2x SSC for 5 minutes, followed by two 5-minute washes with 50% formamide/2x SSC, then two 5-minute washes with 1x SSC, and two 5-minute washes with 0.4xSSC/0.3%NP-40 buffer. Finally, sections were rinsed with three 3-minute washes of distilled water. To prevent non-specific binding, sections were first treated with 3% H_2O_2/Methanol for 15 minutes and rinsed with PBS and then treated with the blocking reagent (10% goat serum/1% bovine serum albumin/PBS). Detection was achieved by using horse radish peroxidise (HRP)-labelled strepavidine

(Invitrogen, Ontario, Canada) for 30 minutes at room temperature. Then slides were counter-stained with hematoxylin and mounted with a mounting medium. To verify the specificity of the protocol, three controls were used: a male mouse tibia as a positive control, a female mouse tibia with no implanted cells as a negative control, and a male mouse tibia with all the steps applied except the Y-chromosome probe to control for non-specific binding of the HRP detection system.

We stained histological controls to verify the specificity of the protocol. The first control (negative) which was a female bone with probe and detection system, absence of Y-chromosome cells was noted which indicates that our detection system is specific and did not bind to non-specific sites (Figure 8-2 A). In the second control (positive) which was a male bone with probe and detection system, Y-chromosome positive cells was noted as cells with black-brown spot in their nuclei, which indicates that the Y-chromosome protocol successfully detected the male cells (Figure 8-2 B).

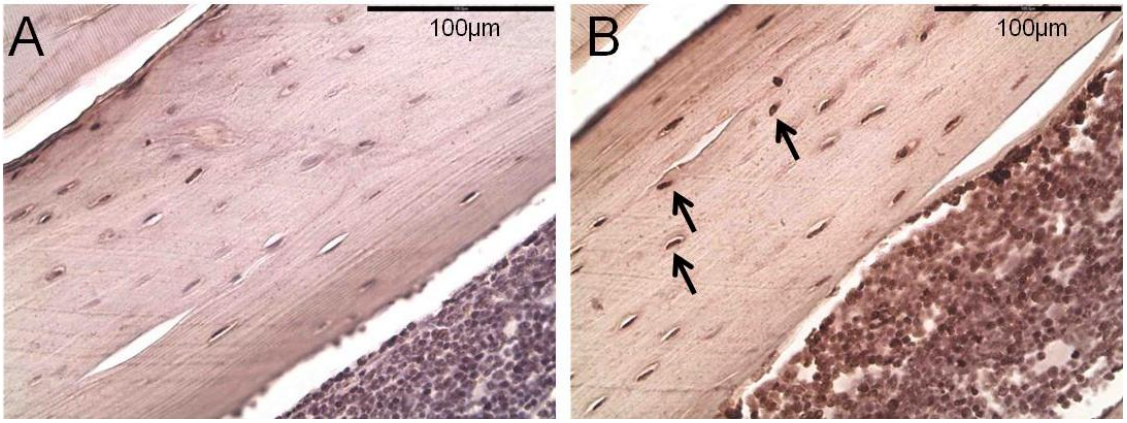

Figure 8-2 *In situ* hybridization for Y-chromosome (HRP/DAB detection counterstained with hematoxylin). Cells tested positive for Y-chromosome have black brown spot in their nuclei. (A) Female bone with probe and detection system. (B) Male bone with probe and detection system.

Macrophage staining (for Study 2). We used this protocol to stain for macrophages and compare their location with the distribution of iron from the PB stained sections to determine whether iron was transferred to macrophages after cell death. If both are found at the same locations this would suggest cell death and subsequent transfer of iron to macrophages.

We used a biotin-conjugated monoclonal anti-F4/80 (eBiosciences) to detect the F4/80 antigen which is expressed by macrophages and is considered the best marker to detect them[164]. We used liver tissue as a control because F4/80 is expressed in liver Kupffer cells. Deparaffinized slides were incubated with 20 µg/mL proteinase K (Invitrogen) for 15 minutes at 37º C, then washed 3 times in 1x PBS for 5 minutes each. Then slides were incubated with 0.3% H_2O_2/methanol solution for 20 minutes at room temperature, to quench the endogenous peroxidise, followed by three 5-minute washes in PBS. For blocking, we used 1% bovine serum albumin/10% goat serum/PBS for one hour in a humidity chamber at room temperature. To block endogenous biotin, first the slides were incubated in 10% (w/v) egg mix (Sigma) in water for 15 minutes at room temperature. Slides were then rinsed with water followed by PBS to remove all egg residues. Second, slides were incubated with a 5% milk solution for 15 minutes at room temperature. Then the slides were rinsed in water for 5 minutes and 0.1% PBS-Tween solution was added for 5 minutes. To stain for macrophages, slides were incubated with the primary antibody, diluted 1:100 in 1.5% goat serum in PBS for 30 minutes at 37º C. Slides were washed 3 times in PBS-Tween for 5 minutes each, then incubated them with horse radish peroxidise-streptavidine (Invitrogen) diluted 1:500 in PBS-Tween for 30 minutes at room temperature. The slides were washed again in PBS-Tween for 3 times, for 3 minutes each. 3,3'-Diaminobenzidine (DAB; Invitrogen) was applied for 5 minutes, then slides were washed twice for 5 minutes with distilled water twice. Slides were counterstained with a 1:2 hematoxylin

dilution for 20 seconds, and then dehydrated in gradually increasing concentrations of ethanol. Slides were cleared twice for 5 minutes each in xylene, then mounted with a mounting medium.

To verify the specificity of the macrophage protocol, we stained histological control sections of liver tissue. Absence of macrophages was noted in sections stained with the detection system but without the F4/80 antibody (Figure 8-3 A). Macrophage positive cells detected as brown spots were observed in sections stained with detection system and F4/80 antibody (Figure 8-3 B).

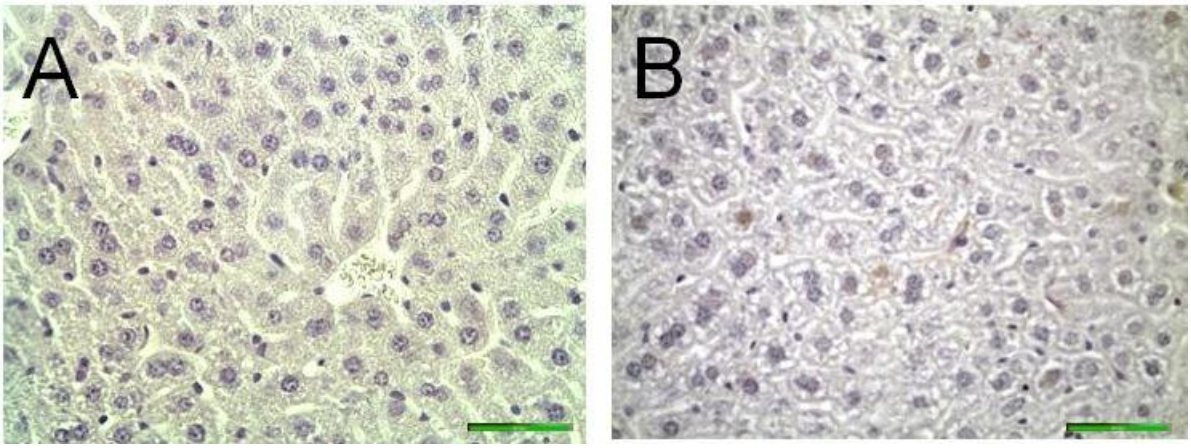

Figure 8-3 Liver sections stained with macrophage IHC staining (HRP/DAB detection counterstained with hematoxylin). Macrophages are detected as brown areas. (A) Liver sections with detection system but without F4/80 antibody, stained negative to macrophages. (B) Liver sections with F4/80 antibody and detection system show the presence of brown macrophages. Scale bar 50 µm.

GFP staining (Study 2). We used this protocol to locate GFP cells and compare their location with the distribution of iron from the PB stained sections to determine whether iron was still inside the transplanted cells. If both are found at the same locations this would suggest that iron is still inside the transplanted cells.

Goat polyclonal biotinylated GFP antibody (Abcam) was used immunohistochemistry. Deparaffinized, rehydrated slides were incubated with 20 µg/mL of proteinase K for 45 minutes at 37ºC, and then washed in distilled water three times for 5 minutes each. To quench the endogenous peroxidise, the slides were incubated with 3% H_2O_2/methanol for 20 minutes at room temperature. Slides were washed with 1xPBS three times for 5 minutes each. To block unspecific binding, 10% goat serum/1% bovine serum albumin/ PBS was applied at room temperature for 1 hour. The serum block was washed with two 3-minute PBS rinses. Slides were incubated with the primary antibody at a 1:100 dilution in 1.5% goat serum in PBS, in a humidity chamber over night at room temperature. Slides were given three 15-minute washes with PBS. Then slides were incubated for 30 minutes at room temperature with horse radish peroxidise-streptavidine (Invitrogen) diluted 1:200 in PBS. Then slides were washed in PBS-Tween three times, for 3 minutes each. 3,3'-Diaminobenzidine (DAB; Invitrogen) was applied for 10 minutes at room temperature. Slides were washed in running tap water then counterstained with hematoxylin (1:2 dilution) for 5 seconds. A final wash in running tap water was followed by dehydration in ethanol, clearing in xylene then mounting.

To verify the specificity of the GFP protocol, we stained histological control sections of a GFP transgenic mouse bone. Absence of GFP was noted in sections stained with the detection system but without the GFP antibody (Figure 8-4 A). GFP positive results were obtained in sections stained with detection system and GFP antibody (Figure 8-4 B).

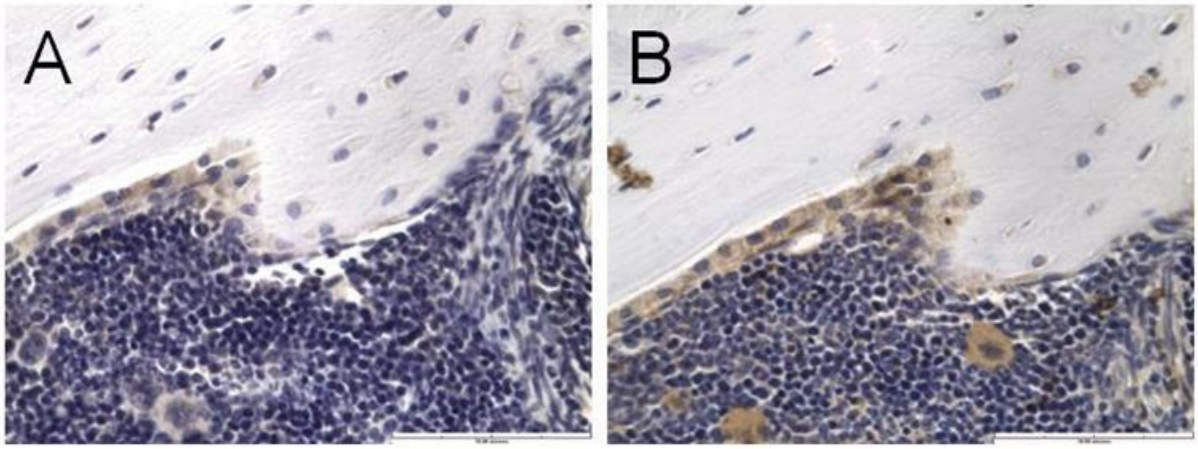

Figure 8-4 GFP stained bone sections of a GFP transgenic mouse (HRP/DAB detection counterstained with hematoxylin). GFP is detected as brown areas. (A) Bone with GFP antibody and detection system, presented GFP negative results. (B) Bone with probe and detection system, presented GFP positive results.

8.2.9 Image analysis and statistics.

We used SI ratios of the regions of interest (ROI) to the gastrocnemius muscle instead of the absolute SI values to assure accuracy when comparing mice between groups. Fixed number of pixels was used for all ROIs (~50 pixels). SI measurements were done using Marevisi software and graphs were created using GraphPad prism and Sigma plot software. The SI ratios of the distal hole of treatment group and distal hole of control group were compared at the three time points used (Day 1, 7 and 14 post surgery). The tests were run using GraphPad software, where statistics was considered significantly different when $P < 0.05$.

8.3 Results

8.3.1 Results of Study 1, development of tracking

8.3.1.1 *In vivo* MR imaging analysis and SI ratios data.

Group 1 (implanted with Ferex–labelled, undifferentiated ESCs). Cells flowed away from the site of fracture after the injection, likely as a result of being suspended in culture media. That labelled cells were absent from the site of injection was confirmed by the SI ratio measurements; at day 1 there was no difference in SI ratios between the distal hole and the proximal (Figure 8-5).

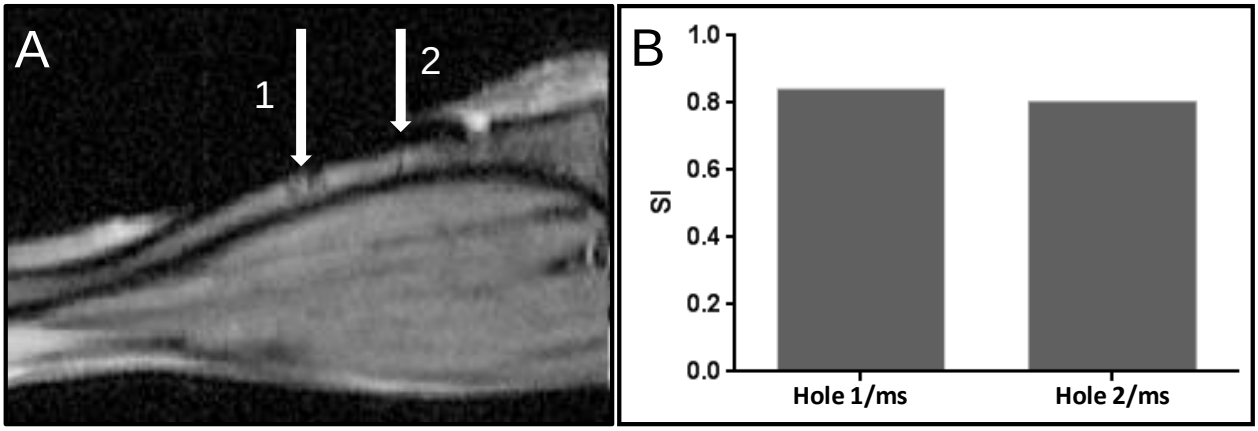

Figure 8-5 (A) A RARE T_2 weighted MR image of a mouse tibia with two drilled holes at day 1. (1) Distal hole injected at day 0 with Ferex-labelled ESCs suspended in culture media. (2) Proximal hole left empty as a control. (B) SI ratios of the distal and proximal holes to the gastrocnemius muscle (ms). SI ratio was similar at both holes which suggests absence of labelled ESCs.

Group 2, 3 and 4, implanted with labelled dESCs in gel construct. The reproducibility of the fracture location was evaluated (n=6). The mean distance between the top of the epiphysis to the centre of the first hole was 3.9 ± 0.26 mm, while the mean distance between the top of the epiphysis to the centre of the second hole was 6.8 ± 0.23 mm.

In Group 2 (n=2), at all time points, the distal hole, implanted with Ferex-labelled dESCs, appeared visually darker than the proximal hole that was not implanted with cells. This was

confirmed with the SI measurement where the mean SI at the distal hole appeared to be lower than the mean SI at the proximal hole (Figure 8-6 D).

We also observed that the SI ratio at each hole changed across time. At the distal hole the SI increased across time, at the proximal hole the SI decreased with time, and finally the SI of the BM decreased with time (Figure 8-6 A, B, C & D). This suggests that iron distributed from the distal hole to the BM and proximal hole across time which resulted in decreasing their SI as shown in the graph Figure 8-6 D. This suggests that the implanted labelled cells migrated from the distal hole to the proximal hole and the bone marrow.

In Group 3 (n=2), the distal hole, implanted with Bang-labelled dESCs, in one mouse the injuries could not be detected at day 1, but were clearly visible at day 7 and 14 (Figure 8-6 E, F & G). The SI analysis indicated a decrease of SI at the distal hole, proximal hole and BM (Figure 8-6 H). In the second mouse, no injuries were detected at any time points.

In Group 4 (n=3), implanted with Gd-labelled dESCs, it was challenging to detect the labelled cells by examining the images due to the mixed signals at the site of bone fracture. Based on the T_1 shortening effect expected from Gd, we expected to see signal increase at the site of labelled cells. However unexpectedly, the SI values obtained from the proximal hole (no cells) were higher than that at the distal hole (labelled cells).

It is worth mentioning that the SI ratio appeared initially high at the distal hole then it decreased over time (from 0.7 to 0.4) (Figure 8-6 I, J, K & L). This suggests that Gd-labelled cells decreased over time which could be due cell proliferation, migration or death. Unexpectedly, the SI at the BM and the proximal hole did not show any increasing or decreasing patterns (Figure 8-6 L).

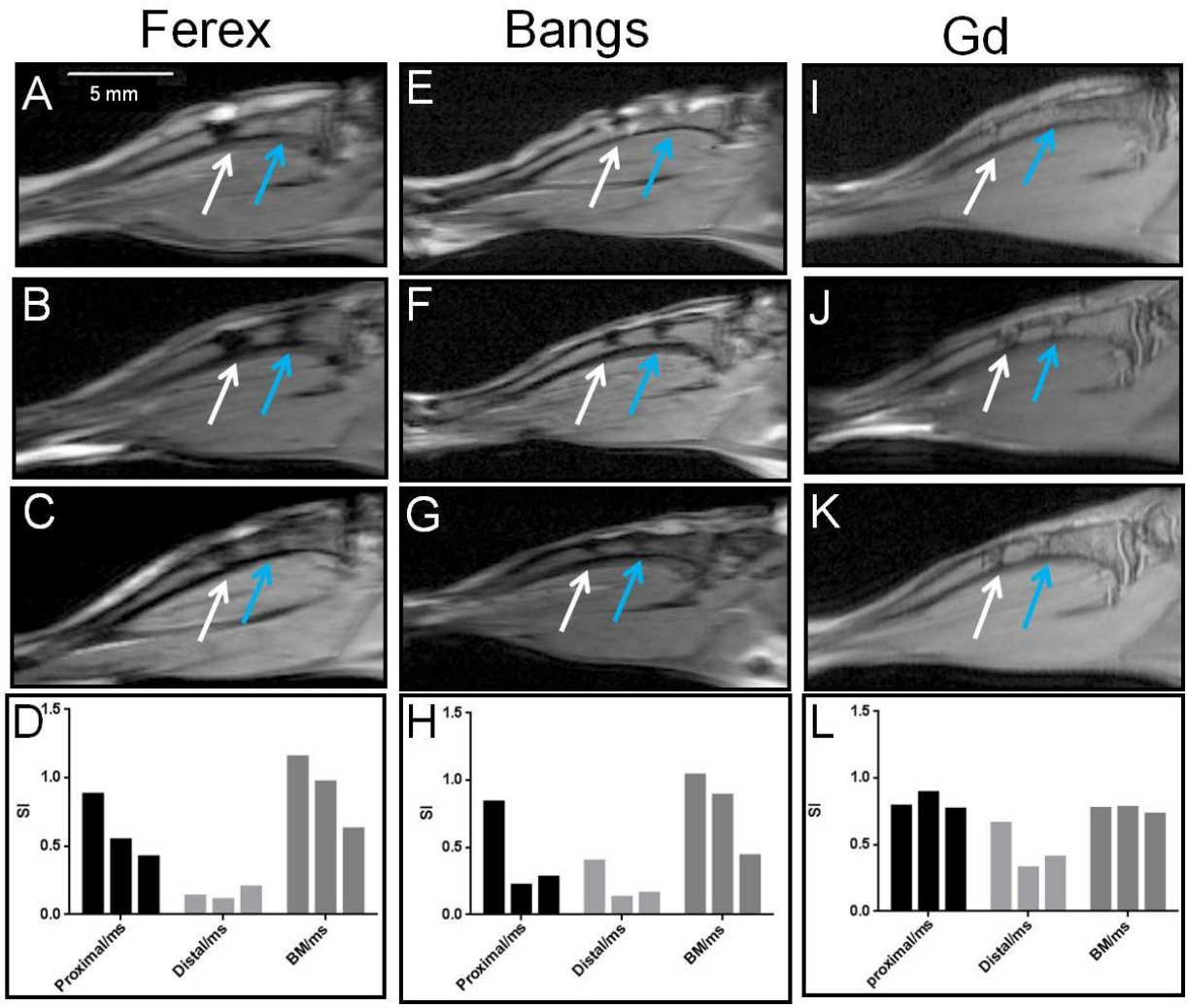

Figure 8-6 MR images and Signal intensity data of mice implanted with Ferex-, Bangs- and Gd-labelled cells. (A, B & C) MRI of an example mouse from Group 2 (Ferex-labelled cells at white arrow-distal hole) at day 1 (A), 7 (B) and 14 (C) post-surgery. (D) A graph showing the SI ratio changes of the proximal hole, distal hole and bone marrow across the time points (day 1, 7 and 14) for Group 2. (E, F & G) MRI of an example mouse from group 3 (Bangs-labelled cells at white arrow-distal hole) at day 1 (E), 7 (F) and 14 (G). (H) A graph showing the SI ratio (SI of bone fracture to the SI of the gastrocnemius muscle) changes for Group 3, indicating decrease in SI at both holes and BM. (I, J & K) MRI of an

example mouse from Group 4 (Gado celltrack-labelled cells at white arrow-distal hole) at day 1 (I), 7 (J) and 14 (K) post-surgery. (L) A graph showing the SI ratio changes for Group 4.

8.3.1.2 µCT results.

We used µCT to confirm the location of bone injuries in correspondence to MRI in order to assure the accuracy of ROI determination and SI analysis (Figure 8-7). µCT was performed at day 14 on excised tissue after sacrificing the mice to avoid the unnecessary exposure of the mice to anaesthesia and radiation. All injuries were detected in the µCT at day 14 and it showed bone healing at the remodelling stage with less dense cortical bone than the surrounding bone architecture (Figure 8-7 B, D & F).

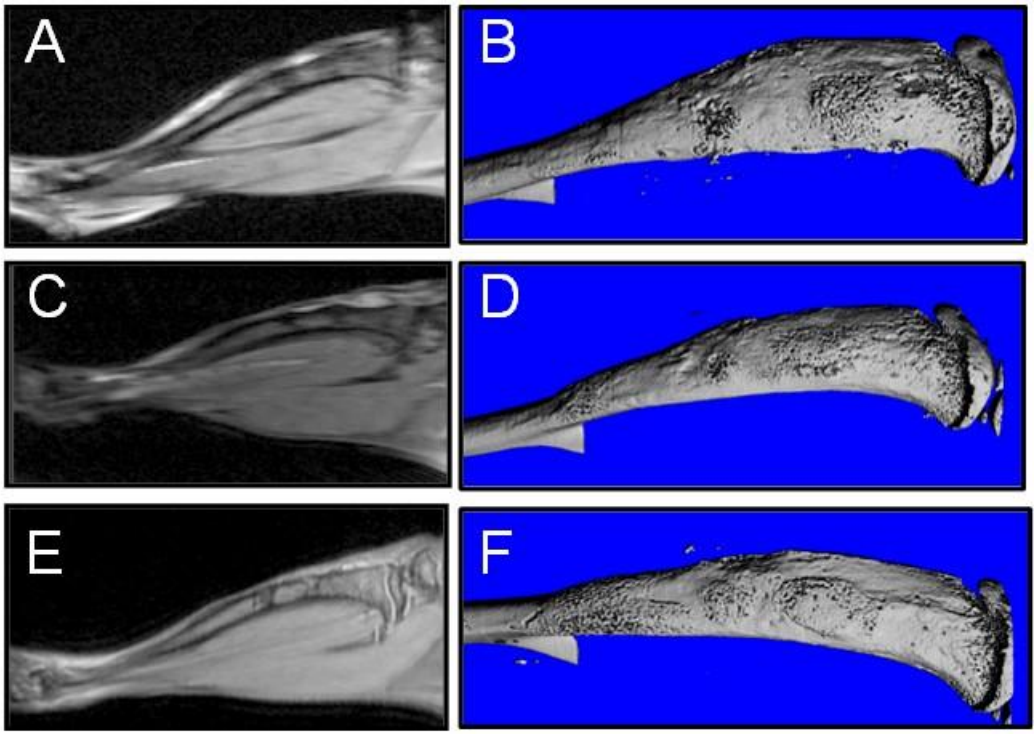

Figure 8-7 MRIs (left column) and 3D µCTs (right column) of mice tibiae at day 14. (A &B) Example mouse from Group 2 (Ferex-labelled ESCs). (C & D) Example mouse from group 3 (Bangs-labelled ESCs). (E& F) Example mouse from Group 4 (Gado celltrack-labelled cells).

8.3.1.3 Histology

In vitro *detection of iron-labelled cells in 3D gels.* PB staining of Gado celltrack-labelled ESCs in 3D gel showed an absence of iron from the cells (Figure 8-8 A). In contrast, Bangs- and Ferex-labelled cells in 3D gel showed blue spots inside the cells indicating the presence of iron inside the cells (Figure 8-8 B & C). The staining demonstrates internalization of one or two iron particles inside the cells.

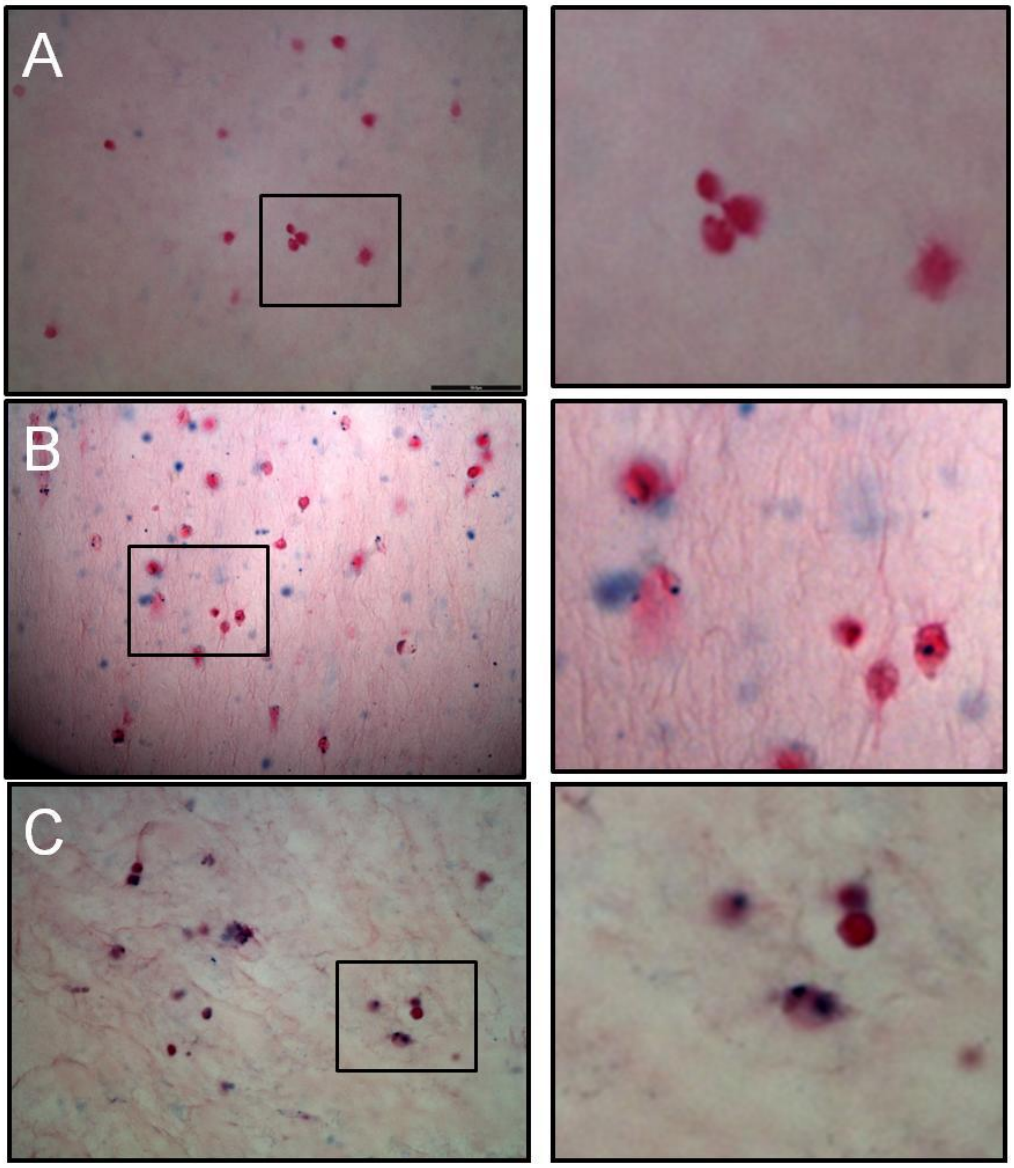

Figure 8-8 *In vitro* PB-stained sections counterstained with nuclear fast red. Red cells are dESCs. Blue spots within the cells are iron particles. (A) Gd-labelled cells (note the absence of blue spots within the cells). (B) Bangs-labelled cells (with blue iron particles within cells) (C) Ferex-labelled cells (with blue iron particles within cells). Scale bar 50 µm. The images in the right column are magnifications of the black boxes in the left column.

In vivo *detection of iron-labelled cells in 3D gels.* To determine the distribution of iron in the different tissues, mouse tibiae were stained with PB after imaging was complete and animals were sacrificed on day 14. In Groups 2 and 3 (Ferex- and Bangs-labelled ESCs), the proximal hole (no cells) had iron only in the bone marrow spaces (between the newly-formed trabeculae) and not in the newly-formed bone trabeculae itself (Figure 8-9). The distal hole had iron in the newly-formed bone trabeculae. The BM had iron all along the tibia (Figure 8-9). In Group 4 (Gado celltrack-labelled ESCs), no iron was detected in the proximal or distal hole. However a few iron granules were detected in the BM suggesting endogenous iron content (Figure 8-9). Additional images of PB stained sections were added to this figure to be used as a negative control to compare the iron distribution with treatment groups. These images belong to a mouse implanted with unlabelled dESCs in one hole and the other hole was left empty (Figure 8-9).

The fluorescent properties of the Bangs particles were detected in the bone fracture model at day 14 (Figure 8-10 B). The location of the red signal was similar to the location of iron particles in the PB-stained slides. The location of red signals and iron particles were also similar to the location of the black spots representing iron particles in the brightfield images (Figure 8-10 A & C).

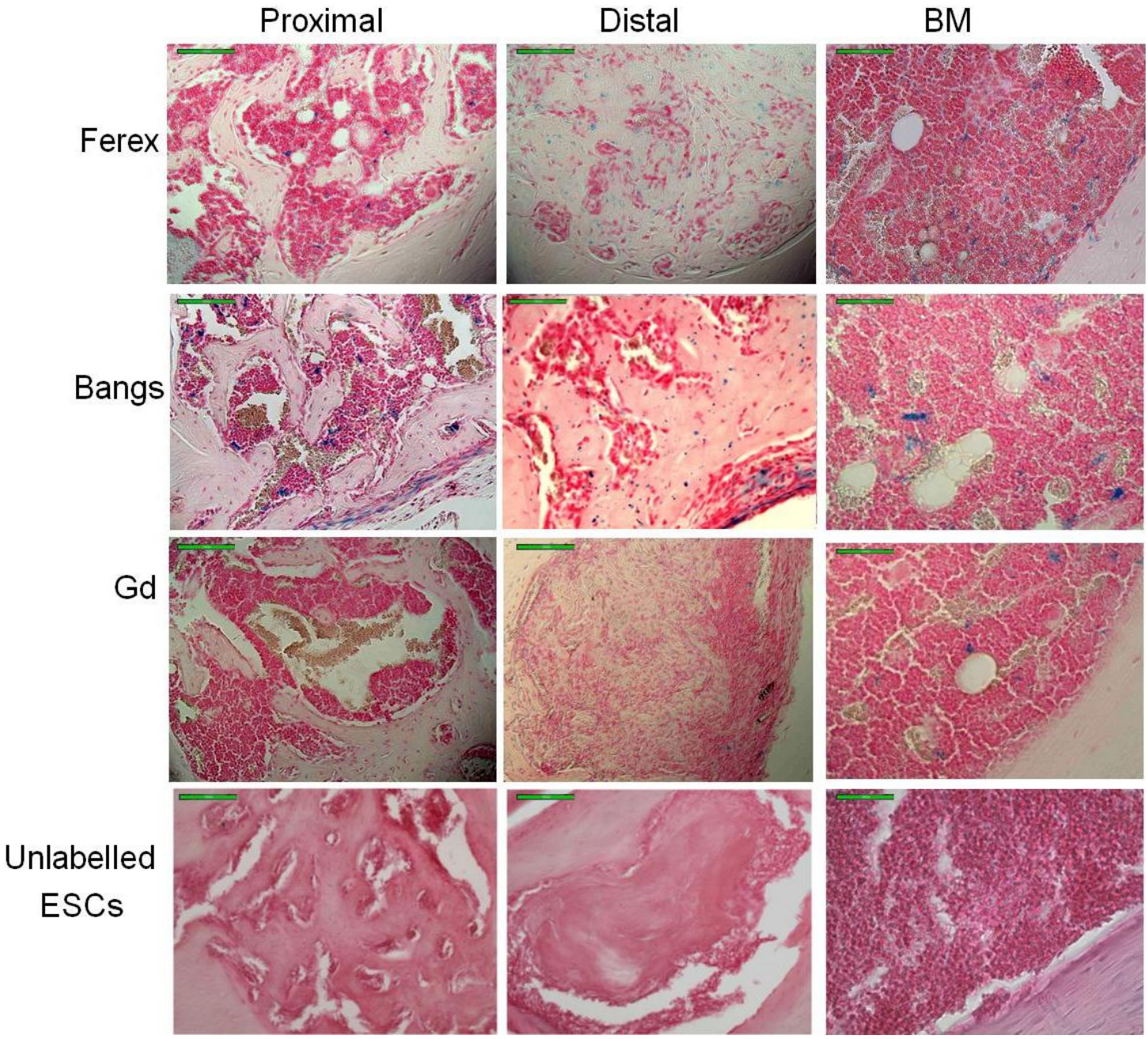

Figure 8-9 Representative histological sections of the mice from Groups 2, 3 and 4, stained with PB, at day 14. The sections show the proximal hole (no cells), the distal hole (labelled cells) and the bone marrow. Scale bar 100 µm.

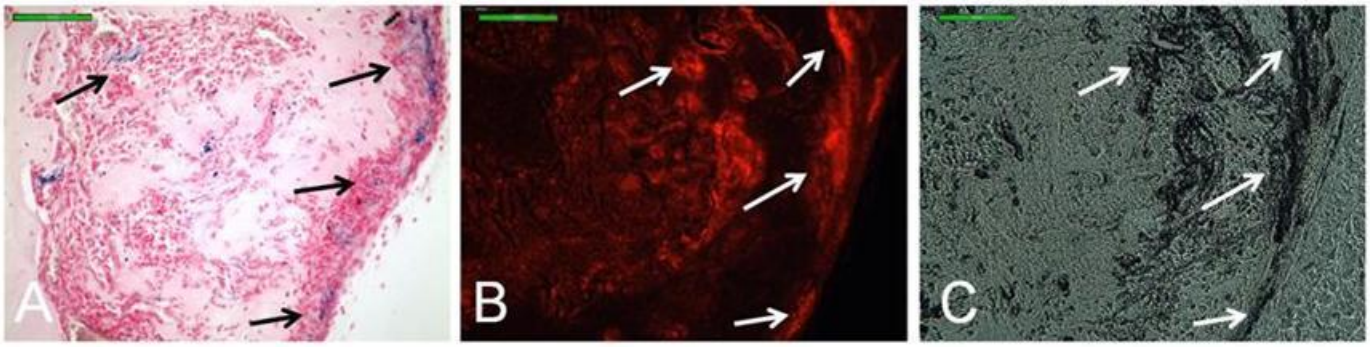

Figure 8-10 Sections of the distal hole of a mouse from Group 3 at day 14 (with Bangs-labelled cells). (A) PB stain (blue iron particles). (B) TxRed fluorescent image (red signal indicates the presence of the Bangs particles). (C) Brightfield image (black spots indicate the presence of iron). Scale bar 100 µm.

8.3.1.4 Immunohistochemistry.

Transplanted male cells could be identified by the brown-black spot in their nuclei. In Group 2 (Ferex-labelled cells), Y-chromosome-positive cells were found in the newly formed bone at the site of implantation and few Y-chromosome positive cells were found in the , periosteum, bone, BM and BM space at the proximal hole (Figure 8-11).

In Group 2 (implanted with Ferex-labelled cells), the location of Y-chromosome-positive cells from IHC was compared with the distribution of iron from PB staining in Figure 8-11. The results showed that iron was present at the same locations as Y-chromosome-bearing cells, except for at the growth plate (Figure 8-11). At the growth plate, iron appeared at the area of newly formed osteoid underneath the growth plate, while the Y-chromosome bearing cells appeared at the zone of proliferating chondrocytes of the growth plate (Figure 8-11). Given that iron particles and Y-chromosome positive cells were detected at almost the same locations, this

suggests that some of the implanted cells contributed to the healing process at the distal hole while others migrated to other sites of the tibia while retaining the iron label.

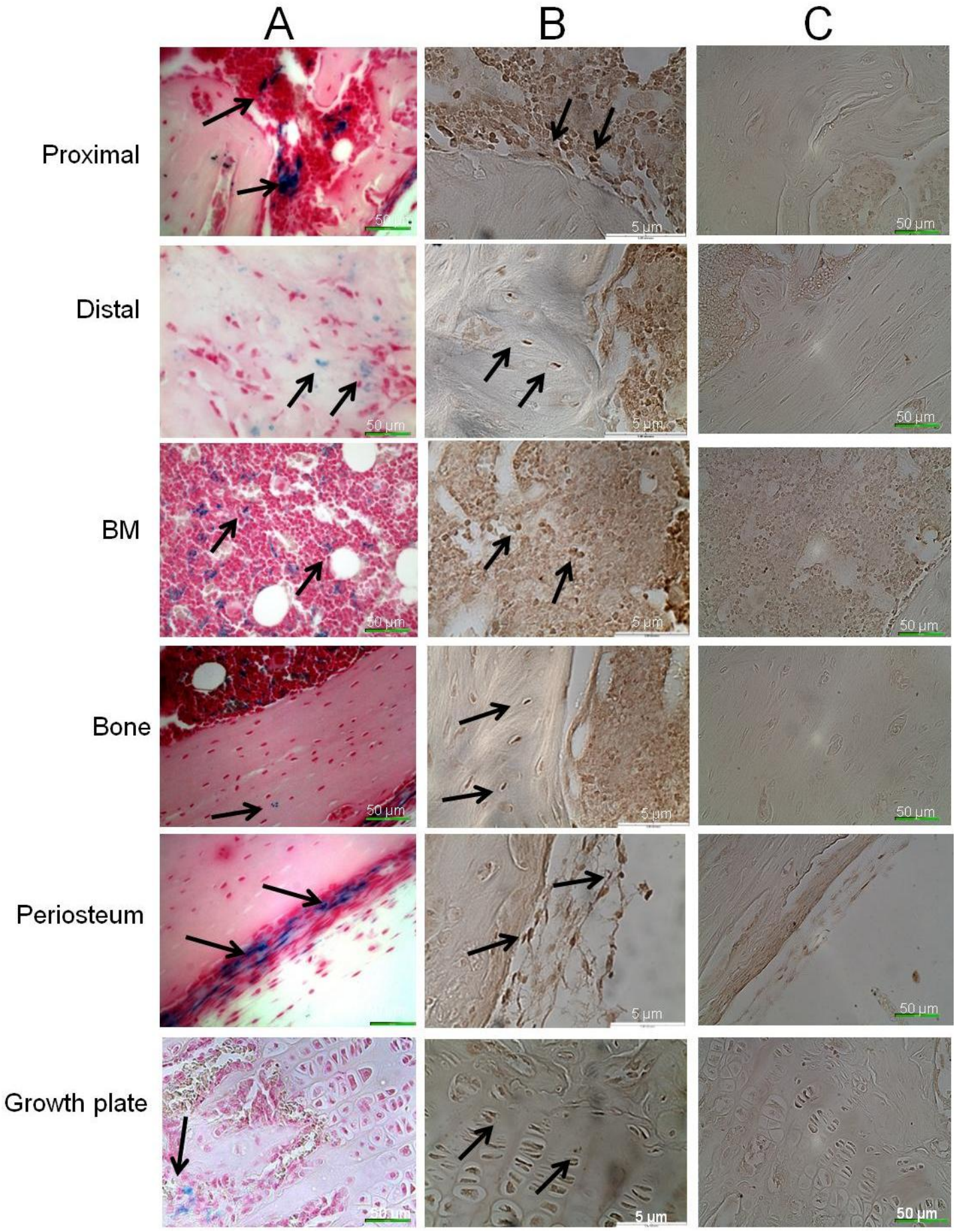
A
B
C
Proximal
Distal
BM
Bone
Periosteum
Growth plate
50 µm
5 µm

Figure 8-11 (Column A) Location of Ferex iron particles. (Column B) Y-chromosome-positive cells in a mouse tibia from Group 2 (with Ferex-labelled cells with probe and detection system). (Column C) Y-chromosome-negative cells in a mouse tibia from Group 2 (with Ferex-labelled cells without probe and with detection system). Ferex particles appear blue. Y-chromosome-positive cells have black-brown spot in their nuclei. The sites shown are for proximal and distal holes, BM, cortical bone, periosteum, and growth plate.

8.3.2 Results of Study 2, cell tracking using Ferex

8.3.2.1 *In vivo* MR imaging analysis and SI ratios data.

The drilled bone injuries were visible in both the control group and the treatment group at all time points. The distal hole implanted with Ferex-labelled GFP-ESCs appeared darker upon examination of the MR images at day 1, 7 and 14, than the distal hole in the control group (white arrows in Figure 8-12 A-F). The quantitative assessment of the labelled cells using SI measurements showed that distal hole of the treatment group (Ferex-labelled cells) had significantly lower SI than the distal hole of control (unlabelled cells) at day 1 (Mann Whitney, P=0.03), however at day 7 and 14 there was no significant difference between the two holes (Mann Whitney, P=0.28 and P=0.42 respectively). This suggests that the amount of iron was highest at day 1 then it decrease across time which could be could be due to cell migration or death.

At the distal hole (Ferex-labelled cells), SI measurement showed slight increase across time, which confirms the decrease of iron content at this area (Figure 8-12 I). Unexpectedly, the SI at the proximal hole showed slight increase across time (Figure 8-12 J). This suggests that no labelled cells or no iron travelled to the proximal hole another possibility is that the amount of iron or labelled cells that travelled to the proximal hole were below the detection threshold.

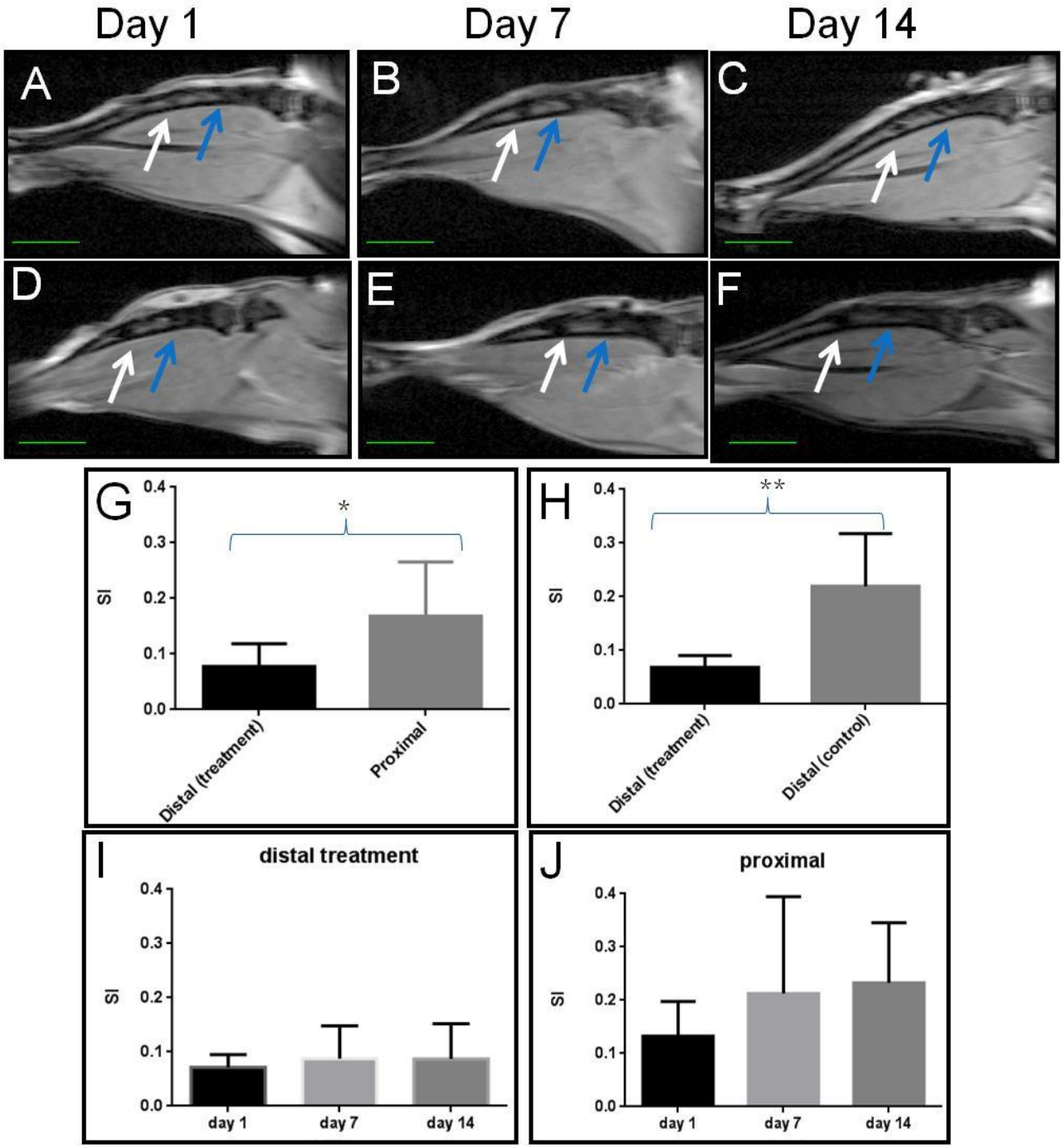

Figure 8-12 MR images and Signal intensity data of holes containing GFP-dESCs and holes that were left empty. (A, B & C) MRI of an example mouse from the control group (unlabelled cells implanted at white arrow-distal hole) at day 1 (A), 7 (B) and 14 (C) post-surgery. (D, E &F) MRI of an example mouse from the treatment group (Ferex-labelled cells implanted at white arrow-distal hole) at day 1 (D), 7 (E) and 14 (F). (G-J) Graphs

showing the SI ratio changes within treatment group (G), between treatment and control group (H). (I) A graph showing the SI ratio changes at the distal hole of treatment group at day 1, 7 and 14. (J) A graph showing the SI ratio changes at the proximal hole of treatment group at day 1, 7 and 14. Scale bar 4 mm.

8.3.2.2 Histology

In vitro *detection of cells with PB, H & E, GFP staining and fluorescent microscopy.* PB staining of undifferentiated GFP-ESCs demonstrated the presence of iron (blue spots) in the Ferex-labelled GFP-ESCs but not in unlabelled GFP-ESCs (Figure 8-13 A & B). The PB staining of dESCs in gels demonstrated the presence of iron particles inside the Ferex-labelled GFP-dESCs and absence or iron in unlabelled GFP-dESCs (Figure 8-13 C & D). This indicates that GFP-ESCs were able to take up the Ferex contrast agent and retain it through the differentiation process for 16 days.

When sections were examined under fluorescent microscope, both the Ferex-labelled and unlabelled GFP-ESCs showed GFP-positive cells (Figure 8-13 E & F). The GFP staining demonstrated the presence of GFP positive cells inside the collagen gel (Figure 8-14 A). This indicates that ESCs were successfully transfected with GFP gene and that the transfected GFP-ESCs retained their capacity to express GFP after being labelled and differentiated for 16 days. Absence of GFP was noted in sections stained with detection system and without GFP antibody (Figure 8-14 B).

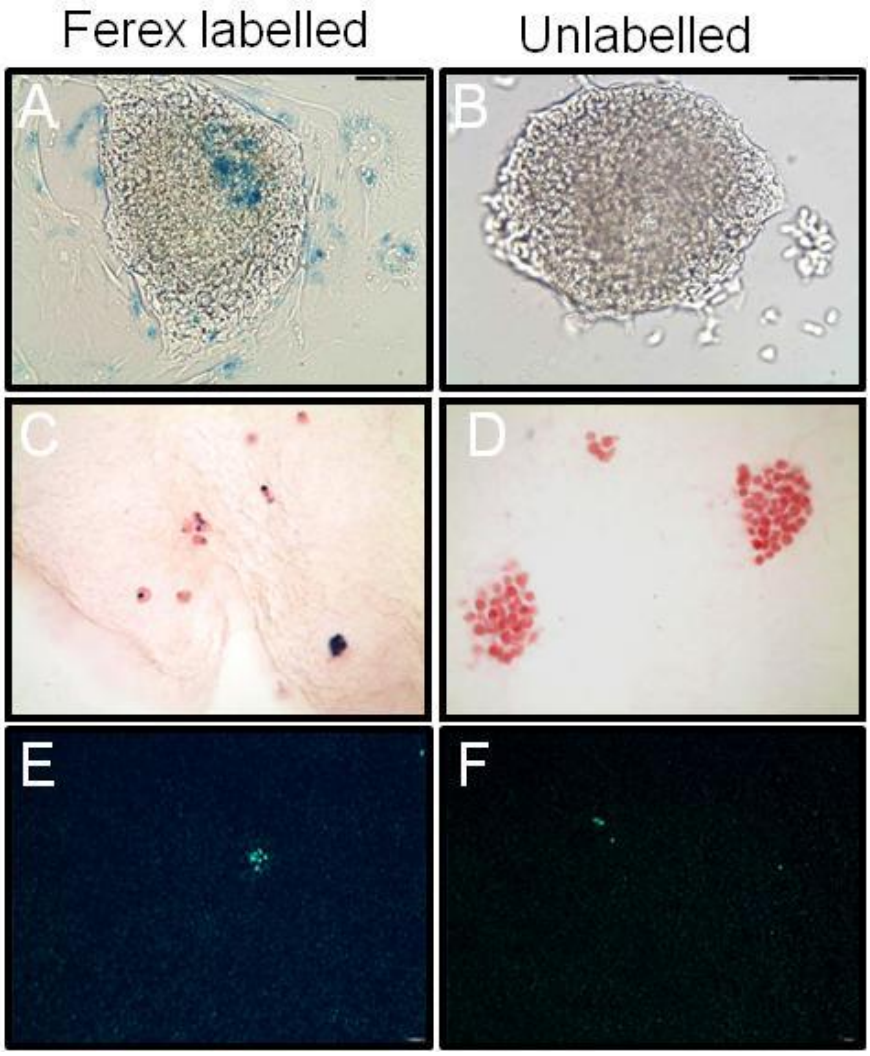

Figure 8-13 Ferex-labelled GFP-ESCs (left column) and unlabelled GFP-ESCs (right column). (A & B) PB staining (A) Undifferentiated GFP-ESC colony labelled with Ferex showed positive blue spots indicating the presence of iron. (B) Undifferentiated unlabelled GFP-ESCs stained negatively for iron. (C & D) Fluorescent images of Ferex-labelled and unlabelled GFP-ESCs in 3D construct. GFP-positive cells appear green. (E & F) PB and nuclear fast red stained Ferex-labelled cells showed positive blue spots indicating the presence of iron (E) and unlabelled cells (F).

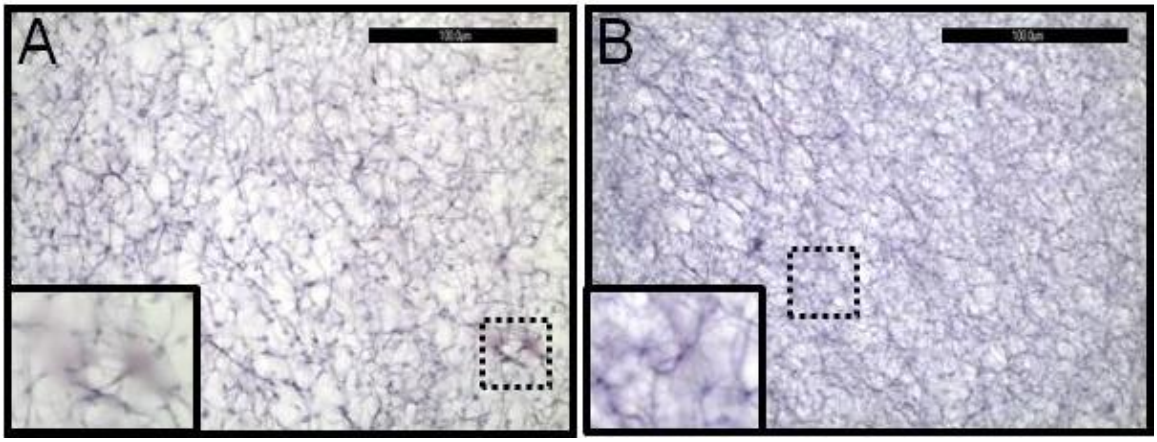

Figure 8-14 GFP-dESCs in 3D collagen construct stained for GFP (HRP/DAB detection lightly counterstained with hematoxylin). GFP protein appears as brown areas indicating the presence of GFP-positive cells. (A) GFP-ESCs stained with GFP antibody and detection system. (B) GFP-ESCs with detection system only and no GFP antibody. Scale bar is 100 µm.

H and E results. The fluorescent signal of the GFP cells coregistered with the positive iron staining and the highly cellular area in the H & E section (Figure 8-15 A, b & C). At day 14 in the distal hole, a bone-like tissue was detected in the same shape of the implanted collagen with a highly cellular content (indicated by the purple nuclei). A rim of calcified bone seemed to surround the implanted collagen (Figure 8-15 C). In the proximal hole, the progress of healing was demonstrated by the presence of trabecular bone at a remodelling stage (Figure 8-15 D)

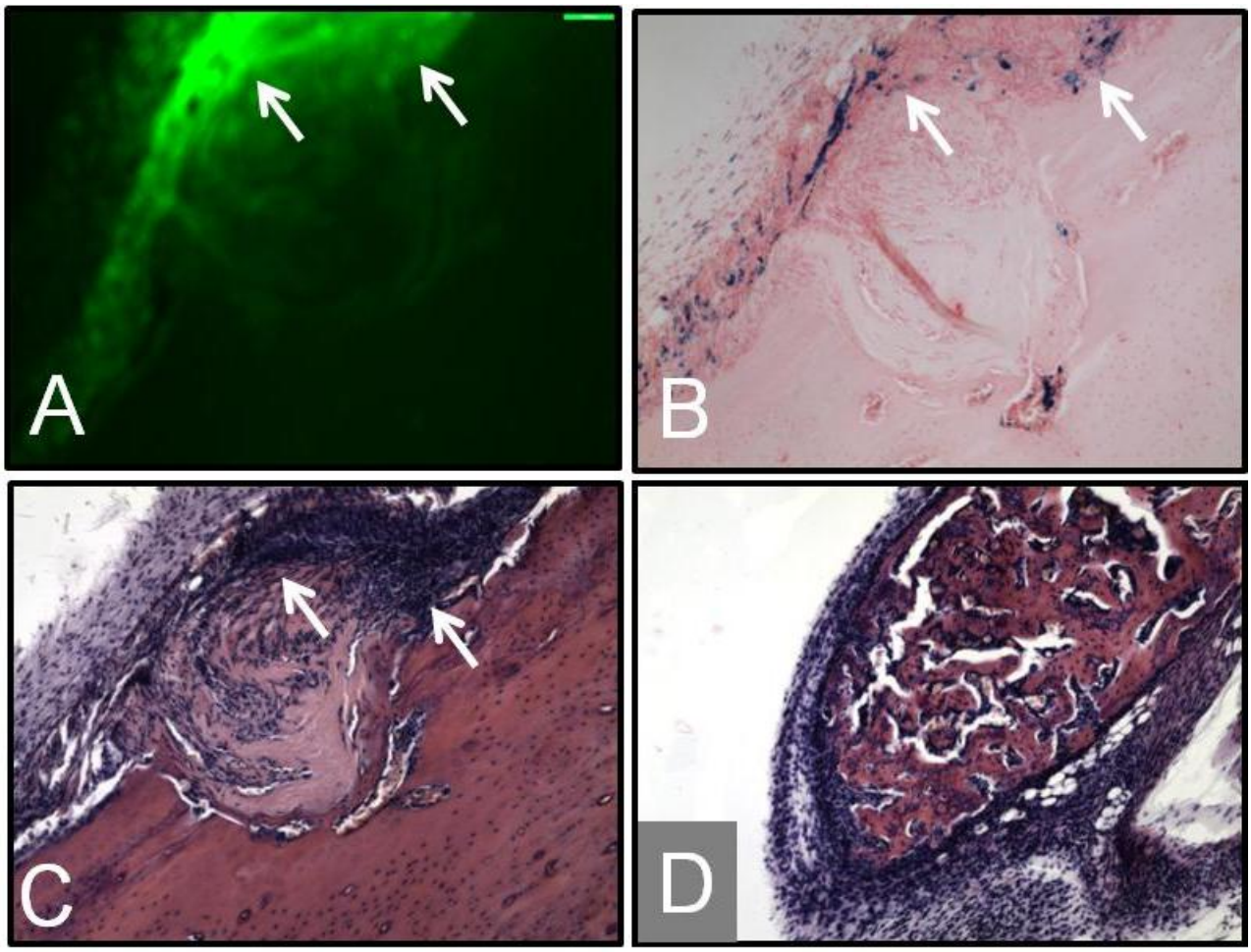

Figure 8-15 Fluorescent, PB, and H & E sections of a mouse from the treatment group at day 14 post implantation. (A) Fluorescent image of Ferex labelled cell-construct in the distal hole. (B) is the corresponding PB staining of section (A) and (C) is the corresponding H & E section. They demonstrate that the fluorescent signal is at the same area of the iron particles and high cellular content in the H & E. In (C) bone like tissue with mineralized edges indicated was detected at the site of implantation. (D) The proximal hole with nothing implanted illustrates a remodelling stage of bone healing with trabecular bone formed. Scale bar 100 µm.

8.3.2.3 Immunohistochemistry.

The results of iron, macrophages and GFP protocols. The macrophage staining comparison with the distribution of iron at day 14 indicated that iron was found at the same locations as macrophage cells in the bone marrow and bone marrow area between the newly formed trabeculae at the proximal and the distal hole (Figure 8-16). GFP positive cells were detected in the newly formed bone at the distal hole at the same locations as iron. However it was challenging to detect GFP positive cells in the BM and proximal hole due to the high background staining (Figure 8-16). This suggests that 14 days post-implantation GFP cells were still alive, and that they incorporated into the newly formed bone at the distal hole. At the same time, the presence of iron particles and macrophages at the same locations suggests that that some cells died, transferring their iron to macrophages.

Tracking of iron and GFP cells over time revealed presence iron particles and GFP-positive cells in the distal hole, at day 1 and 14 (Figure 8-17).

In vivo distribution of iron. At day 1, the PB results detected the presence of iron at the distal hole (Ferex-labelled cells) (Figure 8-17 C), conversely no iron was detected at the proximal hole (no cells) (data not shown), and weak positive iron signal was detected in the bone marrow tissue which suggests endogenous iron (data not shown). At day 14, the PB results detected the presence of iron in BM, BM tissue in between the newly formed trabeculae in the proximal hole (Figure 8-16 A, F & P) and most importantly in the newly formed bone of the distal (Ferex-labelled cells) (Figure 8-16 F & Figure 8-17 G).

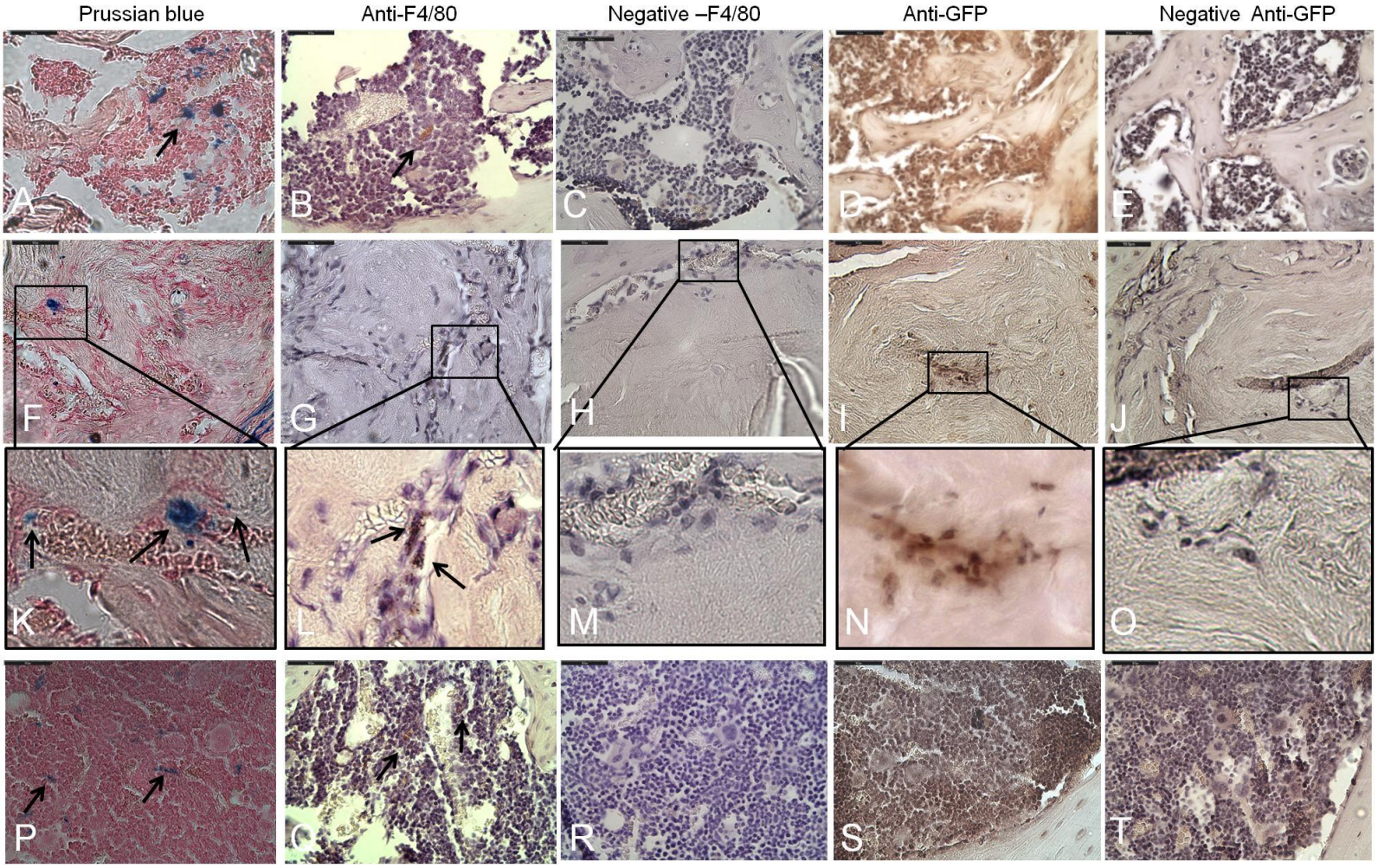

Figure 8-16 Multiple staining in a mouse from the treatment group at day 14 to investigate whether iron is inside macrophages or GFP positive cells. PB staining with iron appearing as blue spots (left column), macrophage staining with macrophage cells appearing as brown spots (middle column) and GFP staining with GFP cells appearing as brown spots (right column). (A-E) Proximal hole (no cells). (F-J) Distal hole (Ferex-labelled cells). (K-O) Magnifications of F-J. (P-T) Bone marrow. Scale bar 50 µm.

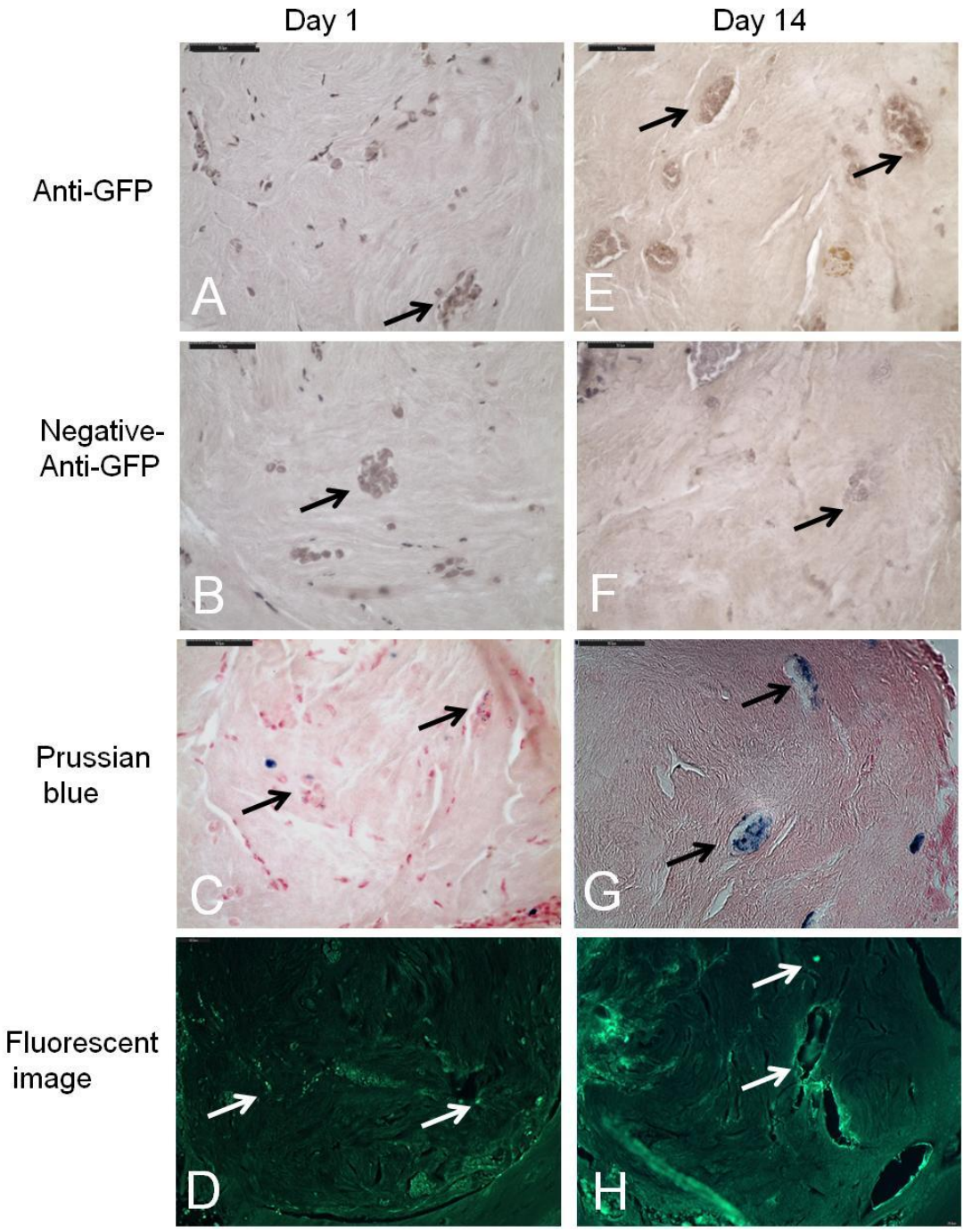

Figure 8-17 GFP, PB staining, and fluorescent imaging of mice from the treatment group at day 1 (left column) and 14 (right column) post surgery. (A & E) GFP staining showing GFP-positive stained cells appear as dark brown-black spots. (B & F) negative GFP staining (with detection system and without the GFP antibody), no GFP-positive stained cells detected. (C & G) PB staining showing iron as blue spots. (D & H) Fluorescent images showing green fluorescing cells, suggestive of GFP-positive cells. Scale bar 50 µm.

8.4 Summary of findings

In study 1 it was challenging to detect the Gado celltrack-labelled cells in the bone due to the mixed signals obtained from the site of fracture (bright and dark areas). The Ferex-labelled cells decreased the SI at the distal hole when compared to the proximal hole at day 1, and then SI started to increase gradually over time suggesting the decrease of iron content at this area. Additionally, the SI changes at the distal hole, proximal hole and bone marrow suggest the migration of iron-labelled cells from the distal hole to the proximal hole and bone marrow. This was also evidenced from Y-chromosome IHC protocol, where similar distribution of iron and Y-chromosome-positive cells was observed, at the different sites in the tibia. The Y-chromosome staining also indicated that part of the cells integrated in the newly formed bone at the distal hole. Given that the group with the Ferex-labelled cells had only 2 mice, we decided to further investigate the use of Ferex-labelled cells using bigger number of mice and additional IHC protocol in study 2. The additional IHC would be used to learn about transfer of the iron label from implanted cells to macrophages after cell death and to confirm our findings about cell migration.

The results of study 2 showed that the SI increased at the distal hole across time however it did not decrease at the proximal hole and bone marrow as expected from Study 1. This indicates that the labelled cells at the distal hole were diluted but it does not support the migration of the cells to the proximal hole and bone marrow. Similar to MRI SI data, the GFP IHC results indicated the presence of GFP cells in the distal hole but it did not show GFP cells elsewhere. The macrophage IHC results suggest partial cell death and the transfer of iron to macrophages. The SI data together with the GFP and macrophage IHC indicates that part of the cells stayed at

the distal hole and contributed to the newly formed bone and other part died and transferred their label to macrophages.

8.5 Discussion

The novelty of the work presented in this chapter was the use of the labelled-dESCs in a 3D scaffold, and tracking them in bone using MRI. Previous cell tracking studies extensively investigated cell tracking in soft tissues like heart[63,64], muscle[156] and brain[155]. To date no studies have investigated cell tracking in bone. This is due to the complex nature of the bone signal. In this study we developed a cell tracking protocol in bone fracture and we addressed some concerns related to the fate of the implanted cells and iron.

To assure consistency among the two studies performed in this chapter, all experimental conditions were standardized except for the type of cells transplanted. The standardized conditions were the distances between the bone fractures, the size of the bone fractures, the cell culturing conditions, the surgical procedure, the MR imaging time points, and the mice housing conditions. This standardization was done to assure that the results obtained are due to treatment effects and not reproducibility. However, in future studies, interaction data analysis is recommended to minimize the probability of reproducibility error.

In order to track cells *in vivo* using MRI, the cells needed to be labelled with a contrast agent that possesses enough relaxivity for *in vivo* visualization. In our experiments, we investigated tracking Gado celltrack-labelled cells and Ferex-labelled cells. The visualization of Gado celltrack-labelled cells was challenging due to the mixed hyper-and hypointense spots detect in the bone fracture. The mixed signals could be attributed to the presence of bone and inflammatory fluids. Also, the inability to detect the Gd-labelled cells could be due to the low detection sensitivity of the Gd compared to iron. In a previous report, Baligand *et al.* proved that

it is possible to track Gd-labelled cells in muscles at high cell concentrations 2 x 10^{6} [158]. In another study done by Daldrup-Link *et al.*, 1 x 10^{6}-3 x 10^{8} Gd-labelled cells were injected intravenously in mice to be detectable in MRI. Thus, it is probable that Gd-labelled cells (~2 x 10^{5} cell) did not changes the SI because they were below the detection threshold. Thus, to obtain significant signal changes with Gd-labelled cells we need to implant 2 x 10^{6}[158]. This is way beyond the capacity of the bone fracture model we are using. Therefore, Gado celltrack-labelled cells might not be appropriate for cell tracking in our bone fracture model. Instead, it could be used in applications where cell detection sensitivity is less important to the success of tracking[158]. This is considered a strong argument in favour of using iron-labelled cells for our model.

Ferex-labelled cells were successfully detected in MRI, the labelled cells decreased the SI and appeared darker than the control holes in T_2 weighted images upon visual examination of the images. The ability to detect the Ferex-labelled cells could be attributed to the high relaxivity offered by iron contrast agents compared to Gd ones[139,158]. Besides our relaxivity results from chapter 6, the reports that compared Gd and iron relaxivities proved that iron had higher relaxivity than Gd[139,158]. This is one of the biggest advantages for using iron in cell tracking because it allows the detection of smaller numbers of labelled-cells compared to Gd. For example, Bulte and his group were able to track~5 x 10^{4} iron-labelled cells for up to 6 weeks in rat brains[70].

An equally important criteria to the relaxivity and detectability of the contrast agent, is its biocompatibility. To use cell tracking protocols in monitoring new cell therapies, the labelling should not negatively impact cell viability or differentiation. In this chapter, we did not extensively investigate the labelled cell viability because this has been covered in chapter 6 and

we know that our labelling protocol did not adversely affect the cell viability. This agrees with a previous study done by Kostura *et al.*, where he proved that iron labelling has no adverse effect on the mesenchymal stem cells viability. Additionally, he proved that the labelling did not inhibit the osteogenic differentiation capacity[165]. In another study done by Li *et al.*, GFP-ESCs labelled with iron gave rise to all tissue lineages *in vivo*[166,30], which indicates that iron labelling did not inhibit any lineage specific differentiation. This implies that the labelling protocol used in our project is safe and does not affect the cells adversely.

Two approaches of cell delivery to bone fracture were studied in this chapter. In the first one, labelled ESCs in an undifferentiated form (in suspension) were used to avoid the possibility of label dilution that can happen upon cell differentiation. However, this approach was problematic because the cells lacked the needed mechanical retention and they were flushed right after injecting them. For this reason, we used a differentiation protocol[30,44] that directs the cells to osteogenic lineage and provide them with the needed mechanical support[30]. The labelling-differentiation protocol optimized and used in this thesis enabled the cells to retain the iron label through the 16 days differentiation period. This agrees with Cahill *et al.* where he showed that labelled muscle stem cells could be differentiated to mature muscle fibers while retaining the iron label through the differentiation process[156]. That is to say, the scaffold we use contains efficiently labelled cells which entitle the scaffold to be tracked *in vivo* using MRI.

There are important aspects that need to be addresses in developing a cell tracking model. These aspects include studying the fate of iron, studying the behaviour and fate of implanted labelled cells, and accounting for the previous two factors in SI interpretation.

Studying the fate of iron. The MRI signal increased at the distal hole (Ferex-labelled cells) suggests that the iron or iron carrying cells got diluted at the site of implantation over time and

moved away to other sites. The theory behind this phenomenon is not fully understood. However, we propose three possible mechanisms with suggestive evidence from the IHC data. The first mechanism suggests that significant number of implanted cells died after implantation and the iron was possibly transferred to macrophages which migrated and carried the iron away to other sites. This mechanism was reported by Cahill *et al.* when he injected dead iron-labelled mesenchymal stem cells in a mouse muscle and found that the iron was cleared away possibly by macrophages which then migrated to other sites[156]. In Cahill's report no macrophage specific staining was done to confirm his results[156], however in our study (Study 2) we used antibody F4/80 to stain for macrophages. Similar to Cahill's report, our results showed that macrophage cells were found at the same sites as iron particles which support the first proposed mechanism.

The second proposed mechanism for travelling of iron away from the distal hole (Ferex-labelled cells) could be based on free movement of iron after its release from dead cells and its eventual uptake by macrophages at distant sites from the distal hole. This mechanism contradicts with Cahill's report, where he showed that the labelled macrophages were migrating starting from the site of graft[156]. In our experimental work, we did not perform any specific studies to test for this mechanism; however our speculation based on the literature is that this mechanism is unlikely to happen, because it is uncommon for iron label to be release and move freely without being cleared by macrophages[69,73,140,158].

The third proposed mechanism for travelling of iron away from the distal hole (Ferex-labelled cells) could be through the migration of the labelled implanted cells. Several reports supported this theory[154,69,70,167]. For example, Bulte *et al.* showed that iron labelled neural stem cells had the ability to migrate after injection in brain tissue, and that most of the migration happened within the first two weeks[70]. This is evidenced from our Y-chromosome data at day 14

post surgery(Study 1) where the iron and Y-chromosome positive cells were found at the same sites (bone marrow, proximal hole and periosteum), suggesting that the implanted cells migrated carrying the iron within it.

Studying the behaviour and the fate of cells. Implanted cells can integrate into the host tissue[158], cells can die and transfer their iron to macrophages[156], or they can migrate away from the site of implanation[69,70,154,167]. Baligand *et al.* showed that labelled myoblasts implanted in mice integrated into the host muscular fibers[158]. Cell integration in the host tissue was also supported by our results in which Y-chromosome positive cells and iron was detected in the newly formed bone at the site of implantation. Integration was also evidenced by the low SI measurements at the site of implantation compared to the proximal hole for up to two weeks after implantation. Secondly, cells can die followed by the release and transfer of iron to scavenger cells[73,158]. Our the results suggest this could have happened in our model, evidenced by iron and macrophage-positive cells being found in similar locations in the BM, distal hole and proximal hole. Labelled macrophages did not cause detectible SI changes in MRI in Study 2. Finally, the cells can migrate from the implant site to other sites[129,168]. Several studies tried to understand the theory behind cell migration[81,162,169], however, to date there is no clear understanding of this mechanism.

The most commonly supported theories that explain cell migration are Fe-mediated cellular signalling pathways[129], the cytokines produced at the other injury site acts as chemo-attractants to implanted cells[167], and the effect of magnetic forces from the MRI on the iron labelled cells[170].

Fe-mediated cellular signalling pathways could be induced upon the degradation of iron and the presence of free iron radicals inside the cells[129]. Free iron can be used by the cells for metabolic functions, stored as ferritin, contribute to red blood cell synthesis[129], or can spur the

cell migration process[129,168]. It was reported by Chen *et al.* that labelling of MSC with iron induced their migratory capacity through three signalling pathways: 1) Matrix metalloproteinases (MMPs), 2) Wnt/β-catenin, and 3) Synovial sarcoma X antigen (SSX) pathway[168]. SSX and MMPs pathways are down regulated after osteogenic differentiation which might decrease the cell migratory capacity[168]. The Fe-mediated cellular signalling could be the explanation behind the migration of dESCs (Study 1). In contrast, GFP-ESCs did not show cell migration which could be attributed to the presence of the GFP gene that affected the Fe-mediated signalling pathways and reduced cell migration. For the previously mentioned effect of iron on the cells, iron contrast agents are always coated with a dextran coating to delay their biodegradation, release and the consequent cascade of Fe-mediated cellular signalling pathways[10,129,138]. However, the dextran coating does not completely inhibit the release of free iron.

Other studies demonstrated additional pathways contributing to the cell migration process such as the release of inflammatory cytokines from sites of injury which acts as chemo-attractants for cells[167]. Another equally important pathway is the effect of magnetic moment of the MRI machine on the cell[170]. This phenomenon is known as magnetophoresis in which cells can migrate in response to the magnetic forces applied on them[171]. For the magnetic moment to induce cell migration, the magnetic force has to overcome the retention forces of the cells with their surroundings[170]. To date, it is not known if the cells stay in place once the applied magnetic field is withdrawn[170]. In our experiments, we assume that the effect of this force was minimal due to the presence of a high retention force on the cells caused by the 3D scaffold that mechanically supported the cells at the site of fracture. Thus, it is unlikely that cell migration was due to the magnetic force of the MRI machine.

SI interpretations. Unexpectedly, the MR signal loss corresponded to labelled implanted cells only and not to labelled macrophages. This could be explained that after the release of iron from the cells, the macrophages phagocytosed the iron at concentration lower than the MR detection threshold which made the labelled macrophages undetectable. This is in contrast to the results obtained by Baligand *et al.* who have reported that the iron transferred to macrophages after cell death causes SI changes similar to that obtained from labelled transplanted cells[158]. However, based on our results it is suggested that MR tracked viable labelled implanted cells and MR did not detect cells after their death and the release of iron.

Also, our SI results showed that signal loss in MRI corresponded to the location of migrating labelled cells in IHC. This demonstrates the feasibility of using MRI to track migrating labelled cells.

Quantitative MRI tracking of labelled cells was previously done using SI analysis, but in other, non-bone tissues[74,130]. However, to date no cell tracking studies were done in bone. The difficulty of using iron-labelled cells in the bone fracture model is that, unlike other body tissues, the short T_2 relaxation time of bone produces low signal and makes it appear as a hypointense area[48]. Iron-labelled cells also appear dark and have low signal intensity. Despite this, we demonstrated the ability to track iron-labelled ESCs in a bone fracture using SI measurements.

Overall, we developed a cell tracking model where it is possible to track the location and migration of Ferex-labelled cells in a bone fracture model. Additionally, our work gave information about the fate of iron and the fate of the implanted cells. This model has potential application in the field of bone regeneration and could be used to test other types of cell therapies in bone injuries

Chapter Nine: **Discussion**

9.1 Research approach and outcomes

Regenerative cell therapies showed promising results in healing a bony defect[30,32,37,38,157]. However, the exact behaviour of the cells *in vivo* is still being investigated. In order to assess the behaviour and fate of the cells *in vivo,* a non-invasive imaging method is of needed. To date there is no method to track cells longitudinally in a bone fracture model. This thesis presents the development of an MR cell tracking model in bone fracture. The development of this model went through various stages to optimize the imaging, labelling and the tracking of the cells. The outcome of our work showed that the developed cell tracking model could be used to track cells in bone and provide information about their *in vivo* behaviour. This model could be potentially be used to test new cell therapies in bone injuries.

9.1.1 Optimization of MRI for imaging a mouse bone fracture model

In order to develop the MRI cell tracking model, first we optimized an MR imaging protocol. The goal was to find an MRI sequence and associated parameters that enabled the visualization of the bone fracture, labelled stem cells and the anatomical structures surrounding the fracture, all in a reasonable acquisition time. Although gradient echo (GE)-based sequence was better at detecting iron than spin echo (SE)-based sequence, it gave too many artefacts that obscured the visualization of anatomical structure. Thus, the optimized sequence that fulfilled all the mentioned criteria was a spin echo (SE)-based sequence called Rapid Acquisition with Relaxation Enhancement (RARE). SE-based RARE was used the most in our studies. In some experiments RARE was combined with the GE sequence to assist in visualizing the iron-labelled cells.

9.1.2 Imaging of biomaterials used as stem cell scaffolds and validation using μCT

We compared MRI with μCT as the gold standard for bone imaging, to determine whether MRI could be used to visualize implanted biomaterials in a bone fracture. Additionally, we wanted to study the effects of some biomaterials, commonly used in bone regenerative therapies[8,33,106,172], on signal intensity in MR images. Different biomaterials appeared differently in MRI, yet they were all successfully detected. Overall, MRI correlated well with μCT and provided comparable information about the bone injuries and the scaffolding biomaterials implanted into them (Section 3.3). Thus, MRI can be used to monitor both the scaffolds used in stem cell therapies and their effects on bone healing. MRI might be an especially useful alternative to μCT because it can be used when ionizing radiation needs to be avoided, such as in longitudinal studies [45].

9.1.3 Assessment of MR contrast agents for cell labelling and imaging **in vitro**

In the process of developing a cell tracking model, the cells needed to be labelled with a contrast agent. The contrast agent of choice need to have enough relaxivity to be visualized in MRI, plus it should not adversely affect the biology of the cells.

Three iron-based, negative (T_2) contrast agents were investigated *in vitro* and their relaxivities were studied in chapter 5 (Feridex, Ferex and Bangs). Feridex had sufficient relaxivity for *in vivo* studies, however it is no longer manufactured. Like Feridex, Bangs and Ferex also provided enough relaxivity for our *in vivo* studies and they can be used as T_2 contrast agents. Then, we tested the labelling capacity of these contrast agents and their effect on the cells. Our results from chapter 6 showed that all three contrast agents had the ability to label ESCs without adversely affecting their viability or proliferation capacity. We also found that the labelled cells can be detected *in vitro* using MRI.

In addition to the three negative contrast agents described above, two positive (T_1) contrast agents were also investigated. One was Gado celltrack, a relatively new contrast agent that was specifically manufactured for cell labelling and tracking purposes with a larger particle size than conventional Gd compound[134]. Like the negative contrast agents described above, Gado celltrack had the ability to label ESCs and did not adversely affect them (chapter 5).

As we previously mentioned, bone suffer lack of signal in MR images which complicated its imaging. In an effort to overcome this problem new positive contrast agents are being developed. We tried to contribute t o the development of a new contrast agent. The advantage of the new contrast agent was to have a bone targeting feature and a higher relaxivity than the previously used ones. To contribute to its development, we tested how efficiently the nanoparticle (NP) encapsulated gadolinium (Gd, a positive contrast agent). The results showed that Gd was efficiently encapsulated in the bone targeting liposomes and that the new bone targeted Gd agent could be potentially used to overcome the signal problem in bone imaging.

Previous studies have demonstrated that undifferentiated ESCs cause tumours when injected *in vivo*[43]. Thus, we needed to use dESCs in our model. Also, we observed in preliminary trials that ESCs would not stay at the site of an *in vivo* bone fracture unless they were embedded in a 3D biomaterial scaffold (Section 8.3.1.1). Our research group previously published methods for osteogenic cell differentiation[30,44]. We attempt to develop a protocol that combine cell labelling and differentiation. This was successfully achieved and a labelling-differentiation protocol that generated labelled, dESCs embedded in 3D biomaterial scaffolds was developed in Section 6.2. Upon development of this protocol, ESCs were ready to be implanted and imaged using MRI in *in vivo* bone fracture models.

9.1.4 **In vivo** ***MRI-based ESC tracking in muscles and in bone fracture with histological characterization of ESCs post-implantation***

The final step in the developing of the cell tracking model was to translate our *in vitro* work to *in vivo*. Since *in vivo* bone injuries have a complex variety of signal intensities in MR images because of the hemorrhage, inflammatory fluids and chipped bony spicules. Therefore, before tracking ESCs in *in vivo* bone injuries, we tracked ESCs in *in vivo* muscle which has a simpler and more homogenous signal intensity in MR images than do bone injuries. In the muscle, MRI was capable of tracking iron-labelled ESCs longitudinally (at day 1 and 7 post-injection). Iron-labelled ESCs were detected as dark hypointense areas in all images. Conversely, Gd-labelled cells were only detected in one cross sectional view at day 1, suggesting that Gd might have limited utility as a label in our model.

Having established that labelled ESCs could be tracked over time in *in vivo* muscle, we introduced them into the *in vivo* bone fracture model. In the *in vivo* bone fracture model, the iron-labelled ESCs were visualized in the MR images as hypointense areas. Using signal intensity (SI) analysis, the iron-labelled ESCs were tracked in bone. However, the SI of the bone fracture and of the surrounding areas is affected by more than the T_2 effect of the implanted iron-labelled cells. An example of one of these additional factors is the dilution of the label upon cell death. This and other factors will be discussed below in Section 9.2.1. All of these other factors must be taken into consideration when using SI analysis to track ESCs in order to avoid misinterpretation.

It was challenging to detect the Gado celltrack-labelled ESCs in our studies probable due to their low detection sensitivity[139,158]. Thus, for our current MRI model system Gado celltrack is not recommended as a T_1 contrast agent for cell labelling, unless further optimized. Given that

this was the first study to investigate Gado celltrack for *in vivo* cell tracking, further studies are needed optimize the cell concentration and the MRI protocol needed for *in vivo* detection of Gado celltrack-labelled cells. The advantage of using Gd-based agents over iron-based ones is that they get rapidly cleared from the circulation[158]. This means that after cell death the Gd does not get phagocytosed by macrophages[158]. This is important because it increases the accuracy of SI interpretation.

Histology and immunohistochemistry protocols were used to study the fate of the implanted cells and of the iron label. Some of the ESCs were found in the newly formed bone and at other sites distant from the site of implantation (Section 8.3.1.4). This suggests that some of the implanted cells integrated into the new bone formed at the site of implantation, while others migrated to other sites. Also, ESCs and macrophage cells were found at the same location, which suggests that some of the implanted cells died and their iron was transferred to macrophages (Section 8.3.2.3).

9.2 Significant findings

This is the first study to develop a non-invasive MRI-based model to track ESC in a bone fracture in live animals. This study presented the foundational steps in developing this model. To develop this model, we optimized the MRI protocol, assessed different contrast agents and biomaterials for their potential use in the model, developed a labelling-differentiation protocol to create implantable, trackable ESCs, and correlated the SI outcomes with histological findings. In the course of developing the model, new information was gained about the outcomes of cell therapies transplanted in the bone fracture. Finally, the model developed in this thesis could be used to track cells in bone injuries and learn about their *in vivo* behaviour.

Summary of findings:

- We optimized an MR protocol for visualizing the mouse bone fracture with high S/N, high resolution, minimal artefacts, and in a reasonable acquisition time (~20 minutes).
- The comparison of MRI and µCT revealed that MRI was capable of imaging the bone fracture like µCT, plus it gave additional information about the implanted soft tissues which was exactly what we needed for our model. Another important advantage of MRI in repeated measure is that it doesn't have ionizing radiation which makes it safe for repeated measurements.
- The *in vitro* MR relaxivity measurement of relatively new contrast agents (Bangs, Ferex, Gado celltrack and Gd-nanoparticles proved that they have enough relaxivity as MRI contrast agents for cell labelling.
- We successfully labelled ESCs with MR detectable doses of contrast agents without adversely affecting the cells. Plus, we were able to detect the Gd- and iron-labelled cells *in vitro*.
- We developed a cell labelling-differentiation protocol and used it to create differentiated implantable and trackable ESCs.
- We tracked iron-labelled cells in muscle and bone.
- We studied that fate and the behaviour of the cells using MRI and IHC. Our data suggested that some of the implanted cells integrated in the host tissue, some migrated away and some died.
- Finally, we development an MR cell tracking model in bone fracture where different cell therapies could be tested longitudinally.

9.3 Important considerations and limitations

9.3.1 Technical considerations

It is common in MR imaging to assess the data qualitatively based on visualizing the cells of interest. The qualitative assessment of iron-labelled cells is based on detecting hypointensities visually. This method was previously used and reported by Hoehn[162], Lepore[75], Lalande[160] , Bulte[10,173], and Walczak[173]. Likewise, we were able to detect the iron-labelled cells in mice muscles and bone injuries as hypointensities (chapter 7 & 8).

Beside the qualitative assessment, there are also quantitative methods to assess the labelled cells in soft tissues *in vivo*[158]. Some of these methods were reported by Baligand and they were based on measuring the number of black pixels cause by the labelled cells against a clear background of soft tissue, measuring the size of the hypointense area caused by the labelled cells, or measuring the contrast at the labelled cells and compare it to the contrast of another distant tissue[158]. In Berman *et al.* study they quantified the iron-labelled cells in mice brain by counting the number of black pixels in the clear background of brain[74]. All these studies were done in soft tissues.

Because cell tracking in bone is a novel protocol and to our knowledge this is the first study to address it, there was no previous quantification method found in the literature to assess the labelled cells in bone. All the studies found were based on cell tracking in soft tissues[10,74,158] which produce higher signal compared to bone. For additional assessment of the data, we decided to apply one of these quantification methods to our model. The most applicable method that we decided to try was measuring the signal at the region of interest (distal hole, proximal hole or bone marrow) and dividing it by the muscle of the mouse. We used ratios instead of absolute values to be able to compare the data across different groups. Our results showed that,

the SI ratio at the distal hole (iron-labelled cells) was significantly lower than the SI ratio at the control hole at day 1, while not significant at day 7 or 14. The method used here is similar to Baligand's method[158]. While not ideal, the SI method is accepted by the MRI scientific community as a method for quantifying labelled cells in soft tissues[128,150,161,174].

In the ideal cell tracking model, the signal changes should allow detection of the labelled cells over the entire time course of tissue to repair, which can take ~40 days in the mouse bone fracture repair[22]. Currently, the length of reliable cell tracking using SI analysis is limited to the amount of time during which most of iron label stays in viable cells. When iron leaves viable cells, it gets transferred to other cells which could not be detected due to the low detection threshold or they can give false positive signal[158]. The time during which accurate SI analyses are possible could be lengthened by developing new contrast agents that are rapidly released from the body after cell death.

Unlike iron-based contrast agents, Gd contrast agents are less likely to be taken by macrophages and produce false positive results. Gd is not taken by macrophages because once it is released from dead cells, it gets rapidly cleared through the kidney[158]. Previous reports showed that SI analysis is more accurate when tracking Gd-labelled cells versus iron-labelled cells[158]. However, due to the low detection sensitivity Gd, it is still unfavourable in cell tracking.

The second technical consideration in using SI analysis is the absence of a linear relationship between the number of labelled stem cells and the SI they generate *in vivo*. This complicates the quantification of the labelled cells *in vivo*. Daldrup-Link *et al.* found no significant correlation between the number of transplanted cells and the MRI SI data[175]. Our *in vitro* results were encouraging because they suggested the presence of a linear relationship between the number of iron-labelled cells and the decrease of the SI (Section 6.3). However this relationship is not

applicable *in vivo* due to the SI misinterpretations (discrepancies) mentioned above. Despite some studies investigating new methods to quantify labelled cells *in vivo*, the *in vivo* quantification of labelled cells remains in an early phase of development[158,176].

9.3.2 Limitations

The MRI-based cell tracking model developed in this thesis shows promise as a tool for testing new cell therapies. However, like any imaging method, MRI has its own limitations in cell tracking that need to be considered. Other limitations, unrelated to MRI, were encountered in the interpretation of tissue fluorescent data due to auto-fluorescing properties of the tissues. Solutions to both types of limitations are suggested below.

MRI limitation. The traumatic injury and bleeding at the site of fracture induction can interfere with the MRI-based visualization of the labelled cells. This limitation was accounted for by using a control group that has the same bone injuries induced into them, and comparing their SI to the treatment group. The second limitation only applies to iron labelling. Iron-labelled ESCs induce hypointense areas that can interfere with the visualization of underlying anatomical structures in MR images. This limitation could be solved by developing new positive contrast agents that have higher relaxivity and detectability than the current ones.

In future experiments, some of these limitations could be overcome by using a dual labelling of positive and negative contrast agent together for cell labelling[134]. This is a relatively new cell labelling approach that was studied by Loai *et al.* in 2012. This approach could overcome the problems associated with the low signal produced by bone and iron-labelled cells[134]. This hyperintensity introduce by the positive contrast agent would not obscure underlying anatomical structures.

Tissue processing limitations. The additional limitation is related to interpreting the fluorescence signal seen in histological sections containing Bangs- and GFP-labelled ESCs. In these sections, auto-fluorescence interfered with the signal from fluorescing cells or particles. Auto-fluorescence is mostly caused by lipofuscins. Lipofuscins come either from natural substances existing in the tissue[177] or from the aldehyde fixative. Both GFP and Bangs, and lipofuscins have very broad and overlapping spectra which makes the detection of the label's signal challenging[177]. In our studies, we used negative controls to determine the amount of signal that was generated by auto-fluorescence. In sections containing fluorescently-labelled ESCs, signal that exceeded the amount seen in the negative controls was interpreted as positive signal.

To avoid fixative-induced auto-fluorescence in future studies, the use of aldehyde fixatives should be avoided. Alternately, the aldehyde fixative should be removed chemically by acid bleaching of the tissue sections after tissue processing[178]. To reduce lipofuscins auto-fluorescence the tissue could be treated with $CuSO_4$ or Sudan Black[177].

9.4 Conclusions

Due to the increasing potential of stem cell therapies and increasing demand to develop new therapies, it is equally important to develop a method to test and monitor these therapies longitudinally. Currently, cell tracking is being extensively investigated and scientists are trying to optimize cell tracking methods[10,63,64,124,125,130,155,156] . An optimal cell tracking model as described by Frangioni *et al.* is one that is non-invasive, biologically safe for the cells and the host[63]. Additionally, the cells should be detected *in vivo* for the term of treatment, and the tracking system should be accurate and only detect viable labelled cells[63]. To date no tracking method fulfills all these point and researchers are continuously attempting to develop this optimal method.

MRI is a robust method for non invasive cell tracking. Despite the limitations of MR in cell tracking (Section 9.3.2), many studies reported significant achievements in this field. Scientists were able to track cells in soft tissues such as; heart[63,64], brain[169], and lymph nodes[10] using MRI. To date no studies tracked cells in bone. This could be due to the complexity of bone imaging using MRI, and its lack of signal which makes it appear dark, consequently, making it challenging to detect labelled cells in bone[78]. Unlike bone imaging, soft tissue provides more signal and appears bright, which enables the detection of tracked cells[10].

Optimizing the MR imaging protocol was a crucial step in developing the cell tracking model. The optimal MR sequence for bone imaging is debatable between GE-and SE-based sequences[78]. Krug compared both sequences in imaging bone and showed that SE-based sequence could be used to image bone and assess its structural parameters[78,179]. Similar to Krug's approach, we compared GE- and SE-based sequences in imaging the bone fracture and the resulted optimized MR protocol was based on SE sequence because the GE had to many susceptibility artifacts at the bone tissue interface.

Additionally, we used an MR Solenoid coil to obtain the best signal to noise ratio S/N, high resolution and minimal imaging artefacts in a reasonable acquisition time (Section 2.2 and Section 2.3). The developed MRI protocol was used for all our *in vivo* bone imaging. It was equally important to determine the MRI capabilities in monitoring biomaterials in bone. To do this we followed Warwick *et al.* approach[45] and we compared the MRI with µCT in assessment of the biomaterials in the bone fracture. Similar to Warwick's finding MRI was capable of imaging bone structures and assessing bone healing. Specifically MRI provided additional information on soft tissue and doesn't have ionizing radiation—making it safe for repeated measurements.

Another important factor in developing the cell tracking model was the selection of a contrast agent. We compared Gd- and iron-based contrast agents, the most commonly used contrast agents in the field of cell tracking[111,125,129,134,148,154,175,180]. The criteria of comparison were the relaxivity, the health of labelled cells and their *in vivo* detectability. In our *in vitro* work (chapter 5 & 6), the contrast agent relaxivity and effect on cell viability were extensively investigated and the results showed that both contrast agents groups had sufficient relaxivity for MR imaging plus it showed that they did not adversely affect the cells. These findings are in agreement with Baligand's *in vitro* reports on labelled myoblasts where he showed that appropriate doses for labelling were not toxic to the cells[158]. As in my study, he showed that both contrast agents have sufficient relaxivity for *in vivo* detection in skeletal muscle.[158]

Using information from the in vitro studies, we tested Gd- and iron-based contrast agents *in vivo* (Chapter 7 & 8). We found that iron-labelled cells were clearly detected in muscle (~ 10,000 cells) and bone (~2 x 10^4 cell) as hypointensities, however Gd-labelled cells were difficult to detect in both tissues. A similar comparison was carried out by Baligand *et al.*, where he transplanted (~2 x 10^6) Gd-labelled myoblasts or (~2 x 10^6) iron-labelled myoblasts in mice muscles[158]. Baligand found that Gd-labelled cells appeared as hypointense area while iron-labelled cells appeared as a hypointense area[158]. Our findings about iron-labelled cells were similar to Baligand's findings. Conversely, the Gd-labelled cells were in contrast with his finding. This could be because Gd has lower detection sensitivity than iron[158] and thus to visualize the cells *in vivo* higher number of cells was needed. Given the limited capacity of the size of our bone fracture, we could not increase the number of Gd implanted cells. These findings were more in favour of using iron labelled cells than Gd-labelled cells for our model.

Our *in vivo* tracking model was able to detect the iron-labelled cells at the site of implantation in bone fracture. This was evidenced by our results where MR signal changes corresponded to the locations of the Y-chromosome positive cells. Because MR cell tracking in bone is a novel area in research, we could not find any reported results about cell tracking in bone. The only relevant study, was done by Lalande *et al.*, where he differentiated adipose derived stem cells to osteogenic lineage, put them in a 3D scaffold then transplanted them subcutaneously in mice[160]. His results showed that he could track the cells and their migration out of the scaffold. Yet, these results were not obtained from imaging in real bone. Our model is more complex as due to lack of signal in bone and gradient artifacts caused by the bone/tissue interface.

Many studies reported the capability of MR in detecting cell migration[160,162,169]. Based on our results, our cell tracking model was capable of tracking ESCs migration from the site of implantation to the bone marrow and the control fracture site (Section 8.5). When we redid the study using GFP-ESC's there did not appear to be migration to the control fracture site. This could be due to the presence of the GFP gene which might have affected the migratory signalling pathways of the cells or increased their death rate after labelling.

We did not detect labelled macrophages (labelled by the iron release from dead implanted labelled cells) using MRI. This finding is in contrast with most studies in the literature which reports that the transfer of label to macrophages gives false positive results[69,156,158]. However, Berman *et al.* it reported that macrophages labelled by iron transferred from dead cells had lower detectability than the transplanted labelled cells[74]. As histology on serial sections provided supportive evidence for iron within macrophages, it is possible that upon cell death the label gets phagocytosed by macrophages at doses below the MR detection limit[74]. This suggests that our

MR method tracked the cells as long as they were viable and carrying the iron, but once they died, releasing their iron to macrophages, nothing was detected. This is important in monitoring new cell therapies where false positive obtained from dead cells or labelled macrophages could be misleading.

Based on our work using MRI and IHC, the implanted cells showed three patterns of response; some cells migrated away from the site of implantation, others integrated in the new bone, and lastly some cells died and their iron was phagocytosed by macrophages (Section 8.4). A previous study used comparable IHC and MRI protocols to study the *in vivo* behaviour of embryonic stem cells in brain and reported that cells migrated away from the site of transplantation[162]. Cell migration was also reported by Guzman where he proved that neural stem cell migrated in the brain tissue after transplantation[169]. Aside from cell migration, cell integration into the host tissue was reported by Taiani *et al.* after they transplanted dESCs in a bony defect[30]. Finally, several studies reported partial cell death of cells after transplantation and subsequent transfer of iron to macrophages[69,158].

Overall, we described the development of a novel cell tracking model and we used this to track labelled cells in a bone fracture model successfully. Moreover, we detected dESCs migration from the implantation site to the bone marrow and the control fracture site. At the same time, the labeling method did not adversely affect the cells. The novelty in our model is the ability to track cells in bone.

9.5 Future directions

The experiments presented in this thesis were a part of a much bigger project aimed at developing the use of stem cells for healing bone in a bone fracture model. One future direction of this work is to be used to test new cell therapies in bone *in vivo*. Future experiments would

also use knowledge about the behaviour of implanted ESCs *in vivo* to improve our understanding about the current MR tracking model.

References

1. Group COCS. Canadian institute of Health Research 2010.
2. Report PHAoC. Public Health Agency of Canada Report. Canadian institute of Health Research 2000.
3. Errico TJ. Lumbar disc arthroplasty. Clin Orthop Relat Res 2005(435):106-117.
4. Dupont KM, Sharma K, Stevens HY, Boerckel JD, Garcia AJ, Guldberg RE. Human stem cell delivery for treatment of large segmental bone defects. Proc Natl Acad Sci U S A 2010;107(8):3305-3310.
5. Taiani JT, Krawetz RJ, Zur Nieden NI, et al. Reduced differentiation efficiency of murine embryonic stem cells in stirred suspension bioreactors. Stem Cells Dev 2009;19(7):989-998.
6. Liang H WK, Shimer AL, Li X, Balian G, Shen FH. Use of a bioactive scaffold for the repair of bone defects in a novel reproducible vertebral body defect model. Bone 2010;47(2):197-204.
7. Swetha M, Sahithi K, Moorthi A, Srinivasan N, Ramasamy K, Selvamurugan N. Biocomposites containing natural polymers and hydroxyapatite for bone tissue engineering. Int J Biol Macromol 2010;47(1):1-4.
8. Dalkyz M, Ozcan A, Yapar M, Gokay N, Yuncu M. Evaluation of the effects of different biomaterials on bone defects. Implant Dent 2000;9(3):226-235.
9. Wang G, Mostafa NZ, Incani V, Kucharski C, Uludag H. Bisphosphonate-decorated lipid nanoparticles designed as drug carriers for bone diseases. J Biomed Mater Res A 2012;100(3):684-693.
10. Bulte JW. In vivo MRI cell tracking: clinical studies. AJR Am J Roentgenol 2009;193(2):314-325.
11. Walter J Rogers CHMaCMK. Technology Insight: in vivo cell tracking by use of MRI. Nature Clinical Practice Cardiovascular Medicine 2006;3(554-562).
12. Sun C, Lee JS, Zhang M. Magnetic nanoparticles in MR imaging and drug delivery. Adv Drug Deliv Rev 2008;60(11):1252-1265.
13. Deev RV, Tsupkina NV, Gololobov VG, et al. The influence of transplanted culture of bone marrow stromal cells on reparative osteohistogenesis in parietal bone defect. Tsitologiia 2008;50(4):293-301.
14. Undale A, Fraser D, Hefferan T, et al. Induction of fracture repair by mesenchymal cells derived from human embryonic stem cells or bone marrow. J Orthop Res 2011;29(12):1804-1811.
15. Khurana J. Bone pathology. 2009.
16. Bernstein J. Musculoskeletal medicine. Rosemont, Ill : American Academy of Orthopaedic Surgeons, ©2003 2003.
17. Day TF, Guo X, Garrett-Beal L, Yang Y. Wnt/beta-catenin signaling in mesenchymal progenitors controls osteoblast and chondrocyte differentiation during vertebrate skeletogenesis. Dev Cell 2005;8(5):739-750.
18. Victor Hirsch Frankel MN. Basic biomechanics of the skeletal system. Henry Kimpton publisher 1980.
19. Einhorn TA. Clinically applied models of bone regeneration in tissue engineering research. Clin Orthop Relat Res 1999(367 Suppl):S59-67.

20. Einhorn TA. The cell and molecular biology of fracture healing. Clin Orthop Relat Res 1998(355 Suppl):S7-21.
21. Saban J, Zussman MA, Havey R, Patwardhan AG, Schneider GB, King D. Heterozygous oim mice exhibit a mild form of osteogenesis imperfecta. Bone 1996;19(6):575-579.
22. Uusitalo H, Rantakokko J, Ahonen M, et al. A metaphyseal defect model of the femur for studies of murine bone healing. Bone 2001;28(4):423-429.
23. B Bak KJ. Standardization of tibial fractures in the rat. Bone 1992;13:289-295.
24. Bonnarens F, Einhorn TA. Production of a standard closed fracture in laboratory animal bone. J Orthop Res 1984;2(1):97-101.
25. Greiff J. A method for the production of an undisplaced reproducible tibial fracture in the rat. Injury 1978;9(4):278-281.
26. Hiltunen A, Vuorio E, Aro HT. A standardized experimental fracture in the mouse tibia. J Orthop Res 1993;11(2):305-312.
27. Taha MA, Manske SL, Kristensen E, et al. Assessment of the efficacy of MRI for detection of changes in bone morphology in a mouse model of bone injury. J Magn Reson Imaging 2012;38(1):231-237.
28. An Y, Friedman RJ, Parent T, Draughn RA. Production of a standard closed fracture in the rat tibia. J Orthop Trauma 1994;8(2):111-115.
29. Taiani JT, Krawetz RJ, Yamashita A, et al. Embryonic stem cells incorporate into newly formed bone and do not form tumors in an immunocompetent mouse fracture model. Cell Transplant;22(8):1453-1462.
30. Taiani JTK, Roman J.; Yamashita, Akihiro; Pauchard, Yves; Buie, Helen R.; Ponjevic, Dragana; Boyd, Steven K.; Rancourt, Derrick E.; Matyas, John R. Embryonic stem cells incorporate into newly formed bone and do not form tumors in an immunocompetent mouse fracture model. Cell Transplantation 2013;22.
31. Cook MJ. The Anatomy of the Laboratory Mouse. Academic press 1965.
32. Arvidson K, Abdallah BM, Applegate LA, et al. Bone regeneration and stem cells. J Cell Mol Med 2010;15(4):718-746.
33. Usas A, Ho AM, Cooper GM, Olshanski A, Peng H, Huard J. Bone regeneration mediated by BMP4-expressing muscle-derived stem cells Is affected by delivery system. Tissue Engineering Part A 2008;15(2):285-293.
34. Deev RV, Tsupkina NV, Gololobov VG, et al. The influence of transplanted culture of bone marrow stromal cells on reparative osteohistogenesis in parietal bone defect. Tsitologiia 2008;50(4):293.
35. Basile L, Pignatello R, Passirani C. Active targeting strategies for anticancer drug nanocarriers. Curr Drug Deliv 2012;9(3):255-268.
36. Waese EY, Kandel RA, Stanford WL. Application of stem cells in bone repair. Skeletal Radiol 2008;37(7):601-608.
37. Bruder SP, Fox BS. Tissue engineering of bone. Cell based strategies. Clin Orthop Relat Res 1999(367 Suppl):S68-83.
38. Cancedda R, Bianchi G, Derubeis A, Quarto R. Cell therapy for bone disease: a review of current status. Stem Cells 2003;21(5):610-619.
39. Aicher WK, Buhring HJ, Hart M, Rolauffs B, Badke A, Klein G. Regeneration of cartilage and bone by defined subsets of mesenchymal stromal cells-Potential and pitfalls. Adv Drug Deliv Rev 2010;63(4-5):342-351.

40. Thomson JA, Itskovitz-Eldor J, Shapiro SS, et al. Embryonic stem cell lines derived from human blastocysts. Science 1998;282(5391):1145-1147.
41. Evans MJ, Kaufman MH. Establishment in culture of pluripotential cells from mouse embryos. Nature 1981;292(5819):154-156.
42. Bielby RC, Boccaccini AR, Polak JM, Buttery LD. In vitro differentiation and in vivo mineralization of osteogenic cells derived from human embryonic stem cells. Tissue Eng 2004;10(9-10):1518-1525.
43. Wakitani S, Takaoka K, Hattori T, et al. Embryonic stem cells injected into the mouse knee joint form teratomas and subsequently destroy the joint. Rheumatology (Oxford) 2003;42(1):162-165.
44. Krawetz RJ, Taiani JT, Wu YE, et al. Collagen I scaffolds cross-linked with beta-glycerol phosphate induce osteogenic differentiation of embryonic stem cells in vitro and regulate their tumorigenic potential in vivo. Tissue Eng Part A 2011;18(9-10):1014-1024.
45. Warwick R, Willatt JM, Singhal B, Borremans J, Meagher T. Comparison of computed tomographic and magnetic resonance imaging in fracture healing after spinal injury. Spinal Cord 2009;47(12):874-877.
46. Techawiboonwong A, Song HK, Leonard MB, Wehrli FW. Cortical bone water: in vivo quantification with ultrashort echo-time MR imaging. Radiology 2008;248(3):824-833.
47. Beaman FD, Bancroft LW, Peterson JJ, Kransdorf MJ, Menke DM, DeOrio JK. Imaging characteristics of bone graft materials. Radiographics 2006;26(2):373-388.
48. Donald Mcrobbie EM, Martin Graves and Martin Prince. MRI from picture to proton 2007.
49. Filler A. The History, Development and Impact of Computed Imaging in Neurological Diagnosis and Neurosurgery: CT, MRI, and DTI. The Internet Journal of Neurosurgery 2009;7(1).
50. Damadian R. Tumor detection by nuclear magnetic resonance. Science 1971;171(3976):1151-1153.
51. Lauterbur PC. Image formation by induced local interactions. Examples employing nuclear magnetic resonance. 1973. Clin Orthop Relat Res 1989(244):3-6.
52. Dawson J. Paul Lauterbur and the Invention of MRI; 2013.
53. Adrian M. K. Thomas AKB, Uwe Busch. Classic Papers In Modern Diagnostic Radiology; 2005.
54. Hornak JP. The basics of MRI. 1996-2014.
55. Nishimura D. Principals of Magnetic Resonance Imaging. 1994.
56. Armfield DR, Towers JD, Robertson DD. Radiographic and MR imaging of the athletic hip. Clin Sports Med 2006;25(2):211-239, viii.
57. Brukner P, Bennell K. Stress fractures in female athletes. Diagnosis, management and rehabilitation. Sports Med 1997;24(6):419-429.
58. Kiuru MJ, Pihlajamaki HK, Hietanen HJ, Ahovuo JA. MR imaging, bone scintigraphy, and radiography in bone stress injuries of the pelvis and the lower extremity. Acta Radiol 2002;43(2):207-212.
59. Llopis E, Fernandez E, Cerezal L. MR and CT arthrography of the hip. Semin Musculoskelet Radiol 2012;16(1):42-56.

60. Anumula S, Wehrli SL, Magland J, Wright AC, Wehrli FW. Ultra-short echo-time MRI detects changes in bone mineralization and water content in OVX rat bone in response to alendronate treatment. Bone 2010;46(5):1391-1399.
61. Horch RA, Gochberg DF, Nyman JS, Does MD. Non-invasive predictors of human cortical bone mechanical properties: T(2)-discriminated H NMR compared with high resolution X-ray. PLoS One 2011;6(1):e16359.
62. Krug R, Stehling C, Kelley DAC, Majumdar S, Link TM. Imaging of the musculoskeletal system in vivo using ultra-high field magnetic resonance at 7 T. Investigative radiology 2009;44(9):613.
63. Frangioni JV, Hajjar RJ. In vivo tracking of stem cells for clinical trials in cardiovascular disease. Circulation 2004;110(21):3378-3383.
64. Azene N, Fu Y, Maurer J, Kraitchman DL. Tracking of stem cells in vivo for cardiovascular applications. J Cardiovasc Magn Reson 2014;16(1):7.
65. Contag CH, Jenkins D, Contag PR, Negrin RS. Use of reporter genes for optical measurements of neoplastic disease in vivo. Neoplasia 2000;2(1-2):41-52.
66. Joo SY, Cho KA, Jung YJ, et al. Bioimaging for the monitoring of the in vivo distribution of infused mesenchymal stem cells in a mouse model of the graft-versus-host reaction. Cell Biol Int 2010;35(4):417-421.
67. Villa C, Erratico S, Razini P, et al. In vivo tracking of stem cell by nanotechnologies: future prospects for mouse to human translation. Tissue Eng Part B Rev 2010;17(1):1-11.
68. Zaheer A, Lenkinski RE, Mahmood A, Jones AG, Cantley LC, Frangioni JV. In vivo near-infrared fluorescence imaging of osteoblastic activity. Nat Biotechnol 2001;19(12):1148-1154.
69. Hawrylak N, Ghosh P, Broadus J, Schlueter C, Greenough WT, Lauterbur PC. Nuclear magnetic resonance (NMR) imaging of iron oxide-labeled neural transplants. Exp Neurol 1993;121(2):181-192.
70. Bulte JW, Douglas T, Witwer B, et al. Magnetodendrimers allow endosomal magnetic labeling and in vivo tracking of stem cells. Nat Biotechnol 2001;19(12):1141-1147.
71. Jing Y, Mal N, Williams PS, et al. Quantitative intracellular magnetic nanoparticle uptake measured by live cell magnetophoresis. FASEB J 2008;22(12):4239-4247.
72. Taiani J, Krawetz RJ, Nieden N, et al. Reduced differentiation efficiency of murine embryonic stem cells in stirred suspension bioreactors. Stem Cells and Development 2009(ja).
73. Wang YX. Superparamagnetic iron oxide based MRI contrast agents: Current status of clinical application. Quant Imaging Med Surg 2012;1(1):35-40.
74. Stacey Cromer Berman, Chulani Galpoththawela, Assaf A. Gilad, Jeff W. M. Bulte, Walcza aP. Long-Term MR Cell Tracking of Neural Stem Cells Grafted in Immunocompetent Versus Immunodeficient Mice Reveals Distinct Differences in Contrast Between Live and Dead Cells. Magnetic resonance in medicine 2011;65:564–574.
75. Lepore AC, Walczak P, Rao MS, Fischer I, Bulte JW. MR imaging of lineage-restricted neural precursors following transplantation into the adult spinal cord. Exp Neurol 2006;201(1):49-59.
76. Liney G. MRI from A to Z. 2011:2nd ed. 2011.

77. Jung BA, Weigel M. Spin echo magnetic resonance imaging. J Magn Reson Imaging 2013;37(4):805-817.
78. Krug R, Stehling C, Kelley DA, Majumdar S, Link TM. Imaging of the musculoskeletal system in vivo using ultra-high field magnetic resonance at 7 T. Invest Radiol 2009;44(9):613-618.
79. Scheffler K, Hennig J. T(1) quantification with inversion recovery TrueFISP. Magn Reson Med 2001;45(4):720-723.
80. Schmitt P, Griswold MA, Jakob PM, et al. Inversion recovery TrueFISP: quantification of T(1), T(2), and spin density. Magn Reson Med 2004;51(4):661-667.
81. Frank JA, Miller BR, Arbab AS, et al. Clinically applicable labeling of mammalian and stem cells by combining superparamagnetic iron oxides and transfection agents. Radiology 2003;228(2):480-487.
82. Hoult DI, Chen CN, Sank VJ. Quadrature detection in the laboratory frame. Magn Reson Med 1984;1(3):339-353.
83. Hornak JP, Szumowski J, Bryant RG. Elementary single turn solenoids used as the transmitter and receiver in magnetic resonance imaging. Magn Reson Imaging 1987;5(3):233-237.
84. Hidalgo SS, Jirak D, Solis E, Rodriguez AO. Solenoid coil for mouse-model MRI with a clinical 3-Tesla imager: body imaging. Revista Mexicana de Física 2009;55(002).
85. Taiani JT, Krawetz RJ, Zur Nieden NI, et al. Reduced differentiation efficiency of murine embryonic stem cells in stirred suspension bioreactors. Stem Cells Dev 2010;19(7):989-998.
86. Uusitalo H, Rantakokko J, Ahonen M, et al. A metaphyseal defect model of the femur for studies of murine bone healing. Bone 2001;28(4):423-429.
87. Gaetke-Udager K, Girish G, Kaza RK, et al. MR imaging of the pelvis: a guide to incidental musculoskeletal findings for abdominal radiologists. Abdom Imaging 2014.
88. A Haase, J Frahm, D Matthaei, W Hanicke, Merboldt K-D. FLASH imaging. Rapid NMR imaging using low flip-angle pulses Journal of Magnetic Resonance Imaging 1969; 67(2):258–266.
89. Haacke EM, Xu Y, Cheng YC, Reichenbach JR. Susceptibility weighted imaging (SWI). Magn Reson Med 2004;52(3):612-618.
90. Haacke EM. Susceptibility weighted imaging (SWI). Z Med Phys 2006;16(4):237.
91. de Souza JM, Domingues RC, Cruz LC, Jr., Domingues FS, Iasbeck T, Gasparetto EL. Susceptibility-weighted imaging for the evaluation of patients with familial cerebral cavernous malformations: a comparison with t2-weighted fast spin-echo and gradient-echo sequences. AJNR Am J Neuroradiol 2008;29(1):154-158.
92. Chamberlain RM. Novel Magnetic Resonance Imaging Using Frequency Swept Pulses. ProQuest 2008.
93. Miles JD, Weinhold P, Brimmo O, Dahners L. Rat tibial osteotomy model providing a range of normal to impaired healing. J Orthop Res 2010;29(1):109-115.
94. Jones AC, Arns CH, Sheppard AP, Hutmacher DW, Milthorpe BK, Knackstedt MA. Assessment of bone ingrowth into porous biomaterials using MICRO-CT. Biomaterials 2007;28(15):2491-2504.

95. Klinck RJ, Campbell GM, Boyd SK. Radiation effects on bone architecture in mice and rats resulting from in vivo micro-computed tomography scanning. Med Eng Phys 2008;30(7):888-895.
96. Monfoulet L, Rabier B, Chassande O, Fricain JC. Drilled Hole Defects in Mouse Femur as Models of Intramembranous Cortical and Cancellous Bone Regeneration. Calcified Tissue International 2009;86(1):72-81.
97. Sellgren KL, Ma T. Perfusion conditioning of hydroxyapatite-chitosan-gelatin scaffolds for bone tissue regeneration from human mesenchymal stem cells. J Tissue Eng Regen Med 2011.
98. Nandi SK, Roy S, Mukherjee P, Kundu B, De DK, Basu D. Orthopaedic applications of bone graft & graft substitutes: a review. Indian J Med Res 2010;132:15-30.
99. Yamashita A, Krawetz R, Rancourt DE. Loss of discordant cells during micro-mass differentiation of embryonic stem cells into the chondrocyte lineage. Cell Death Differ 2009;16(2):278-286.
100. Martin M, Lemaire C, Tatton WG, Armstrong RL, Struk R. The center-tapped slotted tube autotransformer resonator: a coil for use with a high-resolution small animal imaging system. Magn Reson Med 1988;8(2):171-179.
101. Benabdallah N, Benahmed N, Benyoucef B, Bouhmidi R, Khelif M. Electromagnetic analysis of the slotted-tube resonator with a circular cross section for MRI applications. Phys Med Biol 2007;52(16):4943-4952.
102. Daldrup-Link HE, Henning T, Link TM. MR imaging of therapy-induced changes of bone marrow. Eur Radiol 2007;17(3):743-761.
103. Low G RN. Can follow-up radiography for acute scaphoid fracture still be considered a valid investigation? clin Radiol 2005;60(10):1106-10.
104. Warwick R, Willatt JM, Singhal B, Borremans J, Meagher T. Comparison of computed tomographic and magnetic resonance imaging in fracture healing after spinal injury. Spinal Cord 2009;47(12):874-877.
105. Cui Q, Xiao Z, Li X, Saleh KJ, Balian G. Use of genetically engineered bone-marrow stem cells to treat femoral defects: An experimental study. The Journal of Bone and Joint Surgery 2006;88(Supplement 3):167.
106. Dalkýz M, Özcan A, Yapar M, Gökay N, Yüncü M. Evaluation of the effects of different biomaterials on bone defects. Implant Dentistry 2000;9(3):226-235.
107. Laasonen EM, Kyrö A, Korhola O, Böstman O. Magnetic resonance imaging of tibial shaft fracture repair. Archives of Orthopaedic and Trauma Surgery 1989;108(1):40-43.
108. Alanen A. Magnetic resonance imaging of hematomas in a 0.02 T magnetic field. Acta radiologica: diagnosis 1986;27(5):589.
109. Kubo T, Shiga T, Hashimoto J, et al. Osteoporosis influences the late period of fracture healing in a rat model prepared by ovariectomy and low calcium diet. J Steroid Biochem Mol Biol 1999;68(5-6):197-202.
110. Andreozzi E, Wang P, Valenzuela A, et al. Size-stable solid lipid nanoparticles loaded with Gd-DOTA for magnetic resonance imaging. Bioconjug Chem 2013;24(9):1455-1467.
111. Guenoun J, Koning GA, Doeswijk G, et al. Cationic Gd-DTPA liposomes for highly efficient labeling of mesenchymal stem cells and cell tracking with MRI. Cell Transplant 2011;21(1):191-205.

112. Panahifar A, Mahmoudi M, Doschak MR. Synthesis and in vitro evaluation of bone-seeking superparamagnetic iron oxide nanoparticles as contrast agents for imaging bone metabolic activity. ACS Appl Mater Interfaces 2013;5(11):5219-5226.
113. Wang G, Babadagli ME, Uludag H. Bisphosphonate-derivatized liposomes to control drug release from collagen/hydroxyapatite scaffolds. Mol Pharm 2011;8(4):1025-1034.
114. Vitha T, Kubicek V, Kotek J, et al. Gd(iii) complex of a monophosphinate-bis(phosphonate) DOTA analogue with a high relaxivity; Lanthanide(iii) complexes for imaging and radiotherapy of calcified tissues. Dalton Trans 2009(17):3204-3214.
115. Adzamli IK, Blau M. Phosphonate-modified GdDTPA complexes. I. NMRD study of the solution behavior of new tissue-specific contrast agents. Magn Reson Med 1991;17(1):141-148.
116. Vitha T, Kubicek V, Hermann P, et al. Lanthanide(III) complexes of bis(phosphonate) monoamide analogues of DOTA: bone-seeking agents for imaging and therapy. J Med Chem 2008;51(3):677-683.
117. Sandiford L, Phinikaridou A, Protti A, et al. Bisphosphonate-anchored PEGylation and radiolabeling of superparamagnetic iron oxide: long-circulating nanoparticles for in vivo multimodal (T1 MRI-SPECT) imaging. ACS Nano 2012;7(1):500-512.
118. Tofts P. Quantitative MRI of the Brain: Measuring Changes Caused by Disease. John Wiley & Sons, Ltd 2004.
119. Gmbh BBM. 2012.
120. Lee MJ, Kim MJ, Yoon CS, Song SY, Park K, Kim WS. The T2-shortening effect of gadolinium and the optimal conditions for maximizing the CNR for evaluating the biliary system: a phantom study. Korean J Radiol 2011;12(3):358-364.
121. Kuperman VY, Alley MT. Differentiation between the effects of T1 and T2* shortening in contrast-enhanced MRI of the breast. J Magn Reson Imaging 1999;9(2):172-176.
122. Ladd DL, Hollister R, Peng X, et al. Polymeric gadolinium chelate magnetic resonance imaging contrast agents: design, synthesis, and properties. Bioconjug Chem 1999;10(3):361-370.
123. Chia-Ying Liu PV, Gerald M. Pohost, Krishna S. Nayak. Studies of Gd-DTPA Relaxivity in Different Tissue Models at 3T. 2005.
124. Ahrens ET, Flores R, Xu H, Morel PA. In vivo imaging platform for tracking immunotherapeutic cells. Nat Biotechnol 2005;23(8):983-987.
125. Bulte JW, Duncan ID, Frank JA. In vivo magnetic resonance tracking of magnetically labeled cells after transplantation. J Cereb Blood Flow Metab 2002;22(8):899-907.
126. Himes N, Min JY, Lee R, et al. In vivo MRI of embryonic stem cells in a mouse model of myocardial infarction. Magn Reson Med 2004;52(5):1214-1219.
127. Riviere C, Boudghene FP, Gazeau F, et al. Iron oxide nanoparticle-labeled rat smooth muscle cells: cardiac MR imaging for cell graft monitoring and quantitation. Radiology 2005;235(3):959-967.
128. Chavhan GB, Babyn PS, Thomas B, Shroff MM, Haacke EM. Principles, techniques, and applications of T2*-based MR imaging and its special applications. Radiographics 2009;29(5):1433-1449.
129. Arbab AS, Wilson LB, Ashari P, Jordan EK, Lewis BK, Frank JA. A model of lysosomal metabolism of dextran coated superparamagnetic iron oxide (SPIO) nanoparticles:

implications for cellular magnetic resonance imaging. NMR Biomed 2005;18(6):383-389.
130. Cromer Berman SM, Walczak P, Bulte JW. Tracking stem cells using magnetic nanoparticles. Wiley Interdiscip Rev Nanomed Nanobiotechnol 2011;3(4):343-355.
131. Henriques C, Henriques-Pons A, Meuser-Batista M, Ribeiro AS, de Souza W. In vivo imaging of mice infected with bioluminescent Trypanosoma cruzi unveils novel sites of infection. Parasit Vectors 2014;7:89.
132. Aulanier AL, Doiron AL, Shepherd RD, Rinker KD, Frayne R, Andersen LB. A human cell model for dynamic testing of MR contrast agents. Biotechniques 2011;50(2):120-123.
133. Loai Y, Sakib N, Janik R, Foltz WD, Cheng HL. Human aortic endothelial cell labeling with positive contrast gadolinium oxide nanoparticles for cellular magnetic resonance imaging at 7 Tesla. Mol Imaging 2012;11(2):166-175.
134. Loai Y, Ganesh T, Cheng HL. Concurrent dual contrast for cellular magnetic resonance imaging using gadolinium oxide and iron oxide nanoparticles. Int J Mol Imaging 2012;2012:230942.
135. Hinds KA, Hill JM, Shapiro EM, et al. Highly efficient endosomal labeling of progenitor and stem cells with large magnetic particles allows magnetic resonance imaging of single cells. Blood 2003;102(3):867-872.
136. Fatouros PP, Corwin FD, Chen ZJ, et al. In vitro and in vivo imaging studies of a new endohedral metallofullerene nanoparticle. Radiology 2006;240(3):756-764.
137. Bulte JW, Kraitchman DL, Mackay AM, Pittenger MF. Chondrogenic differentiation of mesenchymal stem cells is inhibited after magnetic labeling with ferumoxides. Blood 2004;104(10):3410-3412; author reply 3412-3413.
138. Bulte JW, Ma LD, Magin RL, et al. Selective MR imaging of labeled human peripheral blood mononuclear cells by liposome mediated incorporation of dextran-magnetite particles. Magn Reson Med 1993;29(1):32-37.
139. Kalish H, Arbab AS, Miller BR, et al. Combination of transfection agents and magnetic resonance contrast agents for cellular imaging: relationship between relaxivities, electrostatic forces, and chemical composition. Magn Reson Med 2003;50(2):275-282.
140. Barrefelt A, Saghafian M, Kuiper R, et al. Biodistribution, kinetics, and biological fate of SPION microbubbles in the rat. Int J Nanomedicine 2013;8:3241-3254.
141. Harisinghani MG, Barentsz J, Hahn PF, et al. Noninvasive detection of clinically occult lymph-node metastases in prostate cancer. N Engl J Med 2003;348(25):2491-2499.
142. Genant HK, Engelke K, Fuerst T, et al. Noninvasive assessment of bone mineral and structure: state of the art. J Bone Miner Res 1996;11(6):707-730.
143. Gordana Vunjak-Novakovic RIF. Culture of Cells for Tissue Engineering. 2006.
144. Sheehan D. HB. Theory and practice of histotechnology. 2nd ed; Battelle Press: Ohio 1980:p 217-218.
145. Parmley RT, Spicer SS, Alvarez CJ. Ultrastructural localization of nonheme celluar iron with ferrocyanide. J Histochem Cytochem 1978;26(9):729-741.
146. Robert I. Handin SEL, Thomas P. Stossel. Principles and Practice of Hematology; 2003. 2304 p.
147. Gomori G. Microtechnical Demonstration of Iron: A Criticism of its Methods. Am J Pathol 1936;12(5):655-664 651.

148. Cunningham CH, Arai T, Yang PC, McConnell MV, Pauly JM, Conolly SM. Positive contrast magnetic resonance imaging of cells labeled with magnetic nanoparticles. Magn Reson Med 2005;53(5):999-1005.
149. Grigoriadis AE, Kennedy M, Bozec A, et al. Directed differentiation of hematopoietic precursors and functional osteoclasts from human ES and iPS cells. Blood 2010;115(14):2769-2776.
150. Argyropoulou MI, Astrakas L. MRI evaluation of tissue iron burden in patients with beta-thalassaemia major. Pediatr Radiol 2007;37(12):1191-1200; quiz 1308-1199.
151. Wiginton1 CD, Kelly2 B, Aytekin Oto3, et al. Gadolinium-Based Contrast Exposure, Nephrogenic Systemic Fibrosis, and Gadolinium Detection in Tissue. MR imaging 2007(DOI:10.2214/AJR.07.2822).
152. Santin G, Paulis M, Vezzoni P, Pacchiana G, Bottiroli G, Croce AC. Autofluorescence properties of murine embryonic stem cells during spontaneous differentiation phases. Lasers Surg Med 2013;45(9):597-607.
153. Arbab AS, Bashaw LA, Miller BR, et al. Characterization of biophysical and metabolic properties of cells labeled with superparamagnetic iron oxide nanoparticles and transfection agent for cellular MR imaging. Radiology 2003;229(3):838-846.
154. Bulte JW, Zhang S, van Gelderen P, et al. Neurotransplantation of magnetically labeled oligodendrocyte progenitors: magnetic resonance tracking of cell migration and myelination. Proc Natl Acad Sci U S A 1999;96(26):15256-15261.
155. Adamczak J, Hoehn M. In vivo imaging of cell transplants in experimental ischemia. Prog Brain Res 2012;201:55-78.
156. Cahill KS, Gaidosh G, Huard J, Silver X, Byrne BJ, Walter GA. Noninvasive monitoring and tracking of muscle stem cell transplants. Transplantation 2004;78(11):1626-1633.
157. Aicher WK, Buhring HJ, Hart M, Rolauffs B, Badke A, Klein G. Regeneration of cartilage and bone by defined subsets of mesenchymal stromal cells--potential and pitfalls. Adv Drug Deliv Rev 2010;63(4-5):342-351.
158. Baligand C, Vauchez K, Fiszman M, Vilquin JT, Carlier PG. Discrepancies between the fate of myoblast xenograft in mouse leg muscle and NMR label persistency after loading with Gd-DTPA or SPIOs. Gene Ther 2009;16(6):734-745.
159. M. López-Lagunaa AS-D, L. Rafael Ramos-Pascuab, J.A. Rodríguez-Altónaga-Martínezc, J. Ramos-Carroa, P. de la Puente Garcíaa, J.J. Vázquez-Reyeroa, J.Á. Santos-Sánchezd, F.J. Iglesias-Muñoza. Labelling of Adipose Derived Mesenchymal Stem Cells for Cell Tracking Using MRI in Bone Tissue Engineering. 2011;55(5):369-377.
160. Lalande C, Miraux S, Derkaoui SM, et al. Magnetic resonance imaging tracking of human adipose derived stromal cells within three-dimensional scaffolds for bone tissue engineering. Eur Cell Mater 2011;21:341-354.
161. Gandon Y, Guyader D, Heautot JF, et al. Hemochromatosis: diagnosis and quantification of liver iron with gradient-echo MR imaging. Radiology 1994;193(2):533-538.
162. Hoehn M, Kustermann E, Blunk J, et al. Monitoring of implanted stem cell migration in vivo: a highly resolved in vivo magnetic resonance imaging investigation of experimental stroke in rat. Proc Natl Acad Sci U S A 2002;99(25):16267-16272.
163. Alers JC, Krijtenburg PJ, Vissers KJ, van Dekken H. Effect of bone decalcification procedures on DNA in situ hybridization and comparative genomic hybridization. EDTA

is highly preferable to a routinely used acid decalcifier. J Histochem Cytochem 1999;47(5):703-710.
164. Austyn JM, Gordon S. F4/80, a monoclonal antibody directed specifically against the mouse macrophage. Eur J Immunol 1981;11(10):805-815.
165. Kostura L, Kraitchman DL, Mackay AM, Pittenger MF, Bulte JW. Feridex labeling of mesenchymal stem cells inhibits chondrogenesis but not adipogenesis or osteogenesis. NMR Biomed 2004;17(7):513-517.
166. Li Z, Suzuki Y, Huang M, et al. Comparison of reporter gene and iron particle labeling for tracking fate of human embryonic stem cells and differentiated endothelial cells in living subjects. Stem Cells 2008;26(4):864-873.
167. Wu X, Hu J, Zhou L, et al. In vivo tracking of superparamagnetic iron oxide nanoparticle-labeled mesenchymal stem cell tropism to malignant gliomas using magnetic resonance imaging. Laboratory investigation. J Neurosurg 2008;108(2):320-329.
168. Chen YC, Hsiao JK, Liu HM, et al. The inhibitory effect of superparamagnetic iron oxide nanoparticle (Ferucarbotran) on osteogenic differentiation and its signaling mechanism in human mesenchymal stem cells. Toxicol Appl Pharmacol 2010;245(2):272-279.
169. Guzman R, Bliss T, De Los Angeles A, Moseley M, Palmer T, Steinberg G. Neural progenitor cells transplanted into the uninjured brain undergo targeted migration after stroke onset. J Neurosci Res 2008;86(4):873-882.
170. Kolosnjaj-Tabi J, Wilhelm C, Clement O, Gazeau F. Cell labeling with magnetic nanoparticles: opportunity for magnetic cell imaging and cell manipulation. J Nanobiotechnology 2014;11 Suppl 1:S7.
171. Wilhelm C, Gazeau F, Bacri JC. Magnetophoresis and ferromagnetic resonance of magnetically labeled cells. Eur Biophys J 2002;31(2):118-125.
172. Sellgren KL, Ma T. Perfusion conditioning of hydroxyapatite-chitosan-gelatin scaffolds for bone tissue regeneration from human mesenchymal stem cells. J Tissue Eng Regen Med 2011;6(1):49-59.
173. Walczak P, Kedziorek DA, Gilad AA, Barnett BP, Bulte JW. Applicability and limitations of MR tracking of neural stem cells with asymmetric cell division and rapid turnover: the case of the shiverer dysmyelinated mouse brain. Magn Reson Med 2007;58(2):261-269.
174. Augat P, Eckstein F. Quantitative imaging of musculoskeletal tissue. Annu Rev Biomed Eng 2008;10:369-390.
175. Daldrup-Link HE, Rudelius M, Metz S, et al. Cell tracking with gadophrin-2: a bifunctional contrast agent for MR imaging, optical imaging, and fluorescence microscopy. Eur J Nucl Med Mol Imaging 2004;31(9):1312-1321.
176. Mowat P, Franconi F, Chapon C, et al. Evaluating SPIO-labelled cell MR efficiency by three-dimensional quantitative T2* MRI. NMR Biomed 2007;20(1):21-27.
177. Schnell SA, Staines WA, Wessendorf MW. Reduction of lipofuscin-like autofluorescence in fluorescently labeled tissue. J Histochem Cytochem 1999;47(6):719-730.
178. Billinton N, Knight AW. Seeing the wood through the trees: a review of techniques for distinguishing green fluorescent protein from endogenous autofluorescence. Anal Biochem 2001;291(2):175-197.

179. Krug R, Han ET, Banerjee S, Majumdar S. Fully balanced steady-state 3D-spin-echo (bSSSE) imaging at 3 Tesla. Magn Reson Med 2006;56(5):1033-1040.
180. Arbab AS, Bashaw LA, Miller BR, Jordan EK, Bulte JW, Frank JA. Intracytoplasmic tagging of cells with ferumoxides and transfection agent for cellular magnetic resonance imaging after cell transplantation: methods and techniques. Transplantation 2003;76(7):1123-1130.